



Algorithm Theoretical Basis Document (ATBD)
for the
Conical-Scanning Microwave Imager/Sounder (CMIS)
Environmental Data Records (EDRs)

Volume 4: Atmospheric Vertical Temperature
Profile EDR

Version 1.4 – 2 December 2003

Submitted by:
Atmospheric and Environmental Research, Inc.
131 Hartwell Ave
Lexington, MA 02421-3126

With contributions by:
Alan Lipton, Sid-Ahmed Boukabara, Jean-Luc Moncet, and George Modica

Prepared for:
Boeing Satellite Systems
919 Imperial Avenue
El Segundo, CA 90245

AER Document P1130-TR-I-ATBD-AVTP-20031202

This page intentionally left blank.

REVISION HISTORY

Version	Release Date	POC	Comments
1.0		A. Lipton	
1.1			Inserted discussion and plots regarding performance in relation to polarization. Revised SDR data requirements
1.2	11/22/00		Inserted "Interpretation of SRD requirements" section and revised presentation of vertical averaging function. Inserted description and results for high-latitude rocketsonde dataset. Inserted results for lower atmosphere.
1.3			Revised Doppler correction and FFT binning. Added weighting function plot. Added error budget
1.4	12/2/04	A. Lipton	Revised discussion of Doppler shifting in sections 3.4.6 and 4.2.2.

RELATED CMIS DOCUMENTATION

Government Documents

Title	Version	Authorship	Date
CMIS SRD for NPOESS Spacecraft and Sensors	3.0	Associate Directorate for Acquisition NPOESS IPO	2 March 2001

Boeing Satellite Systems Documents

Title	Description
ATBD for the CMIS EDRs	Multi-volume document covering TDR, SDR, and EDR algorithms and code documentation. See "ATBD for the CMIS EDRs Volume 1: Overview, Part 1: Integration" for the complete list of associated volumes.

TABLE OF CONTENTS FOR VOLUME 4

REVISION HISTORY	3
RELATED CMIS DOCUMENTATION.....	3
TABLE OF CONTENTS	4
LIST OF TABLES	6
LIST OF FIGURES	7
1. Abstract	10
2. Introduction.....	10
2.1. Purpose.....	10
2.2. Document Scope.....	10
3. Overview and Background Information	10
3.1. Objectives of the Atmospheric Vertical Temperature Profile EDR retrieval.....	10
3.2. Summary of EDR requirements.....	10
3.2.1. SRD Requirements.....	10
3.2.2. Interpretation of SRD requirements.....	12
3.2.3. Requirements imposed by other EDR algorithms.....	12
3.3. Historical and background perspective of proposed algorithm	12
3.4. Physics of atmospheric temperature profiling	13
3.4.1. Fundamentals of temperature profiling.....	13
3.4.2. Temperature sounding near the surface	14
3.4.3. Zeeman line splitting.....	15
3.4.4. Spectrum for high-altitude temperature sounding.....	16
3.4.5. Polarization and view geometry.....	20
3.4.6. Doppler shifting	22
3.4.7. Spectral resolution in relation to measurement noise	23
3.5. Instrument Characteristics	24
3.5.1. Instrument overview.....	24
3.5.2. Channel set.....	25
3.5.3. Derived requirements on sensor data.....	29
3.6. Requirements for cross sensor data (NPOESS or other sensors).....	29
3.7. Derived requirements on data from other EDR algorithms	30
3.8. Requirements for ancillary data.....	30
4. Algorithm Description.....	31
4.1. Theoretical Description of Algorithm.....	31
4.2. Mathematical Description of Algorithm.....	32
4.2.1. Profile retrieval.....	32
4.2.2. Upper atmosphere radiative transfer	33
4.2.3. Vertical registration.....	34
4.3. Algorithm Processing Flow	34
4.3.1. Processing Flow for CMIS Atmospheric Vertical Temperature Profile Algorithm	34
4.3.2. Relationship to Overall CMIS Processing Flow	36
4.4. Algorithm inputs	37
4.5. Algorithm outputs	38
4.6. Timing benchmark	38
5. Algorithm Performance	39
5.1. Vertical averaging.....	39
5.2. Lower atmosphere.....	40
5.2.1. Performance test conditions	40
5.2.2. Performance overview	40
5.2.3. Sensitivity studies	42

5.3. Upper atmosphere	43
5.3.1. Performance test conditions	44
5.3.2. Performance overview	49
5.3.3. Polarization errors	64
5.3.4. Sensitivity studies	65
5.4. Performance summary	70
5.5. Performance under degraded measurement conditions	76
5.6. Constraints, Limitations, and Assumptions.....	77
6. Algorithm Calibration and Validation Requirements	80
6.1. Pre-launch	80
6.2. Post-launch.....	80
6.3. Special considerations for Cal/Val.....	80
6.3.1. Measurement hardware	80
6.3.2. Field measurements or sensors	80
6.3.3. Sources of truth data	80
7. Practical Considerations	80
7.1. Numerical Computation Considerations.....	80
7.2. Programming/Procedure Considerations	80
7.3. Computer hardware or software requirements.....	81
7.4. Quality Control and Diagnostics.....	81
7.5. Exception and Error Handling	81
7.6. Special database considerations.....	81
7.7. Special operator training requirements	81
7.8. Archival requirements.....	81
8. Glossary of Acronyms	81
9. References.....	81
9.1. Technical Literature	81

LIST OF TABLES

Table 3-1: SRD Requirements for the Atmospheric Vertical Temperature Profile EDR..	11
Table 3-3. Global frequency of occurrence of geomagnetic field conditions for CMIS, normalized by latitude band.....	21
Table 3-5. SDR data requirements derived from the AVTP algorithm	29
Table 3-7: Temperature data requirements placed on the Core Module by the AVTP algorithm under nominal conditions.....	30
Table 4-1. AVTP algorithm inputs	37
Table 4-2. AVTP algorithm outputs	38
Table 5-1: Nominal performance for the AVTP EDR.....	71
Table 5-3: Error budget for the AVTP EDR (K).....	75
Table 5-5: AVTP error for various environments. Shaded values are excluded from the net, as discussed in the text.	76
Table 5-7: AVTP EDR performance under degraded measurement conditions.....	76
Table 5-9: Excluded measuring conditions for the AVTP EDR.....	77

LIST OF FIGURES

Figure 3-1. The geometry of the geomagnetic field in relation to the satellite view path.	16
Figure 3-3. Weighting function half-maximum spectra (top and bottom curves) and the midpoint between them (middle curve) for the 7^+ line. The frequency offset is with respect to the line center. The computations were made in circular polarization and for the US Standard Atmosphere, an Earth incidence angle of 53° , and a geomagnetic field condition of $ B =61 \mu\text{T}$, $\theta=135^\circ$ (radiation in circular polarization is independent of ϕ).	18
Figure 3-5. As in Figure 3-3, but for the 1^+ line.	18
Figure 3-7. As in Figure 3-3, but with a running average over a uniform 250-kHz passband.	19
Figure 3-9. As in Figure 3-5, but with a running average over a uniform 250-kHz passband.	19
Figure 3-11 Passbands (3-dB limits) for temperature profiling channels for the lowest part of the atmosphere, shown as blue lines and gray bars. The optical depth of a sample atmosphere is shown for reference.	26
Figure 3-13. Passbands (3-dB limits) for temperature profiling channels for the middle part of the profiled atmosphere, shown as blue lines and gray bars. The weighting function center of a sample atmosphere is shown for reference.	27
Figure 3-15. Frequency ranges for temperature profiling channels produced by the FFT, which apply to the upper portion of the profiled atmosphere, shown as blue lines and gray bars. The weighting function center of a sample atmosphere is shown for reference.	28
Figure 3-17 Weighting functions for the CMIS temperature sounding channels for the US Standard Atmosphere and a geomagnetic field condition of $ B =50 \mu\text{T}$, $\theta=135^\circ$.	29
Figure 4-1. Illustration of the process of vertical registration of the temperature profile, for a cross-sectional view through a portion of a scan.	31
Figure 4-3. Processing flow for the upper atmosphere portion of the AVTP EDR algorithm.	35
Figure 4-5. Processing flow for vertical registration for the AVTP EDR algorithm.	36
Figure 4-7. AVTP module algorithm flow in relation to other EDR modules.	37
Figure 5-1. Processing flow for vertical averaging for the AVTP EDR validation.	40
Figure 5-3. Temperature profile retrieval rms error for a) ocean surface and b) land surface, stratified by latitude and season as labeled. Performance is given for data vertically averaged according to the SRD requirements. The drop-off in error just above 300 mb coincides with an increase in the vertical cell size.	41
Figure 5-5. Temperature profile retrieval error with a global atmospheric background constraint (red) and an air mass classified background (dashed green) for a) ocean and b) land surface. These results are for a CFOV size of 50 km and, thus, are not directly comparable to the thresholds. The test cases are cloudy.	42
Figure 5-7. Temperature profile retrieval rms error for a set of 230 profiles with NEDT corresponding to a 50-km CFOV. Frames a and c are for ocean background and frames b and d are for a forest background. In frames c and d, cloud was specified to be held constant at the true value (0 cloud liquid water). These results are for a CFOV size of 50 km and were computed without any vertical averaging.	43
Figure 5-9. A sample of 20 profiles from the NOAA88b dataset.	45
Figure 5-11. The Rosenkranz profiles from latitudes a) lower than and b) greater than 30° . Some of the profiles were extrapolated with constant temperature at the top.	46
Figure 5-13. The CRISTA profiles from latitudes a) lower than and b) greater than 30° . The profiles were extrapolated downward from about 4 mb.	47

Figure 5-15. The high-latitude rocketsonde profiles from latitudes a) lower than and b) greater than 60°. The profiles were extrapolated upward from about 0.08 mb.48

Figure 5-17. Upper atmosphere temperature profile rms error for the current baseline system applied to the Rosenkranz dataset. The errors are for temperatures that have been vertically51

Figure 5-19. Upper atmosphere temperature profile rms error for three values of sensor noise. The NRF in the legend indicates the noise averaging factor, relative to single-footprint noise level. The solid curve corresponds to very low noise, and the dashed and dotted curves correspond to averaging over 300×300 and 200×200 km² CFOVs. The Rosenkranz dataset was used.52

Figure 5-21. Temperature profile error for H polarization and a 300-km CFOV at a) 0.01 mb and b) 1 mb. The Rosenkranz dataset was used. For each test case (true temperature), errors are plotted for each of the 112 tabulated geomagnetic field conditions. Errors are for temperatures that have been vertically averaged per the SRD requirements.53

Figure 5-23. Upper atmosphere temperature profile rms error for the CRISTA dataset. Results from one quarter of the Rosenkranz data are shown for reference. Results are for a 300×300 km² CFOV. Performance is shown for horizontal polarization and for left circular.54

Figure 5-25. Upper atmosphere temperature profile rms error for the high-latitude rocketsonde dataset, using the current baseline system.55

Figure 5-27. Upper atmosphere temperature profile rms error for channel sets with digital (FFT) channels on the 7⁺ line (solid curve) and on both the 7⁺ and 9⁺ lines (dashed curve). Horizontal polarization was used and the CFOV size is about 380×380 km². Statistics are for one quarter of the Rosenkranz dataset.56

Figure 5-29. Upper atmosphere temperature profile rms error for H, V, and left circular channel polarizations. For left circular, the second curve was derived with the assumption that measuring in circular polarization adds 0.2 dB of loss to the sensor system, thus increasing the data noise. The noise is for a CFOV of about 380×380 km², which is larger than the baseline size. One quarter of the Rosenkranz dataset was used.57

Figure 5-31. Retrieval performance for the most favorable geomagnetic conditions for a) H, b) V, and c) LC polarization; and d) for an additional condition discussed in the text. The noise is for a CFOV of 300×300 km². One quarter of the Rosenkranz dataset was used.59

Figure 5-33. Weighting functions for the geomagnetic condition ($|B| = 47 \mu\text{T}$, $\theta = 79^\circ$, $\phi = 79^\circ$) most favorable for H polarization. Polarizations shown are a) H, b) V, and c) LC.60

Figure 5-35. Weighting functions for the geomagnetic condition ($|B| = 33 \mu\text{T}$, $\theta = 101^\circ$, $\phi = 34^\circ$) most favorable for V polarization. Polarizations shown are a) H, b) V, and c) LC.61

Figure 5-37. Weighting functions for the geomagnetic condition ($|B| = 33 \mu\text{T}$, $\theta = 124^\circ$, $\phi = 34^\circ$) most favorable for LC polarization. Polarizations shown are a) H, b) V, and c) LC.62

Figure 5-39. Weighting functions for an additional geomagnetic condition ($|B| = 40 \mu\text{T}$, $\theta = 11^\circ$, $\phi = 56^\circ$) favorable for LC polarization. Polarizations shown are a) H, b) V, and c) LC.63

Figure 5-41. Upper atmosphere temperature profile rms error for varying polarization purity knowledge error. The labeled value of 0.01 represents $(1-\alpha)$. The noise is for a CFOV of 300×300 km². One quarter of the Rosenkranz dataset was used.64

Figure 5-43. Comparison of temperature profile rms errors for the physical algorithm and regression, as applied to the Rosenkranz dataset. The polarization is horizontal and noise is for a CFOV of 300×300 km².66

Figure 5-45. Comparison of temperature profile rms errors for the physical algorithm and regression, as applied to standard atmosphere profiles. The noise is for a CFOV of 300×300 km².67

Figure 5-47. Upper atmosphere temperature profile rms error, as a function of the number of iterations of the physical algorithm. The polarization is horizontal and noise is for a CFOV of 300×300 km². One quarter of the Rosenkranz dataset was used.68

Figure 5-49. Stratified upper atmosphere temperature profile rms error. Each curve represents error under one geomagnetic field condition. The polarization is horizontal and noise is for a CFOV of about 380×380 km². One quarter of the Rosenkranz dataset was used. 69

Figure 5-51. Sensitivity of upper atmosphere temperature profile rms error to loss of all the FFT-processed channels and loss of two individual channels (FFT bins). The polarization is horizontal and noise is for a CFOV of 300×300 km². One quarter of the Rosenkranz dataset was used.70

Figure 5-53: Impact of center frequency instability error on upper atmosphere temperature profile retrieval error. Results are shown for left circular (LC) and horizontal polarization (H). The red solid and blue dotted curves are for simulated retrievals with center frequencies shifted 20 kHz from the “true” values. Noise is for a CFOV of 300×300 km².73

Figure 5-55: Temperature profile retrieval rms error for various precipitation rates. The curves are for the first-guess (dashed red), clear sky (black), and rain rates of 0.1 (blue), 0.4 (green-blue), 1.0 (yellow-green), and 1.7 (red) mm/h. The test cases for this plot had a rain layer top at 700 mb and excludes channels with frequencies above 61 GHz. The plotted performance is for 30-km CFOV size and was computed without vertical averaging, so it is not directly comparable to the SRD requirements.77

Figure 5-57. Upper atmosphere temperature profile rms error for varying center frequency knowledge error. The errors are given as a fraction of the bandwidth. The plot is for a channel set with digital (FFT) channels having 156-kHz resolution, so a shift of 10% is 15.6 kHz for the digital channels. The noise averaging factor was 0.17. Statistics are for a 20-profile subset of the Rosenkranz dataset. The sampling of geomagnetic field conditions was from method 1.79

Figure 5-59. Brightness temperature residual difference from the upper atmosphere algorithm as a function of the center frequency shift from the nominal passband positions, corresponding to Figure 5-57.80

1. Abstract

2. Introduction

2.1. Purpose

The purpose of this document is to provide a reference for the background, methodology, and performance of the CMIS Atmospheric Vertical Temperature Profile EDR algorithms. It presents the theoretical basis for retrieving temperature profiles from conically-scanning microwave satellite observations, history of retrieval algorithm developments, a description of the algorithm used for CMIS, requirements associated with the algorithm, retrieval performance and its dependence on sensor and environmental factors.

2.2. Document Scope

A substantial portion of the process for obtaining the Atmospheric Vertical Temperature Profile EDR is performed by the Core Physical Inversion Module, which is described in the ATBD for the Core Physical Inversion Module (ATBD Vol. 2). The material covered in that ATBD is not repeated here. This document describes how the products of the core module are integrated with other algorithms to produce Atmospheric Vertical Temperature Profile EDRs. In particular, the retrieval of the temperature profile in the upper portion of the atmosphere is not part of the core module and is described in detail here.

The ATBD provides outlines for continued algorithm development and advancement and for pre- and post-launch calibration/validation efforts. These outlines are intended to be reviewed and revised prior to launch as new data sources and research become available.

3. Overview and Background Information

3.1. Objectives of the Atmospheric Vertical Temperature Profile EDR retrieval

The Atmospheric Vertical Temperature Profile (AVTP) algorithm must produce estimates of the temperature of the atmosphere. The temperature reports are to be made along vertical paths through the atmosphere, using the term profile to refer to a set of temperatures along a single path. Each report consists of temperatures given as a function of atmospheric pressure for a specified location. Temperature profiles are to be produced within the swath observed by CMIS so that coverage is global upon a series of NPOESS orbits.

For a conical scanner such as CMIS, the paths over which the instrument views the atmosphere are slanted with respect to the local vertical of the observed location. The AVTP algorithm produces estimates of temperatures along the CMIS view paths, given as a function of pressure, as an initial algorithm product. These temperature profiles then undergo further processing to generate the final EDR products that are registered to vertically-oriented paths, for compliance with the CMIS System Requirements Document (SRD).

3.2. Summary of EDR requirements

3.2.1. SRD Requirements

The text below and Table 3-1 are the portions of CMIS SRD section 3.2.1.1.1.1 that apply directly to the AVTP algorithm.

Atmospheric Vertical Temperature Profile

An atmospheric temperature profile is a set of estimates of the average atmospheric temperature in three-dimensional cells centered on specified points along a local vertical.

Table 3-1: SRD Requirements for the Atmospheric Vertical Temperature Profile EDR

Para. No.		Thresholds	Objectives
C40.2.2-1	a. Horizontal Cell Size		
	1. Surface to 20 mb	40 km	5 km
	2. 20 mb to 0.01 mb	200 km	200 km
C40.2.2-2	Deleted		
C40.2.2-3	Deleted		
C40.2.2-4	Deleted		
C40.2.2-5	b. Horizontal Reporting Interval		
	1. Surface to 20 mb	40 km	5 km
	2. 20 mb to 0.01 mb	200 km	200 km
	c. Vertical Cell Size		
	Clear		
C40.2.2-6	1. Surface to 300 mb	1 km	(TBD)
C40.2.2-7	2. 300 mb to 30 mb	3 km	(TBD)
C40.2.2-8	3. 30 mb to 1 mb	5 km	(TBD)
C40.2.2-9	4. 1 mb to 0.01 mb	5 km	(TBD)
	Cloudy		
C40.2.2-10	5. Surface to 700 mb	1 km	(TBD)
C40.2.2-11	6. 700 mb to 300mb	1 km	(TBD)
C40.2.2-12	7. 300 mb to 30 mb	3 km	(TBD)
C40.2.2-13	8. 30 mb to 1 mb	5 km	(TBD)
C40.2.2-14	9. 1 mb to 0.01 mb	5 km	(TBD)
	d. Vertical Reporting Interval		
C40.2.2-15	1. Surface to 850 mb	20 mb	15 mb
C40.2.2-16	2. 850 mb to 300 mb	50 mb	15 mb
C40.2.2-17	3. 300 mb to 100 mb	25 mb	15 mb
C40.2.2-18	4. 100 mb to 10 mb	20 mb	10 mb
C40.2.2-19	5. 10 mb to 1 mb	2 mb	1 mb
C40.2.2-20	6. 1 mb to 0.1 mb	0.2 mb	0.1 mb
C40.2.2-21	7. 0.1 mb to 0.01 mb	0.02 mb	0.01 mb
C40.2.2-22	e. Horizontal Coverage	Global	Global
C40.2.2-23	f. Vertical Coverage	Surface to 0.01 mb	Surface to 0.01 mb
C40.2.2-24	g. Measurement Range	180-335K	162-335K (TBR)
C40.2.2-25	Not used		
	h. Measurement Uncertainty		
	Clear		
C40.2.2-26	1. Surface to 700 mb	1.6 K / 1 km layers	0.5K / 1km
C40.2.2-37	2. 700 mb to 300 mb	1.5 K / 1 km layers	0.5K / 1 km
C40.2.2-27	3. 300 mb to 30 mb	1.5 K / 3 km layers	0.5K / 1km
C40.2.2-28	4. 30 mb to 1 mb	1.5 K / 5 km layers	0.5K / 1km
C40.2.2-29	5. 1 mb to 0.01 mb	3.5 K / 5 km layers	0.5K / 1km
	Cloudy		
C40.2.2-30	5. Surface to 700 mb	2.5 K / 1 km layers (TBR)	0.5K / 1km
C40.2.2-31	6. 700 mb to 300 mb	1.5 K / 1 km layers (TBR)	0.5K / 1km
C40.2.2-32	7. 300 mb to 30 mb	1.5 K / 3 km layers (TBR)	0.5K / 1km
C40.2.2-33	8. 30 mb to 1 mb	1.5 K / 5 km layer (TBR)	0.5K / 1km
C40.2.2-34	9. 1 mb to 0.01 mb	3.5 K / 5 km layers (TBR)	0.5K / 1km
C40.2.2-35	i. Mapping Uncertainty	5 km	1 km
C40.2.2-36	j. Swath Width	1700 km (TBR)	3000 km (TBR)

In addition to these requirements, the SRD specifies:

1. “Science algorithms shall process CMIS data, and other data as required, to provide the [EDRs] assigned to CMIS.” (SRD, paragraph SRDC3.1.4.2-1)
2. “As a minimum, the EDR requirements shall be satisfied at the threshold level.” (SRDC3.2.1.1.1-3)
3. “... the contractor shall identify the requirements which are not fully satisfied, and specify the conditions when they will not be satisfied.” (SRCD3.2.1.1.1-4)
4. “... CMIS shall satisfy the EDR Thresholds associated with cloudy conditions under all measurement conditions ...” (SRDC3.2.1.1.1-1)
5. “The CMIS contractor should consider the effects of the relative motion of the satellite and CMIS sensor scan LOS on the retrieval of atmospheric EDRs.” (SRD 3.2.1.11 Doppler Correction or Tracking). “The CMIS contractor shall account for these effects in either the CMIS hardware design or science algorithms or both.” (SRDC3.2.1.11-1).

3.2.2. Interpretation of SRD requirements

Revisions to the SRD have clarified that the horizontal cell size requirement is meant to specify the area over which averaging is done when validating EDRs against truth data. We infer that the vertical cell size requirement is, likewise, a validation requirement. According to our interpretation, the vertical cell size represents the distance over which profile data are averaged when validating EDRs against truth data. We infer that the EDR product to be delivered to the CMIS customers should be a profile of point values with the greatest vertical resolution the CMIS system is capable of providing (within the context of other system requirements), without any deliberate vertical averaging (smoothing). Only in the course of validation are the data processed so that they are estimates of the average temperature in three-dimensional cells.

3.2.3. Requirements imposed by other EDR algorithms

The upper atmosphere module of the AVTP algorithm provides input to the Core Physical Inversion Module (core module). The data provided to the core module is used to enhance the consistency between the upper and lower-atmosphere products and to save computation time for the core module by reducing the number of channels that module must process. However, the core module can meet its requirements without data from the upper atmosphere module, so the core module imposes no requirements on the upper atmosphere module.

3.3. Historical and background perspective of proposed algorithm

The atmospheric temperature profile has, in principle, an infinite number of degrees of freedom; that is, the profile represents temperatures for a series of infinitesimal layers of the atmosphere. Satellite instruments provide some finite number of observations that are not fully independent of each other and are noisy. Temperature profile retrieval algorithms, thus, must include some constraints in order to obtain a stable, realistic solution.

Algorithms for atmospheric temperature profiling from satellites fall into two primary categories, statistical and physical. Statistical algorithms rely on developing statistical relationships between satellite radiometric data and temperature profile data. Various forms of linear regression have been used (Wark and Fleming, 1966; Smith and Woolf, 1976). Physical algorithms involve radiative transfer computations in the execution of the retrieval algorithm, with the objective to find a temperature profile that, when inserted in a radiative transfer model, yields radiometric

data that match the observed radiometric data to within some tolerance. The constraints used in physical algorithms may directly impose smoothness on the temperature profile (Chahine, 1968; Smith, 1970; Hayden, 1988) or may be derived from statistics of archived temperature profile data (Rodgers, 1970). Some algorithms have a statistical first step followed by a physical retrieval process. The statistical step may use clustering/discriminant analysis methods (Uddstrom and Wark, 1985; Thompson, et al., 1985; Chedin, et al., 1985). A review of methods published through 1976, with a discussion of fundamental issues, is given by Rodgers (1976).

3.4. Physics of atmospheric temperature profiling

3.4.1. Fundamentals of temperature profiling

The brightness temperature for monochromatic microwave radiation may be represented as

$$T_B = \varepsilon_s T_s \mathfrak{T}_s + \int_{\mathfrak{T}_s}^1 T d\mathfrak{T} + (1 - \varepsilon_s) \mathfrak{T}_s \int_{\mathfrak{T}'_s}^1 T d\mathfrak{T}' + (1 - \varepsilon_s) \mathfrak{T}_s \mathfrak{T}'_s T_c,$$

where the subscript s indicates the surface, T is the temperature, ε is the emissivity, T_c is the cosmic temperature, \mathfrak{T} is the transmittance from some point in the atmosphere to the satellite, \mathfrak{T}' is the transmittance from some point in the atmosphere to the surface. The Rayleigh-Jeans approximation has been used, scattering is assumed to be negligible, and it is assumed that the surface reflectance is equal to one minus the directional emissivity. When a specular assumption is used for surface reflection, the transmittance from space to the surface (\mathfrak{T}'_s) is the same as from the surface to space (\mathfrak{T}_s). The brightness temperature in this equation is a weighted average of the temperatures of the surface, the atmosphere, and the cosmic background, with the weights adding to unity as

$$\varepsilon_s \mathfrak{T}_s + (1 - \mathfrak{T}_s) + (1 - \varepsilon_s) \mathfrak{T}_s (1 - \mathfrak{T}'_s) + (1 - \varepsilon_s) \mathfrak{T}_s \mathfrak{T}'_s = 1.$$

The temperature in any finite layer of the atmosphere is weighted by $\Delta\mathfrak{T} + (1 - \varepsilon_s) \mathfrak{T}_s \Delta\mathfrak{T}'$. The weighting is often written with respect to the logarithm of pressure as

$$\frac{d\mathfrak{T}}{d \ln p} \Delta \ln p + (1 - \varepsilon_s) \mathfrak{T}_s \frac{d\mathfrak{T}'}{d \ln p} \Delta \ln p,$$

and the second term is sometimes neglected when dealing

with the infrared spectrum where ε_s is near unity. When these weights are plotted as a function of $\ln p$, they constitute a weighting function that describes the contributions of atmospheric temperature at each level to the remotely sensed brightness temperature at the given microwave frequency.

Closely related to the weighting function is the sensitivity function, which is obtained by taking the derivative of the brightness temperature with respect to the temperature in each finite layer and then normalizing by the thickness of the layer. The weighting functions are identical to the sensitivity functions in the linear case where \mathfrak{T} is independent of temperature. In the 50–60 GHz range, the weighting functions are similar to sensitivity functions, though significant differences may occur.

When satellite observations are made at a number of frequencies along the edges of an absorption line, a set of weighting functions occur, with peaks at various altitudes. The observations may then be analyzed together to retrieve the temperature profile from the brightness temperatures. The ability to resolve temperature variations along the line of sight (in

the vertical or slant path) depends on the width of the weighting functions, with broader weighting functions providing less vertical resolution. For monochromatic radiation, the width is dictated by the pressure structure of the atmosphere along with the physics of radiative transfer. When a satellite channel averages radiation over some finite band of frequencies, the weighting functions are broadened further if the optical properties of the atmosphere vary across the band, as they tend to do near absorption lines.

For temperature sounding, it is preferable to use frequencies where the absorption is dominated by a gas that has a fixed, well-known concentration. If the gas is highly variable, such as with water vapor, the temperature weighting functions vary with the gas concentration and it is difficult to associate a temperature signal with a specific level of the atmosphere. In the microwave spectrum, only molecular oxygen provides suitable absorption lines for temperature sounding. There is a complex of lines in the range of 50 to 70 GHz and a single line at 118.75 GHz. CMIS relies on the spectrum near 60 GHz because 1) the line complex provides spectral bands where the optical properties vary little over a significant range of frequencies, helping to narrow weighting functions, 2) contamination from cloud and rain water (liquid and ice) is less at lower frequencies, and 3) receiver technology allows for lower instrument noise at 60 GHz than at 118 GHz.

3.4.2. Temperature sounding near the surface

The second term in the temperature weighting function, $(1 - \epsilon_s) \mathfrak{T}_s \Delta \mathfrak{T}'$, becomes larger as the surface emissivity decreases, suggesting that lower emissivities give rise to larger temperature signals and improved retrieval performance. The situation is different, however, when the full sensitivity function is considered. To illustrate, consider the radiative transfer equation for an isothermal atmosphere, while neglecting the cosmic term and assuming specular surface reflection:

$$T_B = \epsilon_s T_s \mathfrak{T}_s + (1 - \mathfrak{T}_s) T + (1 - \mathfrak{T}_s)(1 - \epsilon_s) \mathfrak{T}_s T$$

The sensitivity function is

$$\frac{\partial T_B}{\partial T} = [\epsilon_s (T_s - T + 2\mathfrak{T}_s T) - 2\mathfrak{T}_s T] \frac{\partial \mathfrak{T}_s}{\partial T} - \epsilon_s \mathfrak{T}_s (1 - \mathfrak{T}_s) + (1 - \mathfrak{T}_s^2)$$

and its dependence on emissivity is

$$\frac{\partial^2 T_B}{\partial T \partial \epsilon_s} = (T_s - T + 2\mathfrak{T}_s T) \frac{\partial \mathfrak{T}_s}{\partial T} - \mathfrak{T}_s (1 - \mathfrak{T}_s).$$

English (1999) showed that, for absorption by oxygen near 50 GHz the first (nonlinear) term nearly offsets the second (linear) term, reducing the sensitivity of air temperature signal to surface emissivity.

This analysis addresses the effect of emissivity near 50 GHz, but not in the other CMIS channels. Emissivities at other frequencies influence the skill at retrieving surface temperature and atmospheric water vapor, which indirectly affects skill at retrieving air temperature near the surface. For example, the low-frequency emissivities of the ocean surface are more favorable than land surface emissivities for retrieving surface temperature and water vapor, tending to make temperature profile performance better over ocean than over land.

The vertical resolution of the temperature sounding channel, as represented by the breadth of their weighting functions, is a factor in temperature profiling performance at all altitudes, but particularly near the surface. Microwave temperature sounding frequencies do not provide sufficient vertical resolution to resolve sharp vertical gradients that occur in the atmosphere. Vertical gradients near the surface are often very sharp and of high amplitude, because of the strong energy fluxes that occur at the surface. Temperature retrieval errors tend to increase, therefore, near the surface wherever such gradients are present. This affect is diminished over ocean and other water surfaces, because the surface energy fluxes are buffered by the large heat capacity of water and the transfer of energy between the surface and subsurface water.

3.4.3. Zeeman line splitting

Temperature profiling at high altitudes entails additional considerations. The Zeeman effect causes O₂ absorption lines to split in the presence of the Earth geomagnetic field. In the lower part of the atmosphere (below about 40 km altitude) the splitting is negligible in comparison with line broadening associated with the air pressure. At higher altitudes (lower pressures) the pressure broadening effect is less and Zeeman line splitting becomes significant near line centers. The number of Zeeman components into which a line splits increases and the separation of components decreases in relation to the angular momentum quantum number associated with the line (Lenoir, 1968). The propagation of radiation in the presence of the Zeeman effect has a polarization dependence that cannot be accounted for with scalar radiative transfer. A matrix form of radiative transfer must be used and coherency matrices provide a convenient way to represent the polarization states (Lenoir, 1967; Lenoir, 1968). The computation method of Rosenkranz and Staelin (1988) was used for our algorithm development. The method provides for computation of weighting functions, although the formulation is different than for the scalar case described above.

Computation of radiative transfer in the presence of the Zeeman effect requires description of the geomagnetic field along the view path of the satellite. At each point along the path, it is necessary to describe the magnitude of the magnetic field and its orientation with respect to the view path. The orientation parameters are illustrated in Figure 3-1, where θ is the angle between the view path and the magnetic field vector and ϕ describes the alignment between the magnetic field and the polarization reference of the satellite sensor.

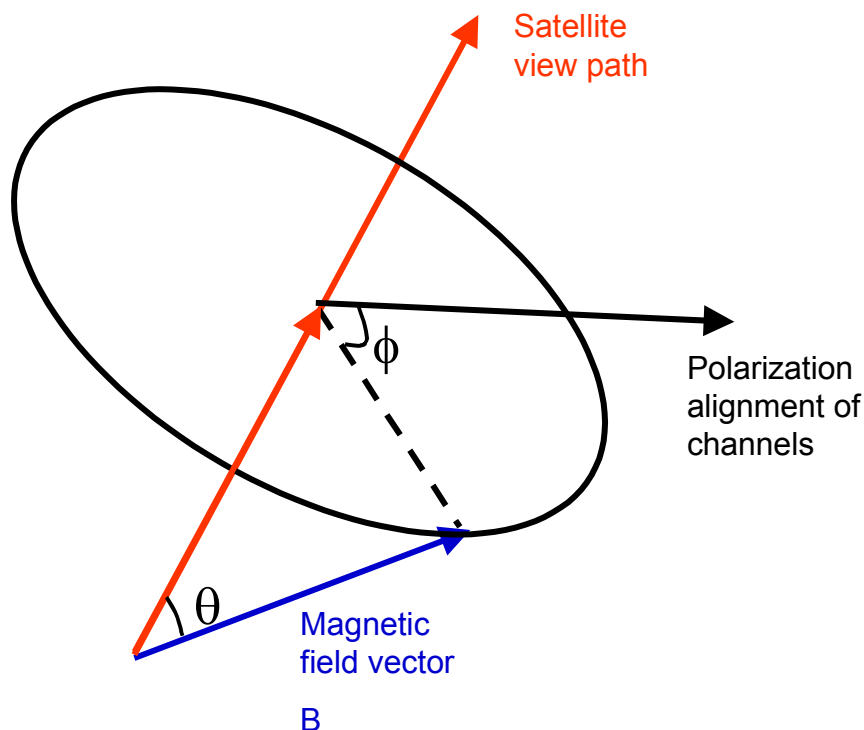


Figure 3-1. The geometry of the geomagnetic field in relation to the satellite view path.

3.4.4. Spectrum for high-altitude temperature sounding

For temperature sounding to pressures as low as 0.01 mb (the upper limit of required vertical coverage) from a conically-scanning sounder, it is necessary to site channels among the strongest O₂ absorption lines. Along with line strength, however, the Zeeman effect must be considered because the peak absorption also depends on the number of Zeeman components into which the absorption is divided and the component spacing. In the following discussion, we follow the convention of identifying lines by the rotational quantum number of the upper energy level and the sign of the change in angular momentum. The 7⁺ line is stronger than the 1⁺ line, but its highest peaking weighting function is lower in the example shown in Figure 3-2 and Figure 3-3. The weighting functions are shown in circular polarization, but the relative peaks of the two lines are similar in linear polarization. It is necessary, however, to consider also the breadth of the weighting function spectral features. Using digital technology, CMIS is able to sample near the line center with a spectral resolution of 250 kHz. When the weighting function spectra are averaged to 250-kHz resolution (Figure 3-4 and Figure 3-5), the 7⁺ line provides the higher peak. The 7⁺ line was advantageous in this respect over other lower-ordered lines (3⁺ and 5⁺) also. The 7⁺ line would have an even greater advantage with broader passbands such as the 1500-kHz passbands used for SSMIS. A further benefit of the 7⁺ line is the relative smooth range of weighting functions that may be used for sounding at lower altitudes. In contrast, the 1⁺ line, with only three Zeeman components has weighting functions dropping off sharply from the peaks, with very little spectrum available for sounding in, for example, the 0.03-mb range. The narrower the available spectrum, the higher is the measurement noise for any channel(s) that measure in that range. An opportunity for future technology insertion may arise to operate digital channels on multiple O₂ lines at spatial resolution finer than 250 kHz, accessing the beneficial aspects of each line.

The 1^- line at 118.75 GHz has three Zeeman components, as with the 1^+ line, and it thus has similar drawbacks. A further drawback is the higher receiver noise at the higher frequency.

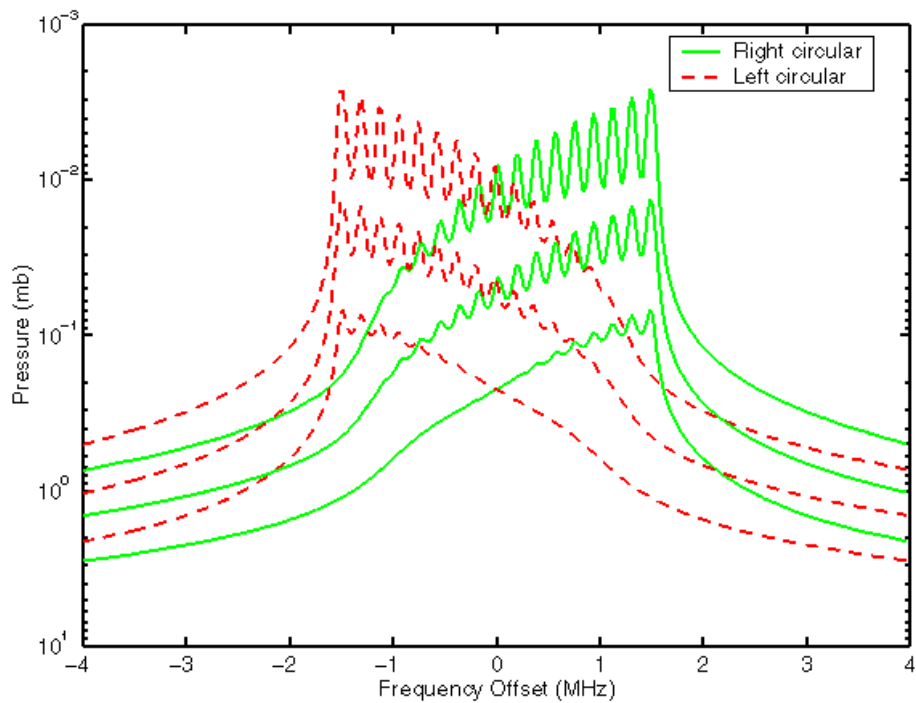


Figure 3-2. Weighting function half-maximum spectra (top and bottom curves) and the midpoint between them (middle curve) for the 7^+ line. The frequency offset is with respect to the line center. The computations were made in circular polarization and for the US Standard Atmosphere, an Earth incidence angle of 53° , and a geomagnetic field condition of $|B|=61 \mu\text{T}$, $\theta=135^\circ$ (radiation in circular polarization is independent of ϕ).

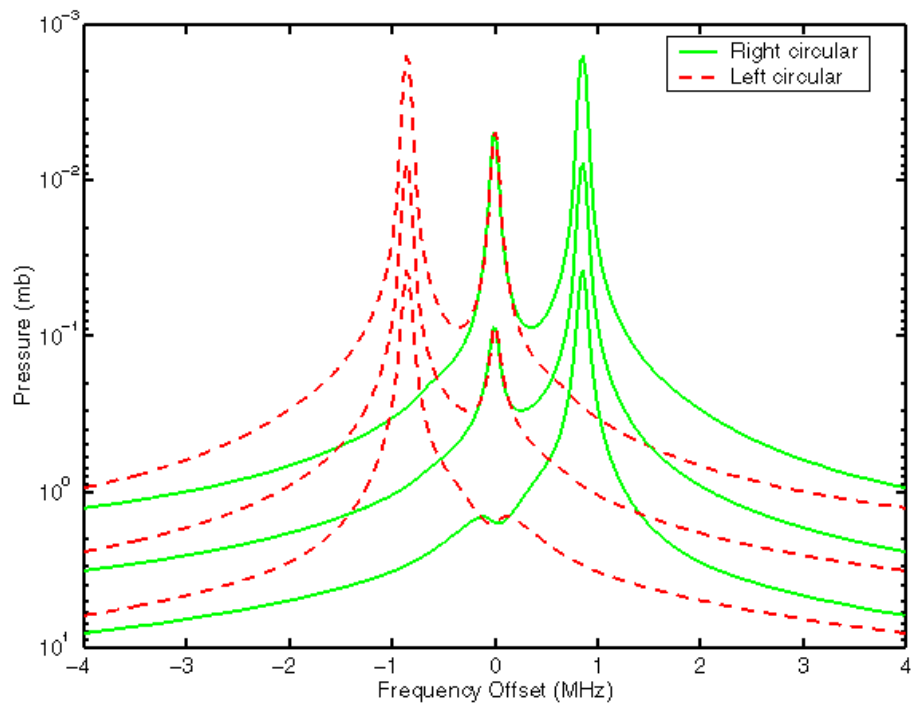


Figure 3-3. As in Figure 3-2, but for the 1^+ line.

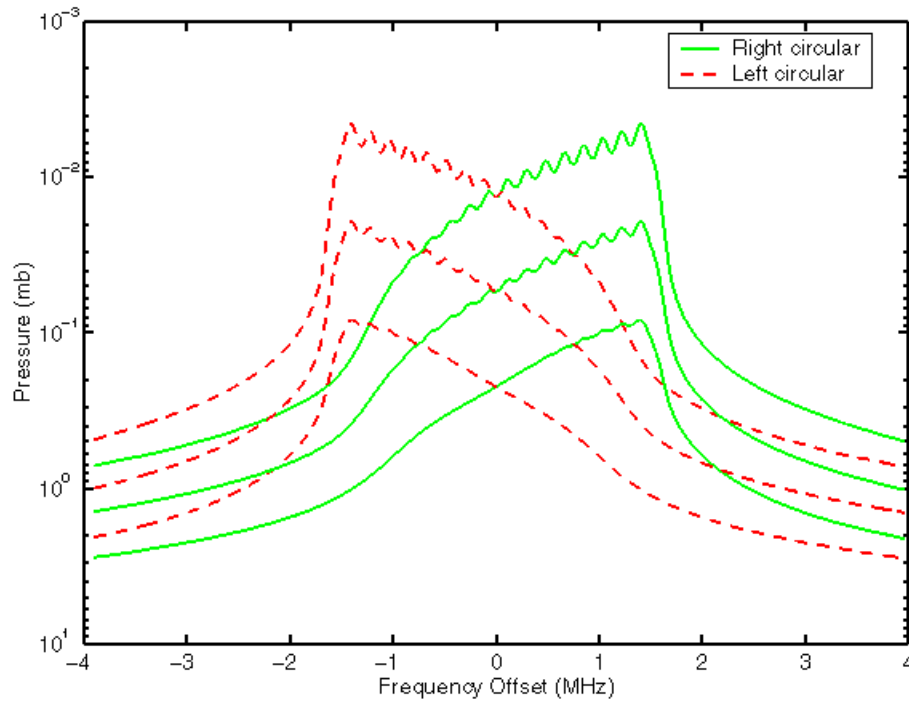


Figure 3-4. As in Figure 3-2, but with a running average over a uniform 250-kHz passband.

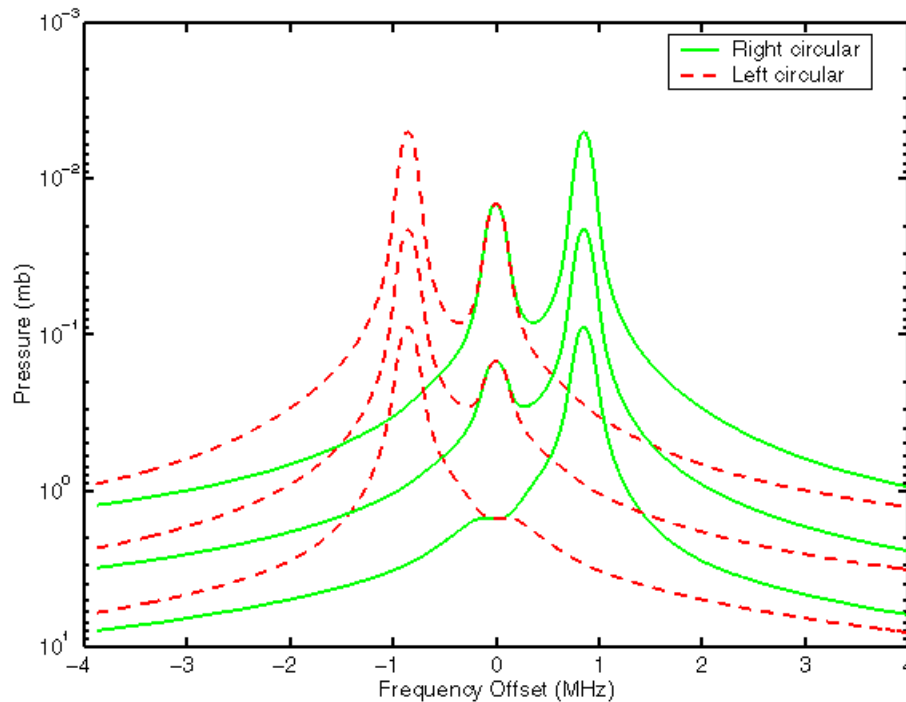


Figure 3-5. As in Figure 3-3, but with a running average over a uniform 250-kHz passband.

It is apparent from these plots of weighting function spectra (particularly Figure 3-4) that, for sounding to 0.01 mb, it is necessary to make measurements about 1 MHz off the line center and with a spectral resolution of about 1 MHz or finer. With coarser spectral resolution, the measurements would average over weighting functions spanning a broad range of pressure levels, degrading the vertical resolution of temperature profiling.

3.4.5. Polarization and view geometry

Another prominent consideration for temperature sounding at low pressures is the choice of polarization at which the measurements are made. (See also [EN #55](#) response.) The Zeeman-split spectrum for right circular polarization is a mirror image, about the line center, of the spectrum for left circular polarization. When measurements are taken symmetrically about the line center, as with the digital channel set, a choice between left and right circular polarization is arbitrary. There are major differences, however, between the radiation in circular and linear polarizations. When the view path is perpendicular to the geomagnetic field ($\theta=90^\circ$) the radiation has independent linear components along and across the direction of the magnetic field vector, with weighting functions in the two components at different altitudes. In this case, measurements in circular polarization provide a blend of the two linear components and smear together the weighting functions. When the view path is parallel to the geomagnetic field ($\theta=0^\circ$ or 180°) the radiation has independent left and right circular components whose weighting functions may be at substantially different altitudes (greater separation than in Figure 3-2) at an offset from the line center. If measurements are made in linear polarization in this case, the measurements merge the left and right-circular weighting functions and may produce double-peaked net weighting functions (Lenoir, 1968; Rosenkranz and Staelin, 1988). Double peaking is detrimental to retrieval of the temperature profile, increasing the ambiguity in the relationship between the brightness temperatures and the temperature profile. Intermediate angles θ produce intermediate effects.

For measurements in linear polarization, an additional consideration is the polarization alignment ϕ . It is not feasible to maintain alignment between the satellite antenna polarization and the geomagnetic field orientation as the satellite executes its scan. Linearly polarized channels on CMIS are oriented with respect to the horizontal and vertical planes at the Earth surface, so the alignment rotates over the scan.

For any given polarization of a temperature sounding channel, the magnitude of the magnetic field $|B|$ and the angles θ and ϕ vary as the satellite orbits and scans. The performance for a polarization depends on the frequency of occurrence of each combination of $|B|$, θ , and ϕ .

The geomagnetic field conditions for CMIS were computed for a set of full earth orbits spaced 3° in longitude, with views taken every 3° along the orbital path and every 3° of scan angle. For each of the views, we computed $|B|$, θ and ϕ . We then computed a frequency distribution among these three parameters. The distribution was normalized according to the number of views that occur within each 10-degree band of latitude. There tend to be more views near the poles for a polar-orbiting satellite, and the normalization removed that bias. The distribution was further normalized by the area of the latitude band (approximated by the cosine of the latitude of the band center) so the normalized distribution would be indicative of a uniformly spaced sampling around the earth. This frequency distribution occupies a three-dimensional space ($|B|, \theta, \phi$), where the range of $|B|$ depends on the range of magnetic field strengths that occur around the Earth at about 80-km altitude. By definition of the coordinate system, θ varies between 0 and 180° and ϕ varies between 0 and 360° . The orientation of ϕ is here defined such that $\phi = 90^\circ$ when the geomagnetic field is aligned with the vertical polarization. The range of ϕ is compressed to 0 to 180° by the periodicity of polarization rotation. When symmetries are accounted for in linear polarization, ϕ varies between 0 and 90° , since $T_{B,P}(\theta, \phi) = T_{B,P}(180^\circ - \theta, -\phi)$, where $T_{B,P}$ is the radiance in linear polarization P . In circular polarization, ϕ is irrelevant and θ varies between 0 and 90° because $T_{B,C}(\Delta f, \theta) = T_{B,C}(-\Delta f, 180^\circ - \theta)$, where C is either left or right circular

polarization, Δf is the frequency offset from the center of the absorption line, and it is assumed that $T_{B,C}$ values on both sides of the line are measured. The distribution was tabulated (Table 3-2) over ranges of $|B|$, θ , and ϕ that exploit only the symmetries common to linear and circular polarization. The domain was divided into a grid of dimension (6,8,4) for the tabulation.

Table 3-2 illustrates several features relevant to the choice of polarization for sounding. The highest values of $|B|$ (where Zeeman splitting is most pronounced) occur only for values of ϕ near 90° . This correspondence is explained by the fact that the highest values of $|B|$ occur near the magnetic poles, where the magnetic field lines are aligned along the local vertical. In addition, the highest values of $|B|$ never occur for θ near 0 or 180° . Such a condition could only occur when the satellite is directly over a magnetic pole and is scanning at the nadir, which could happen for a cross-track scanner but never happens for a conical scanner. Values of θ near 0 or 180° (where circular polarization is most advantageous) are unusual overall, and tend to occur at the moderate values of $|B|$ some distance from the magnetic pole where the field lines are at an angle similar to the CMIS incidence angle. Low values of $|B|$ are broadly distributed with respect to ϕ , as a wide range of polarization alignments can occur as the satellite scans conically near the magnetic equator, where the field lines are roughly parallel to the Earth surface.

Table 3-2. Global frequency of occurrence of geomagnetic field conditions for CMIS, normalized by latitude band.

ϕ range $0-22^\circ$						
θ range ($^\circ$)	Normalized frequency of occurrence (tenths of percent)					
0-22	13	37	29	7	0	0
22-45	32	99	73	10	0	0
45-68	39	95	46	1	0	0
68-90	26	51	20	0	0	0
90-112	28	38	8	0	0	0
112-135	44	110	67	2	0	0
135-158	35	101	73	10	0	0
158-180	14	36	30	7	0	0
B range: (μT)	22-29	29-36	36-43	43-50	50-57	57-65

ϕ range $22-45^\circ$						
θ range ($^\circ$)	Normalized frequency of occurrence (tenths of percent)					
0-22	14	30	36	11	0	0
22-45	35	70	91	45	1	0
45-68	36	78	49	12	0	0
68-90	39	87	43	0	0	0
90-112	39	94	63	8	0	0
112-135	61	101	94	36	1	0
135-158	45	75	99	46	1	0
158-180	14	31	36	11	0	0
B range:	22-29	29-36	36-43	43-50	50-57	57-65

(μT)						
-------------------	--	--	--	--	--	--

ϕ range 45–68°						
θ range (°)	Normalized frequency of occurrence (tenths of percent)					
0–22	15	27	38	17	1	0
22–45	52	62	47	108	59	1
45–68	46	77	48	48	33	2
68–90	88	131	132	56	5	0
90–112	67	141	199	130	21	0
112–135	102	110	87	170	114	5
135–158	76	78	62	127	65	1
158–180	15	27	39	17	1	0
 B range: (μT)	22–29	29–36	36–43	43–50	50–57	57–65

ϕ range 68–90°						
θ range (°)	Normalized frequency of occurrence (tenths of percent)					
0–22	16	28	35	24	4	0
22–45	50	55	26	78	149	55
45–68	30	72	37	11	209	202
68–90	139	140	201	256	165	18
90–112	132	137	221	303	196	21
112–135	31	74	37	38	508	287
135–158	49	54	28	86	170	61
158–180	16	27	34	24	4	0
 B range: (μT)	22–29	29–36	36–43	43–50	50–57	57–65

3.4.6. Doppler shifting

Radiative measurements from CMIS are affected by Doppler shifting because the relative motion between the orbiting satellite and the atmosphere has a component along the CMIS line of sight. Radiation that is transmitted from the top of the atmosphere at frequency f is received by a moving platform at frequency $f+\Delta$. There are two primary factors that contribute to Doppler shifting for CMIS measurements: 1) the motion of the satellite, projected onto the view path, and 2) the motion of the atmosphere due to Earth rotation. The total shift Δ maybe computed as

$$\Delta = \left(\frac{fv}{c} \right) \sin \alpha \cos \beta + \left(\frac{f}{c} \frac{2\pi R_e \cos \lambda}{P} \right) \sin \chi \sin \zeta \quad , \quad \text{A}$$

where

- f = channel center frequency
- v = spacecraft speed
- c = speed of light
- α = nadir angle of scan
- β = azimuth angle of scan, relative to velocity vector

R_e = radius of Earth
 λ = latitude
 P = period of Earth rotation
 χ = Earth incidence (zenith) angle
 ζ = Earth azimuth angle

For CMIS measurements near 60 GHz with a satellite altitude near 833 km, the maximum shifts due to satellite motion and Earth rotation are 1.10 MHz and 0.07 MHz, respectively.

The component due to satellite motion is maximized for scan azimuth in the direction of satellite motion (forward or backward) and is minimized at the edge of scan. CMIS is required to be capable of operating in either direction of motion, so a total shift of about ± 1.17 MHz must be accommodated. This total shift has a significant amplitude with respect to the spectral features of the radiative signal used for high altitude temperature sounding (Figure 3-4). The component due to Earth rotation is significant for spectral channels that sense near the sharpest features of the Zeeman-split O_2 spectrum.

One option for dealing with the Doppler shift is to tune the receiver to track the Doppler shift as the satellite scans. There are some technical problems associated with ensuring that the tracking mechanism does not affect the gain of each channel and, thus, degrade the calibration. In addition, when tracking is used, the passband for a given channel is different between the calibration target view and each Earth-scene view. These frequency offsets may introduce calibration errors.

Another option, which is used by CMIS, is to account for the Doppler shift in the temperature retrieval process. To do this, it is necessary to have enough channels and fine enough spectral resolution so that, regardless of the shift at any particular view point, there will be channels positioned in favorable locations with respect to the weighting function spectrum. CMIS accomplishes this with digitally processed channels that span 20 MHz with 0.25 MHz resolution. While some of these channels are averaged on the spacecraft to reduce the data rate, the 0.25-MHz resolution is retained throughout the portion of the spectrum where fine spectral structure may occur in the presence of Doppler shift.

3.4.7. Spectral resolution in relation to measurement noise

As discussed in sections 3.4.1 and 3.4.4 above, vertical resolution for temperature sounding tends to be enhanced by finer spectral resolution. The ideal is to cover the relevant spectrum with a series of contiguous, narrow passbands. The reason this situation is ideal can be seen by considering a case where the radiative transfer does not depend on frequency, as is approximately true in atmospheric “windows”. In that case, all passbands within the spectrum have the same radiative signal. However, the noise standard deviation for the passband is related to the bandwidth by the approximation

$$\sigma = \frac{C}{\sqrt{W}}$$

(Ulaby, et al., 1981), where C represents a combination of terms and W is the bandwidth. Suppose a spectrum of total width W_{TOT} is divided into N channels of equal width, $W_i = W_{TOT}/N$. Separate passbands provide independent measures of the same signal, in this case, and their data can be averaged to reduce data noise. When N noisy measurements are averaged, the noise of the average value is computed from

$$\sigma_{\text{AVG}}^2 = \frac{1}{\sum_{i=1}^N \frac{1}{\sigma_i^2}}.$$

For this case of measurements from N passbands, the noise of the average is given by

$$\sigma_{\text{AVG}}^2 = \frac{1}{\sum_{i=1}^N \frac{W_i}{C^2}} = \frac{1}{\sum_{i=1}^N \frac{W_{\text{TOT}}}{N C^2}} = \frac{1}{\frac{W_{\text{TOT}}}{C^2}} = \frac{C^2}{W_{\text{TOT}}}$$

and is independent of N . If a given portion of spectrum is thus divided into successively smaller slices, the noise impact of reducing the passband widths is completely offset (within the approximation of Equation X) by the effect of having more independent samples. In the case where the optical properties vary strongly with frequency (such as near the center of an O_2 line), it is better to have the spectrum sliced more finely so that each sample is representative of a minimal range of atmospheric altitudes. The noise for each slice (channel) may be very high, but the effective noise of the whole set of channels is unchanged by the finer slicing. In the sounding case, the noise reduction is accomplished not by simple averaging, but by the weighted averaging that is implicit when all the channels are included in the profile retrieval.

There ultimately are limits to the advantages of finer slicing of the spectrum, since noise is not strictly proportional to the square-root of the bandwidth. Furthermore, when the passbands become narrow relative to the scale of atmospheric spectral features, then further narrowing provides no benefit for vertical resolution of atmospheric temperature.

3.5. Instrument Characteristics

3.5.1. Instrument overview

CMIS is a conically-scanning microwave radiometer with window channels—frequencies chosen to avoid atmospheric absorption lines—at 6.8, 10.7, 19, 37, and 89 GHz and atmospheric sounding channel families at 23, 50-60, 166, and 183 GHz. The instrument rotates continuously at 31.6 rpm on an axis perpendicular to the ground, taking observations along nearly semi-circular arcs centered on the satellite ground track. Successive arcs scanned by a single sensor channel are separated by about 12.5 km along-track (depending on satellite altitude.) Calibration data is collected from a source (hot) and deep-space reflector (cold) viewed during the non-earth-viewing portion of the rotation cycle. Each observation (or sample) requires a finite sensor integration time which also transforms the sensor instantaneous field of view (IFOV)—the projection, or footprint, of the antenna gain pattern on the earth—into an observation effective field of view (EFOV). The sample time, which is the interval between starts of successive samples, is slightly longer than the integration time. The sample time is 1.27 ms for all channels with the exception of 10.7 GHz (exactly twice 1.27 ms) and 6.8 GHz (four times 1.27 ms.) All samples fall on one of 4 main-reflector scan-arcs or a single secondary-reflector scan arc (166 and 183 GHz channels families only).

Sensor sample processing described in ATBD Vol. 1, Part 2, sec. 2 (Footprint Matching) creates composite measurements that are the spatial weighted superpositions of a contiguous group of sensor samples. The process is designed to match observations from different channels to a single reference footprint. The composite fields-of-view (CFOVs) from different channels are more closely matched and collocated than the corresponding EFOVs. In addition, because

sensor noise (as measured in NEDT) is both random and independent between samples, the effective NEDT of composite footprints may be reduced if the square-root of the sum of squared sample weights is less than one. The atmospheric vertical temperature profile algorithm uses data processed to match both 40×40 and 200×200-km CFOVs.

3.5.2. Channel set

The primary CMIS channels for retrieving the temperature profile EDR are the ones in the 50–60 GHz range, which were optimized for this task. The optimization accounted for the sensitivity of bandpass-averaged radiometric data to temperature profile structure and for the dependence of NEDT on bandwidth. The optimization was tailored to the earth incidence angle (EIA) of the CMIS conical scan and balanced performance over a variety of environments and surface types. For channels sensitive to the Zeeman effect, the optimization covered a variety of view geometries in relation to the geomagnetic field. The same optimization method was applied to the data from the FFT to determine the optimal way to average data across FFT bins to reduce the data rate, while considering the full range of Doppler shifts. An outline of the method is in Appendix 1 of ATBD Vol. 3.

The temperature profile retrieval at lower altitudes depends, in a secondary manner, on CMIS channels at 10, 19, 23, 37, 89, 166, and 183 GHz to provide information on surface characteristics, water vapor, and cloud water that may affect radiative transfer in the 50–60 GHz band.

The CMIS spectral bands for the nine channels that are used for sounding the lowest levels of the atmosphere are illustrated in Figure 3-6. The width of the lowest-frequency channel is constrained by frequency spectrum allocations that would make a wider channel susceptible to electromagnetic interference from communications systems. Note that the optimized passbands tend to be in “valleys” of the optical depth spectrum where the optical depth varies relatively little as a function of frequency. For sounding at higher altitudes, it is necessary to have channels near the centers of the absorption lines. The spectral bands for four CMIS channels near the 7⁺ (60.4348-GHz) O₂ line and for the FFT-derived channels centered on that line are illustrated in Figure 3-7 and Figure 3-8, respectively. The bands illustrated in Figure 3-8 include the averaging from 80 to 40 FFT bins. Weighting functions for all the 50–60 GHz channels are in Figure 3-9.

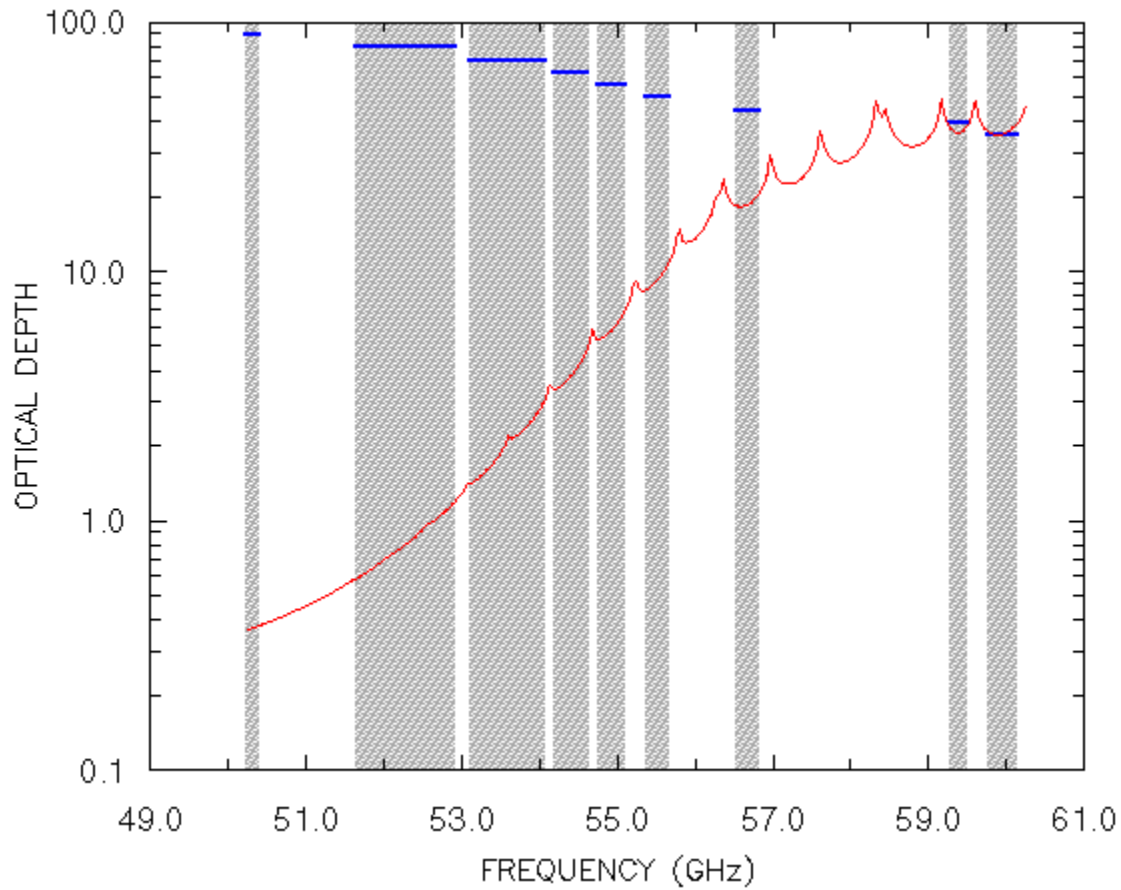


Figure 3-6 Passbands (3-dB limits) for temperature profiling channels for the lowest part of the atmosphere, shown as blue lines and gray bars. The optical depth of a sample atmosphere is shown for reference.

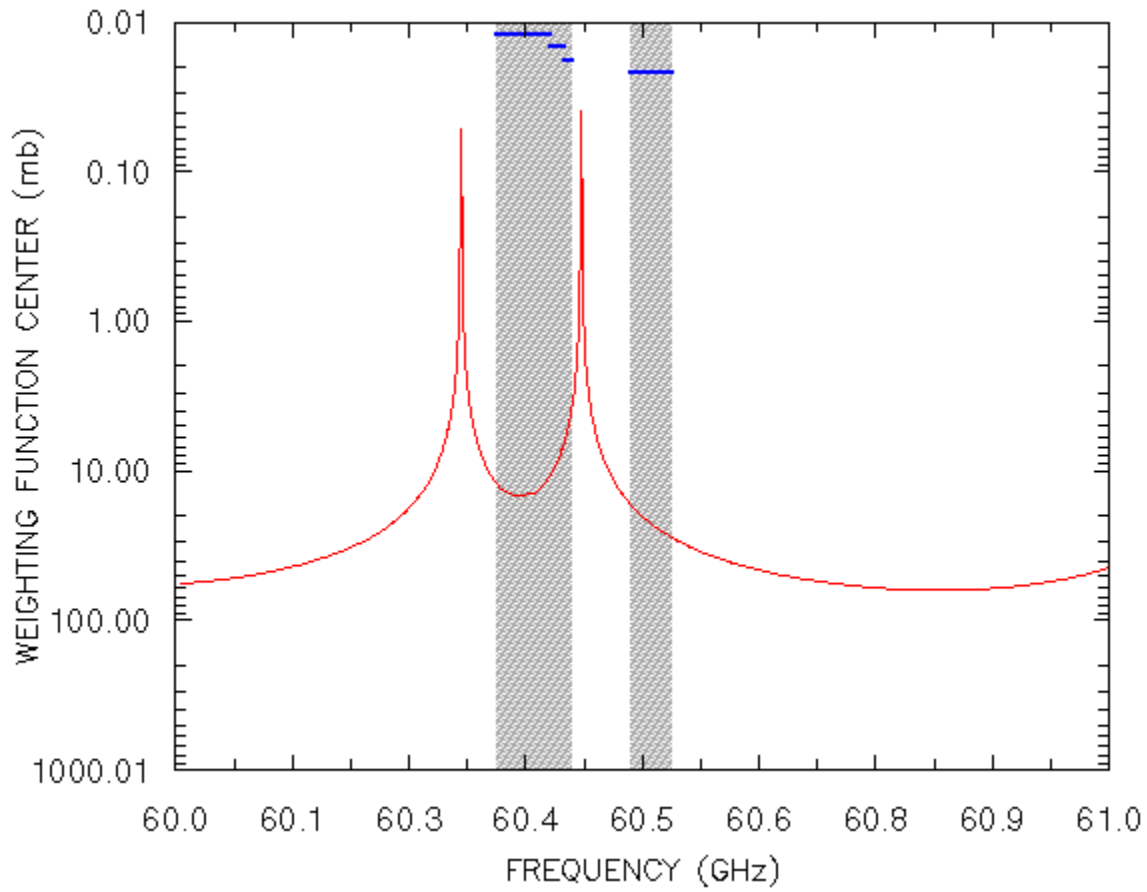


Figure 3-7. Passbands (3-dB limits) for temperature profiling channels for the middle part of the profiled atmosphere, shown as blue lines and gray bars. The weighting function center of a sample atmosphere is shown for reference.

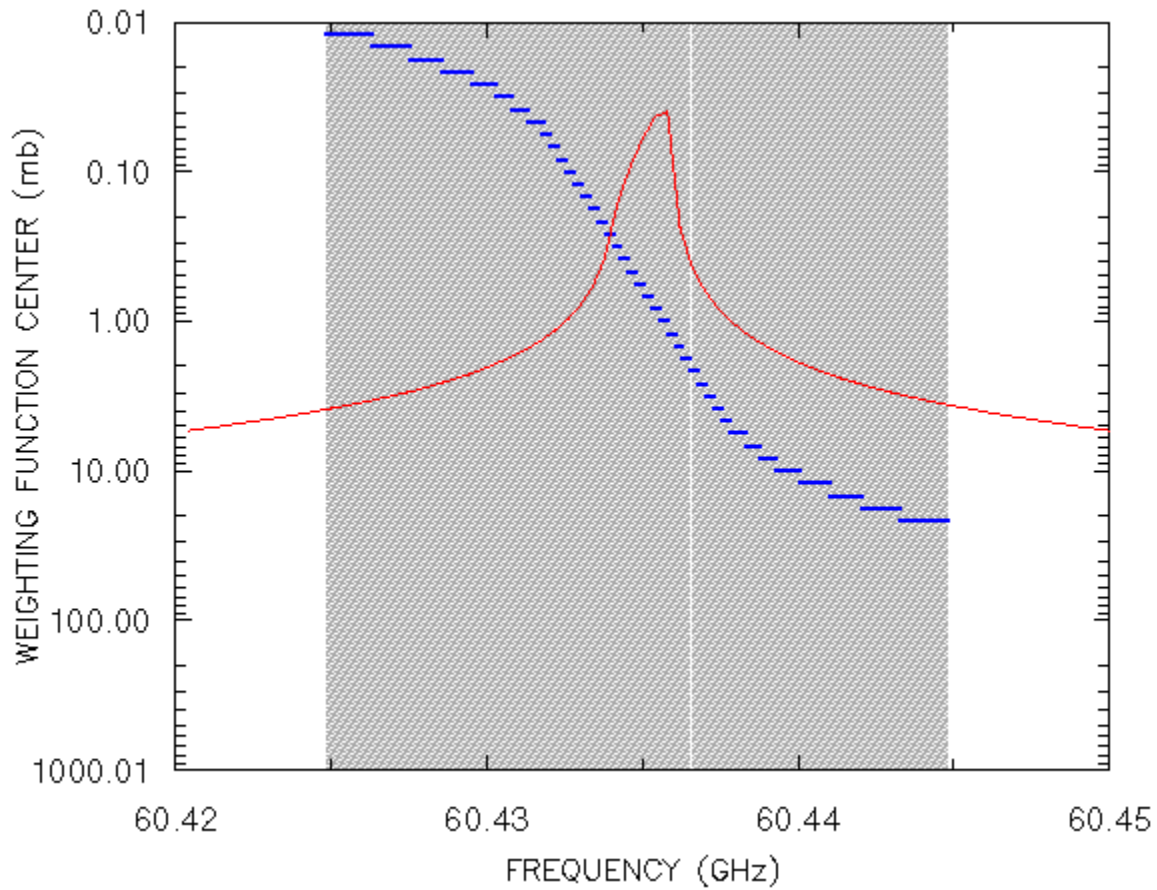


Figure 3-8. Frequency ranges for temperature profiling channels produced by the FFT, which apply to the upper portion of the profiled atmosphere, shown as blue lines and gray bars. The weighting function center of a sample atmosphere is shown for reference.

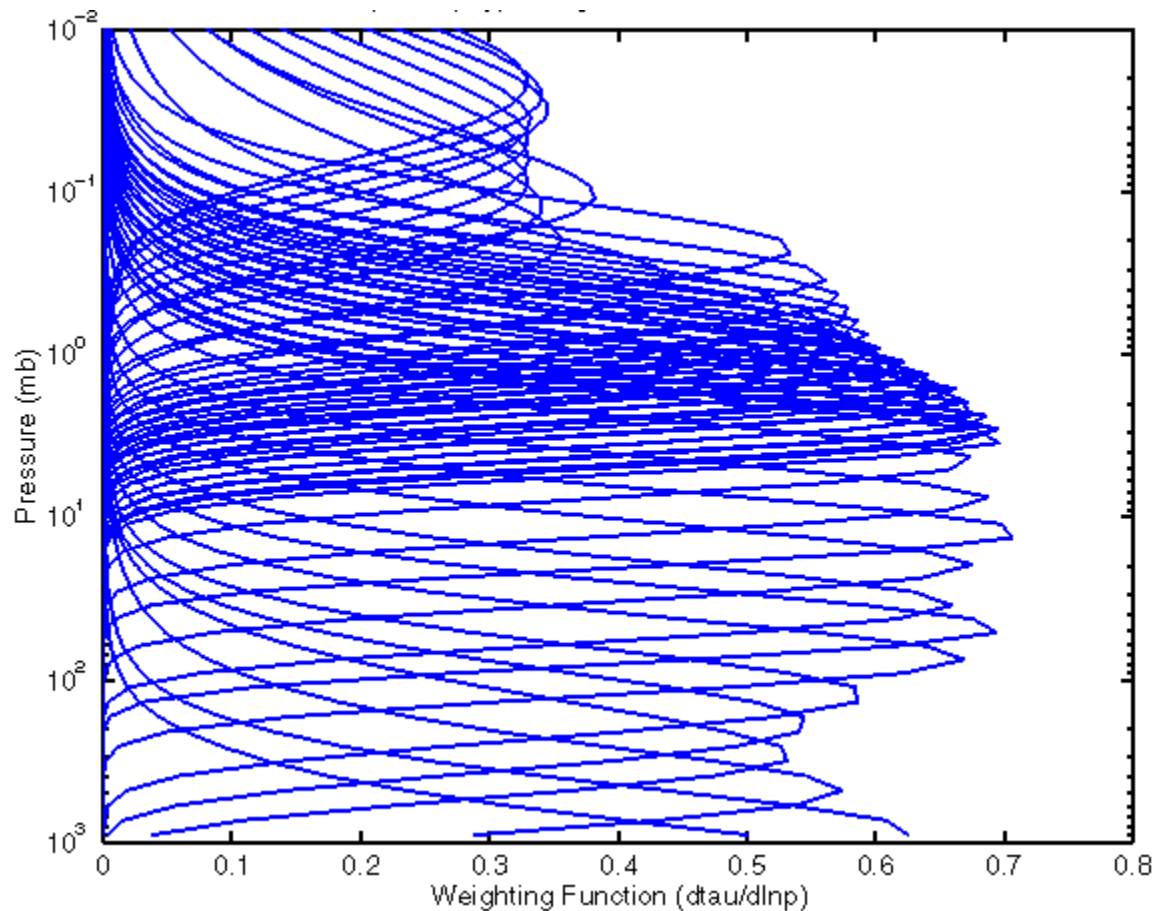


Figure 3-9 Weighting functions for the CMIS temperature sounding channels for the US Standard Atmosphere and a geomagnetic field condition of $|B|=50 \mu\text{T}$, $\theta=135^\circ$.

3.5.3. Derived requirements on sensor data

Derived requirements for Sensor Data Record (SDR) data are listed in Table 3-3. These requirements are associated with computation of the geomagnetic field and the Doppler shift.

Table 3-3. SDR data requirements derived from the AVTP algorithm

SDR Data	Requirements
Latitude/longitude at surface	5 km uncertainty
Earth incidence angle	0.2° uncertainty
Earth azimuth angle	1.3° uncertainty
Scan azimuth angle	0.1° uncertainty
Nadir angle of 60-GHz band	0.1° uncertainty
Satellite forward speed	100 m/s uncertainty
Time/date	24 h uncertainty

3.6. Requirements for cross sensor data (NPOESS or other sensors)

The temperature profile algorithm does not require any data from sensors other than CMIS.

3.7. Derived requirements on data from other EDR algorithms

The AVTP algorithm requires view-path temperature profile data from the core module with the characteristics specified in Table 3-4. The AVTP algorithm also uses view-path water vapor profile data from the core module, for vertical registration, but places no practical requirement on its measurement uncertainty.

Table 3-4: Temperature data requirements placed on the Core Module by the AVTP algorithm under nominal conditions

Parameter	Requirement
a. Horizontal spatial resolution	44 km
b. Horizontal reporting interval	20 km
c. Vertical cell size	
Clear	
1. Surface to 300 mb	1 km
2. 300 mb to 30 mb	3 km
3. 30 mb to 20 mb	5 km
Cloudy	
5. Surface to 700 mb	1 km
6. 700 mb to 300mb	1 km
7. 300 mb to 30 mb	3 km
8. 30 mb to 20 mb	5 km
d. Vertical reporting interval	
1. Surface to 850 mb	20 mb
2. 850 mb to 300 mb	50 mb
3. 300 mb to 100 mb	25 mb
4. 100 mb to 20 mb	20 mb
e. Horizontal coverage	Global
f. Vertical coverage	Surface to 20 mb
g. Measurement range	162-335K
h. Measurement Uncertainty	
Clear	
1. Surface to 700 mb	1.6 K / 1 km layers
2. 700 mb to 300 mb	1.4 K / 1 km layers
3. 300 mb to 30 mb	1.3 K / 3 km layers
4. 30 mb to 20 mb	1.5 K / 5 km layers
Cloudy	
5. Surface to 700 mb	2.0 K / 1 km layers
6. 700 mb to 300 mb	1.4 K / 1 km layers
7. 300 mb to 30 mb	1.3 K / 3 km layers
8. 30 mb to 20 mb	1.5 K / 5 km layers
i. Mapping Uncertainty	3 km
j. Swath Width	1700 km

3.8. Requirements for ancillary data

The AVTP algorithm requires geomagnetic field model parameters for use in the module that computes the geomagnetic field as a function of location and time. The parameters are required to provide an uncertainty less than 300 nT in each geomagnetic field component.

4. Algorithm Description

4.1. Theoretical Description of Algorithm

Given a set of radiometric measurements of the atmosphere, the statistically most likely temperature profile is the one that minimizes the cost function

$$J(\mathbf{x}) = (\mathbf{y} - \mathbf{F}(\mathbf{x}))^T \mathbf{S}_y^{-1} (\mathbf{y} - \mathbf{F}(\mathbf{x})) + (\mathbf{x} - \mathbf{x}_0)^T \mathbf{S}_x^{-1} (\mathbf{x} - \mathbf{x}_0) \quad \text{X}$$

(Rodgers, 1976), where \mathbf{x} is the atmospheric state vector that includes the temperature at discrete levels and may include other variables, \mathbf{y} is a vector composed of the radiometric measurements, the operator \mathbf{F} is a radiative transfer model that can be used to compute radiometric data from the state vector, and \mathbf{x}_0 is an *a priori* estimate of \mathbf{x} . The matrices \mathbf{S}_y and \mathbf{S}_x are the error covariances of the radiometric data and the *a priori* data, respectively. The matrix \mathbf{S}_y represents data noise and errors in the radiative transfer model, and is generally taken to be diagonal. An algorithm that solves (X) for \mathbf{x} is a one-dimensional variational method that is closely related to the three and four-dimensional variational methods that are used operationally to assimilate satellite data in numerical weather prediction models (McNally, et al., 2000).

In Equation X, the constraints that stabilize the solution are represented by the *a priori* estimate and its error covariance. If the temperature profile can be estimated very accurately from some data source other than the radiometric data, the expected difference $\mathbf{x} - \mathbf{x}_0$ is small and the corresponding covariance matrix forces the solution to be close to \mathbf{x}_0 . Likewise, if the *a priori* data source can be relied on to provide the correct vertical structure for the temperature profile, that condition is manifested in \mathbf{S}_x by the off-diagonal terms being relatively large in relation to the diagonals, which tends to force the solution to have the same vertical structure as \mathbf{x}_0 . The matrix \mathbf{S}_x should be reflective of the true quality of the *a priori* data so that the solution departs from the *a priori* estimate in response to the radiometric information, without allowing radiometric noise to introduce spurious features.

The AVTP algorithm solves Equation X to obtain the temperature profile, as a function of pressure along the slanted satellite view path. A second component of the algorithm takes a set of these slant-path temperature profiles and performs an interpolation process to register the profile data into alignment with the local vertical. The vertical registration process is illustrated in Figure 4-1.

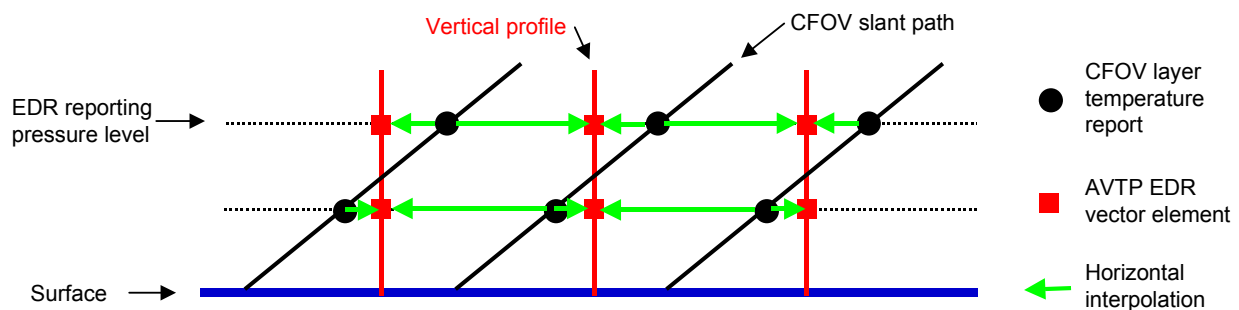


Figure 4-1. Illustration of the process of vertical registration of the temperature profile, for a cross-sectional view through a portion of a scan.

The profile retrieval step is performed separately and before the vertical registration step in order for the retrievals to have the greatest possible fidelity to the radiometric data, avoiding the introduction of interpolation errors. The slant-path retrievals are then available to be

disseminated to CMIS customers that place paramount importance on minimizing temperature profile errors, and for whom slant-path data are fully acceptable. Such customers may, for example, interpolate the slant-path profiles obtained from CMIS directly to their own grid. Customers that require vertically-registered data may access the final EDR products.

4.2. Mathematical Description of Algorithm

4.2.1. Profile retrieval

Equation (X) can be solved by Newtonian iteration by expanding \mathbf{F} in a Taylor series to yield

$$\mathbf{x}_{n+1} = \mathbf{x}_0 + \mathbf{S}_x \mathbf{K}_n^T (\mathbf{K}_n \mathbf{S}_x \mathbf{K}_n^T + \mathbf{S}_y)^{-1} [(\mathbf{y} - \mathbf{y}_n) + \mathbf{K}_n (\mathbf{x}_n - \mathbf{x}_0)] , \quad \text{Y}$$

where n is the iteration index, $\mathbf{y}_n = \mathbf{F}(\mathbf{x}_n)$, and \mathbf{K}_n is the Jacobian matrix composed of the partial derivatives $\partial \mathbf{y}_n / \partial \mathbf{x}_n$ (Rodgers, 1976). This expression represents the primary process of the AVTP profile retrieval algorithm.

The temperature profile retrieval for the lower portion of the atmosphere (surface to 20 mb) is performed by the Core Physical Inversion Module, which is described in the ATBD for the Core Physical Inversion Module (Vol. 2). That module incorporates retrieval of water vapor, cloud, and surface parameters, which factor significantly into lower-atmosphere temperature retrieval.

The upper atmosphere module provides the temperature profile reports in the range 0.01 to 20 mb and, as in the core module, it executes equation Y to perform its retrieval function. The state vector \mathbf{x} is composed of the temperature profile on 66 levels from 0.001 to 200 mb. The state vector spans a broader range of pressures than are reported for the EDR because the CMIS channels that detect temperature in the range 0.01 to 20 mb have weighting functions broad enough that some radiative signals originate outside that range. If temperatures outside that range were not retrieved, the radiative transfer portion of the retrieval algorithm would have to make some assumption about the temperatures. Any discrepancies between the assumed and true temperatures would introduce errors in the computed brightness temperatures and the algorithm would respond by erroneously changing the temperatures in the range 0.01 to 20 mb.

The measurement vector \mathbf{y}_n for the upper atmosphere is composed of brightness temperatures for the channels (60LL, LM, LU, LV, and LFFT) whose weighting functions peak near 20 mb or above.

The baseline *a priori* temperature profile for the upper atmosphere temperature retrieval is a global mean. The use of a global mean minimizes the dependence of the algorithm on external data since *a priori* data do not have to be provided in real time for each CMIS orbit. The algorithm can be adapted to use a local mean (dependent on latitude and longitude) profile derived from a climatology such as the MSISE model (Hendin, 1991). If a reliable, timely, independent source of temperature profile data becomes available, the algorithm can be readily adapted to ingest those data to use as the *a priori* estimate.

If local mean or time-varying profiles are used for the *a priori* estimates, it is difficult to correctly specify the error covariance since reliable statistics describing the variability about the *a priori* values are often unavailable. A trial-and-error method can be used to empirically tune the covariance to improve retrieval performance. When a global mean is used as the *a priori* profile, the *a priori* error covariance is the global covariance of temperature profiles. In other

words, the uncertainty in the *a priori* estimate is equal to the global variability of temperature profiles.

Ideally, the global mean and its covariance should be derived from a large set of temperature profile observations that are statistically representative of global conditions. The observations should have vertical resolution finer than the resolution CMIS so that the retrievals are not unnecessarily smoothed, and should extend to the full range of pressures represented in the state vector. Such a database does not exist for the upper atmosphere. Rocketsonde reports infrequently extend above about 0.02 mb and do not provide global coverage. Ground based lidar remote sensors have been operated in only a few locations. Satellite remote sensors, such as the Microwave Limb Sounder on the Upper Atmosphere Research Satellite (Fishbein, et al., 1996), have not had the necessary combination of accuracy, vertical resolution, and vertical coverage.

The baseline *a priori* profile and covariance were derived from a set of 84 rocketsonde profiles (Rosenkranz, et al., 1997) that extended to at least 80 km altitude (about 0.01 mb). This dataset is relatively good with respect to vertical resolution and vertical coverage, but the number of profiles is small and the horizontal coverage is limited to latitudes lower than 40°. Augmentation of this database has been identified as a pre-launch task.

4.2.2. Upper atmosphere radiative transfer

The algorithm execution involves radiative transfer computations to obtain \mathbf{y}_n and \mathbf{K}_n at each iteration. Each element of \mathbf{y}_n and each row of \mathbf{K}_n corresponds to one CMIS channel. Each channel responds to incident radiation according to its spectral gain function, which describes the sensor gain as a function of frequency. If the normalized gain at frequency f for channel j is $g_j(f)$,

the brightness temperature T_{Bj} for the channel is $T_{Bj} = \int_{a_j}^{b_j} T_{BM}(f) g_j(f) df$, where the limits of

integration a_j and b_j correspond to the range of f where $g_j(f)$ is non-zero. Here, the subscript M denotes the motion of the receiver relative to the atmosphere, which affects the brightness temperature measured at any given frequency in accordance with the Doppler effect discussed in Section 3.4.6. For the upper atmosphere algorithm, Doppler shifting is a significant factor in the radiative transfer. A transmitted brightness temperature $T_B(f)$ will be received as $T_{BM}(f+\Delta)$,

where Δ is the Doppler shift, so $T_{BM}(f) = T_B(f-\Delta)$, and thus $T_{Bj} = \int_{a_j}^{b_j} T_B(f-\Delta) g_j(f) df$. In this

equation, the spectrum of transmitted atmospheric radiation is shifted. A discretized version of this equation could be used in the AVTP algorithm, but it is more convenient from a computational standpoint to make the change of variables $f' = f - \Delta$ and rewrite the equation as

$T_{Bj} = \int_{a_j-\Delta}^{b_j-\Delta} T_B(f') g_j(f'+\Delta) df'$. Since f' is a dummy argument, the prime symbol can be

dropped at this point. In this form, the atmospheric T_B spectrum can be computed without any adjustment of the oxygen absorption line positions, and the integration over frequency is done as if it were the gain function doing the shifting. With this approach, the algorithm does not “correct for” Doppler shifting, since it does not attempt to adjust the sensor or the measured brightness temperatures to remove the Doppler effect. Instead, the algorithm adapts so that its computed T_B values are consistent with the Doppler-shifted radiation being measured.

The baseline algorithm performs monochromatic radiative transfer at evenly spaced intervals of frequency within each channel passband and the results are averaged with weighting given by the spectral gain function of the channel. This is a relatively slow, but straightforward computational approach. The method of Optimal Spectral Sampling employed in the Core Module holds the potential to speed the computations, although the method requires modification to accommodate the influences of Zeeman line splitting and Doppler shifting.

The monochromatic radiative transfer is computed according to the equations presented by Rosenkranz and Staelin (1988). The final brightness temperature is computed from

$$T_B = T_{BLOW} + \sum_{i=1}^n (\tau_i - \tau_{i-1}) \bar{T}_i,$$

where T_{BLOW} is the brightness temperature for the lower part of the atmosphere, \bar{T}_i is the average temperature of atmospheric layer i , τ_i is the transmittance matrix, and layer n is at the top of the atmosphere. The slant path geometry is included by multiplying the propagation coefficients by the secant of the Earth incidence angle in the course of computing τ . T_{BLOW} is computed by scalar radiative transfer and represents the upwelling brightness temperature at the top of the portion of the atmosphere where the Zeeman effect can be neglected. In the baseline algorithm, the transition level is set to 100 mb, although that level is likely lower in the atmosphere than is necessary and the computations could be sped up by raising the level. The brightness temperature derivatives used to compose \mathbf{K}_n are computed with the approximation that τ is independent of temperature, so $\partial T_B / \partial \bar{T}_i = (\tau_i - \tau_{i-1})$, although τ is recomputed, with updated temperatures, at each iteration. The derivatives at the retrieval levels are obtained from the layer-average temperature derivatives by

$$\frac{\partial T_B}{\partial T_i} = \frac{\partial T_B}{\partial \bar{T}_i} \frac{\partial \bar{T}_i}{\partial T_i} + \frac{\partial T_B}{\partial \bar{T}_{i+1}} \frac{\partial \bar{T}_{i+1}}{\partial T_i},$$

noting that each level temperature factors into the averages for the layers above and below the level.

4.2.3. Vertical registration

The main process for vertical registration consists of horizontal interpolation from the locations of slant path data to the locations of the reporting grid. Details of the interpolation method are given in the CMIS ATBD Vol. 1, Part 2, sec. 3: Gridding.

4.3. Algorithm Processing Flow

4.3.1. Processing Flow for CMIS Atmospheric Vertical Temperature Profile Algorithm

The processing flow for the Core Module is illustrated in the ATBD for the Core Physical Inversion Module (Vol. 2). Figure 4-2 shows the processing flow for the upper atmosphere portion of the AVTP algorithm. The process for vertical registration of the profile data is illustrated in Figure 4-3.

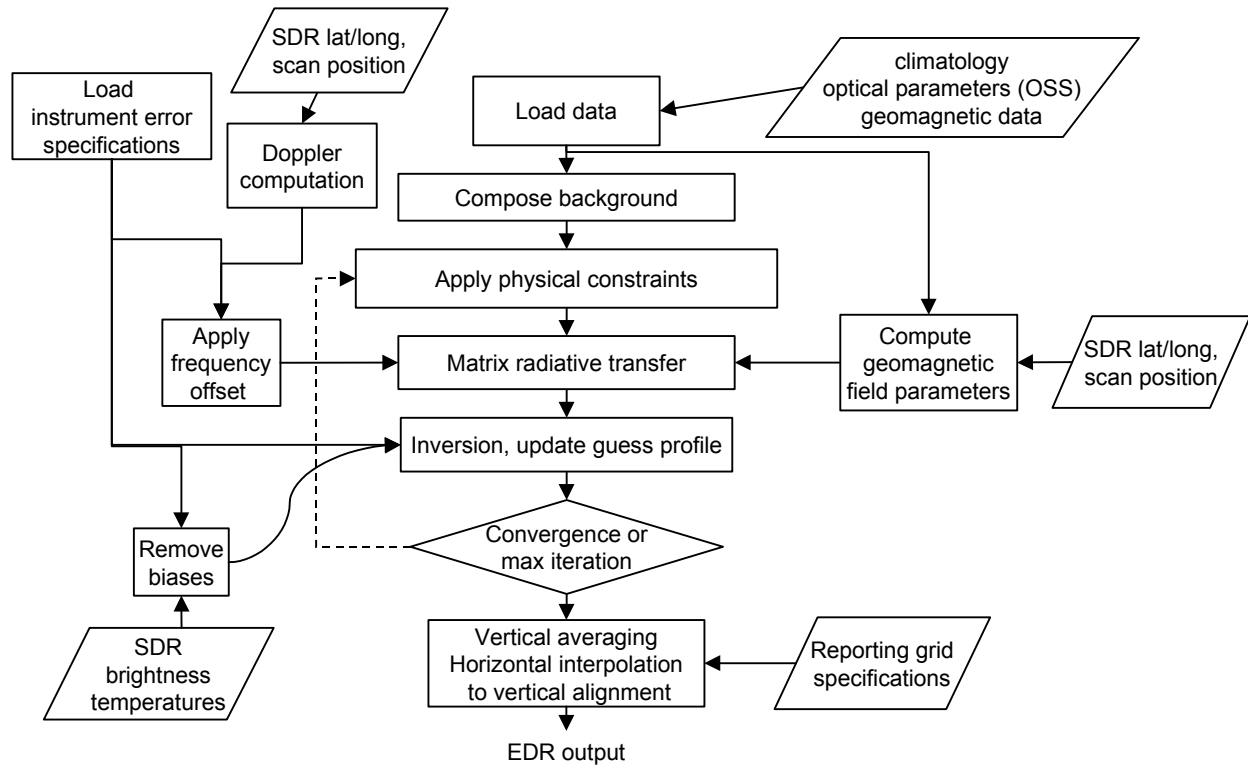


Figure 4-2. Processing flow for the upper atmosphere portion of the AVTP EDR algorithm.

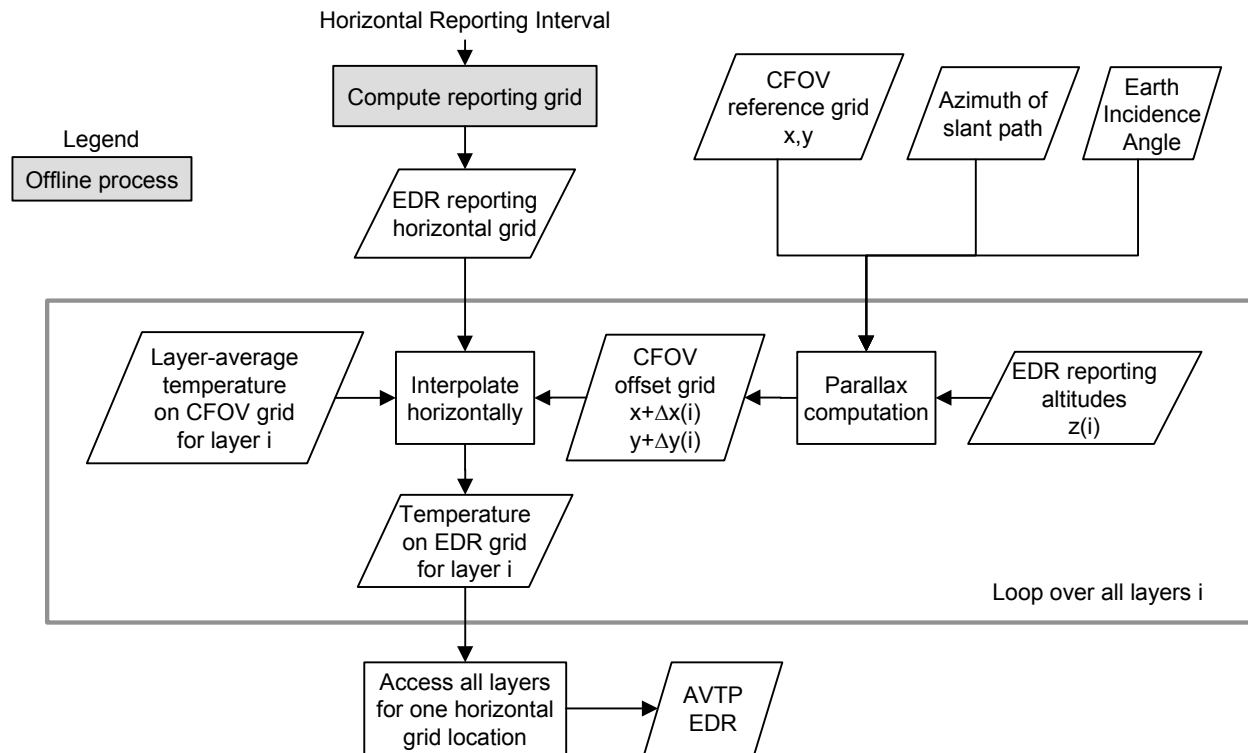


Figure 4-3. Processing flow for vertical registration for the AVTP EDR algorithm.

4.3.2. Relationship to Overall CMIS Processing Flow

The front end of the EDR algorithm set is the footprint matching algorithm, which is described in the Footprint Matching ATBD (ATBD Vol. 1, Part2, sec. 2). That algorithm provides the brightness temperatures to the upper atmosphere temperature profile module. The baseline CFOV size for upper atmosphere processing is 200×200 km².

The upper atmosphere module is responsible for producing the AVTP EDR reports for the pressure range 0.01 to 20 mb, while the core module is responsible for reports in the range 20 mb to the surface (with AVTP EDR postprocessing, in both cases). However, each module retrieves temperatures over a broader range of pressures than its AVTP reporting range. The upper atmosphere module retrieves temperatures from 0.001 to 200 mb, as discussed in Sec. 4.2.1, while the core module retrieves temperatures from 0.1 mb to the surface. The upper atmosphere module provides temperature data to the core module in the overlapping range of 0.1 to 200 mb. The core module statistically combines these temperature data with data from other sources to form the *a priori* estimate for the core module retrievals. By this processes, the retrieved lower atmosphere temperature profile is consistent with the upper atmosphere profile, while allowing the core module to exclude the channels that sense the highest altitudes and to avoid the computational burden of matrix (Zeeman) radiative transfer.

The relationship between the AVTP modules and the overall EDR processing is illustrated in Figure 4-4.

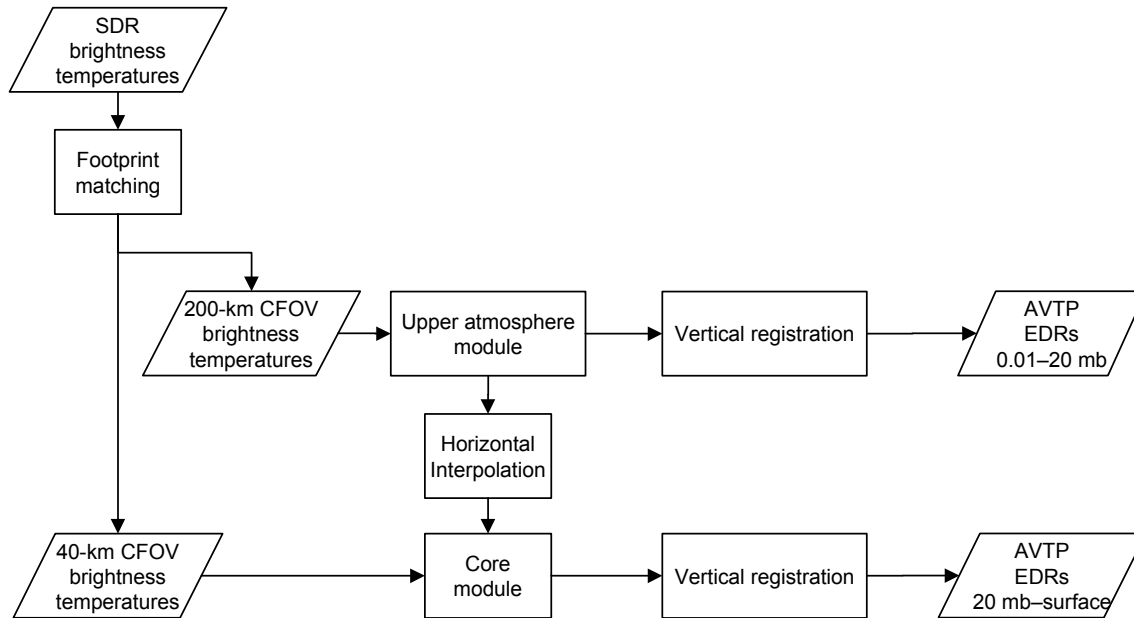


Figure 4-4. AVTP module algorithm flow in relation to other EDR modules.

4.4. Algorithm inputs

Table 4-1. AVTP algorithm inputs

Data	Type	Source	Usage
Brightness temperatures from channels 60HL, 60HM, 60HU, 60HV, and FFT	Dynamic, continuous	Footprint matching algorithm	Upper atmosphere retrieval
Channel spectral gain functions	Static	Sensor description database	Radiative transfer, Doppler computation
Sensor error statistics	Dynamic, episodic	Sensor performance database	Upper atmosphere retrieval
Temperature profile climatological means, covariances	Static	Atmospheric statistics compiler	"
Geomagnetic field parameters	Dynamic, periodic	IGRF geomagnetic database	Geomagnetic computation
Latitude/longitude at surface	"	SDR	EDR reporting, geomagnetic computation, Doppler computation
Time/date	"	SDR	"
Earth incidence angle of 50-60-GHz channels	"	SDR	Radiative transfer, geomagnetic computation
Earth azimuth angle	"	SDR	Geomagnetic computation,

			Doppler computation
Scan azimuth angle	"	SDR	Doppler computation
Satellite forward speed	"	SDR	"
Nadir angle of scan	Static	Sensor description database	"
Slant-path temperature profiles	Dynamic, periodic	Core Module and Upper Atmosphere module	Vertical registration
Slant-path water vapor profiles	"	Core Module	Vertical registration (hydrostatic heights)
CFOV identifier indices	"	Core Module and Upper Atmosphere module	Vertical registration
CFOV reference grid	Static	Scan description database	"
Azimuth of slant path in scan coordinates	"	Scan description database	"
Horizontal reporting grid	"	Specifications database	"
Vertical reporting grid	"	Specifications database	Vertical interpolation

4.5. Algorithm outputs

Table 4-2. AVTP algorithm outputs

Output parameter
Temperature profile
Latitude/longitude at surface
Time/date
CFOV identifier indices
Quality flag

4.6. Timing benchmark

The upper atmosphere baseline module requires about 3.4 s cpu time per iteration on an SGI 195-MHz processor operating on 44 CMIS channels. The bulk of the cpu time is spent on the radiative transfer computations. The baseline algorithm requires two iterations. For a reporting interval of 200 km over a 1700-km swath there are about 2000 profile retrievals per 1.25 orbits. The computation time for 1.25 orbits is therefore 227 min.

There are several means to achieve substantial savings in computation time in the radiative transfer computations, beyond the obvious option to use greater computer power:

- 1) Use more sophisticated spectral sampling to reduce the number of monochromatic computations.
- 2) Tabulate effective opacities (Rosenkranz, 1995) or propagation factors instead of computing them in real time.
- 3) Exploit symmetry of Zeeman effect about line center to reduce computations by a factor of two.
- 4) Reduce the range of pressure levels for which matrix radiative transfer is used (move cutoff up from 100 mb).

- 5) Restrict the computations for each channel to the range of levels known *a priori* to be potential contributors to the signal, rather than using all levels for all channels.
- 6) Use regression to obtain an initial estimate of the temperature profile, thus reducing the number of physical algorithm iterations from two to one.

We expect that, with no change in computing power, these algorithm changes can accomplish one to two orders of magnitude reduction of computation time, which is consistent with the experience of Rosenkranz (1995).

5. Algorithm Performance

The fundamental steps of performance testing are:

- 1) select test cases, with description of temperature profiles and all other relevant environmental parameters,
- 2) simulate CMIS brightness temperatures, accounting for sensor design parameters and error characteristics,
- 3) perform EDR retrievals, and
- 4) compare retrieved EDRs to the “true” EDRs, which are derived directly from the test case data.

The final step involves vertical averaging.

5.1. Vertical averaging

Retrieved and “true” EDRs are vertically averaged, in accordance with the SRD requirements, before computing error statistics. The process for vertical layer averaging is illustrated in Figure 5-1. While the process is denoted in terms of the EDR products, the process is the same for truth data.

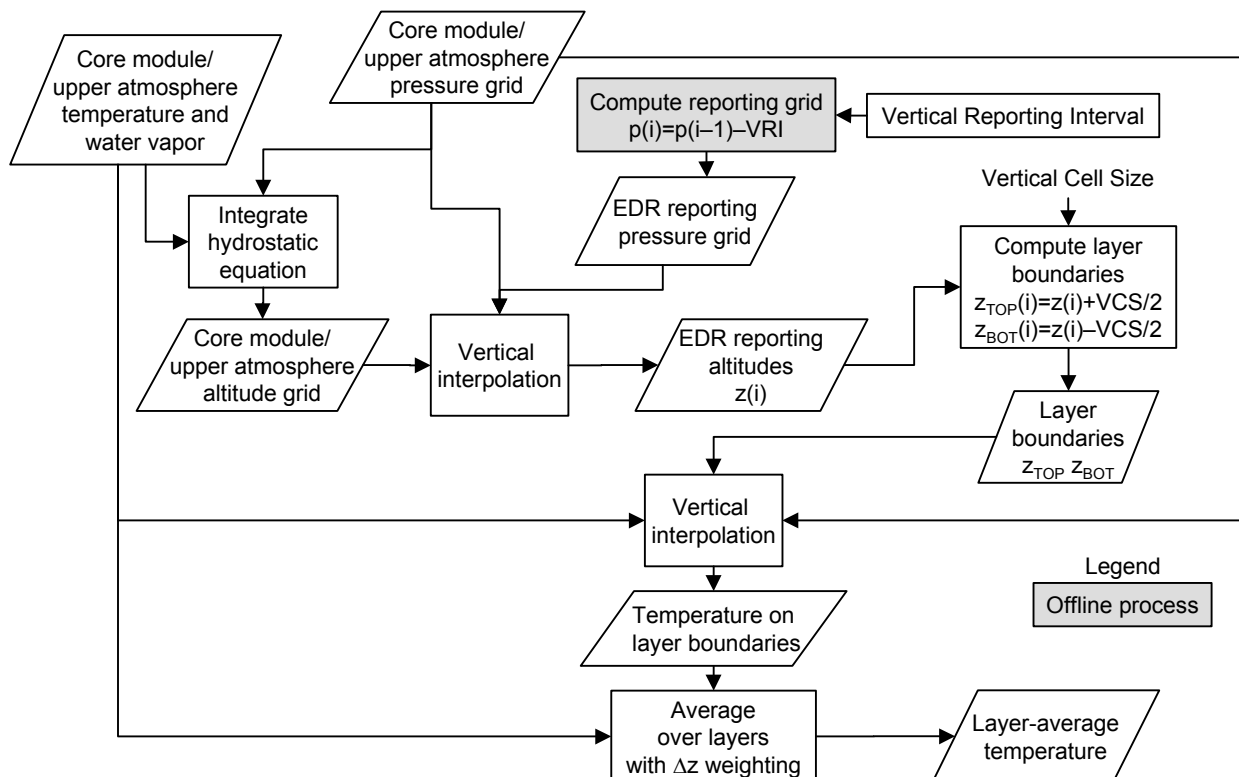


Figure 5-1. Processing flow for vertical averaging for the AVTP EDR validation.

5.2. Lower atmosphere

5.2.1. Performance test conditions

The primary test cases for the lower atmosphere temperature profile are described here briefly and, more extensively, in the ATBD for the Core Physical Inversion Module (ATBD Vol. 2). The atmospheric temperature and water vapor profiles and the surface temperatures were derived from the NOAA-88 database. Liquid clouds were simulated by assuming uniformly-distributed cloud liquid water over a layer whose bounds varied randomly from profile to profile. The total cloud liquid water varied randomly from 0 to 0.5 kg/m². Oceanic profiles were paired with emissivity spectra from the Kohn/Wilheit model. Warm land profiles (surface skin temperature > 273 K) were paired with land emissivity spectra derived from the Prigent database. Cold land profiles (surface skin temperature < 273 K) were paired with snow/ice emissivity spectra also derived from the Prigent database.

5.2.2. Performance overview

Retrieval performance is shown in Figure 5-2, stratified by surface type, latitude, season, and cloud condition. These results were obtained from a set of 1000 ocean profiles and another set of 1000 land profiles from the NOAA-88 dataset. The errors tend to be largest near the surface and near 300 mb. The vertical averaging cell is larger above 300 mb, contributing to the drop in rms error above that level.

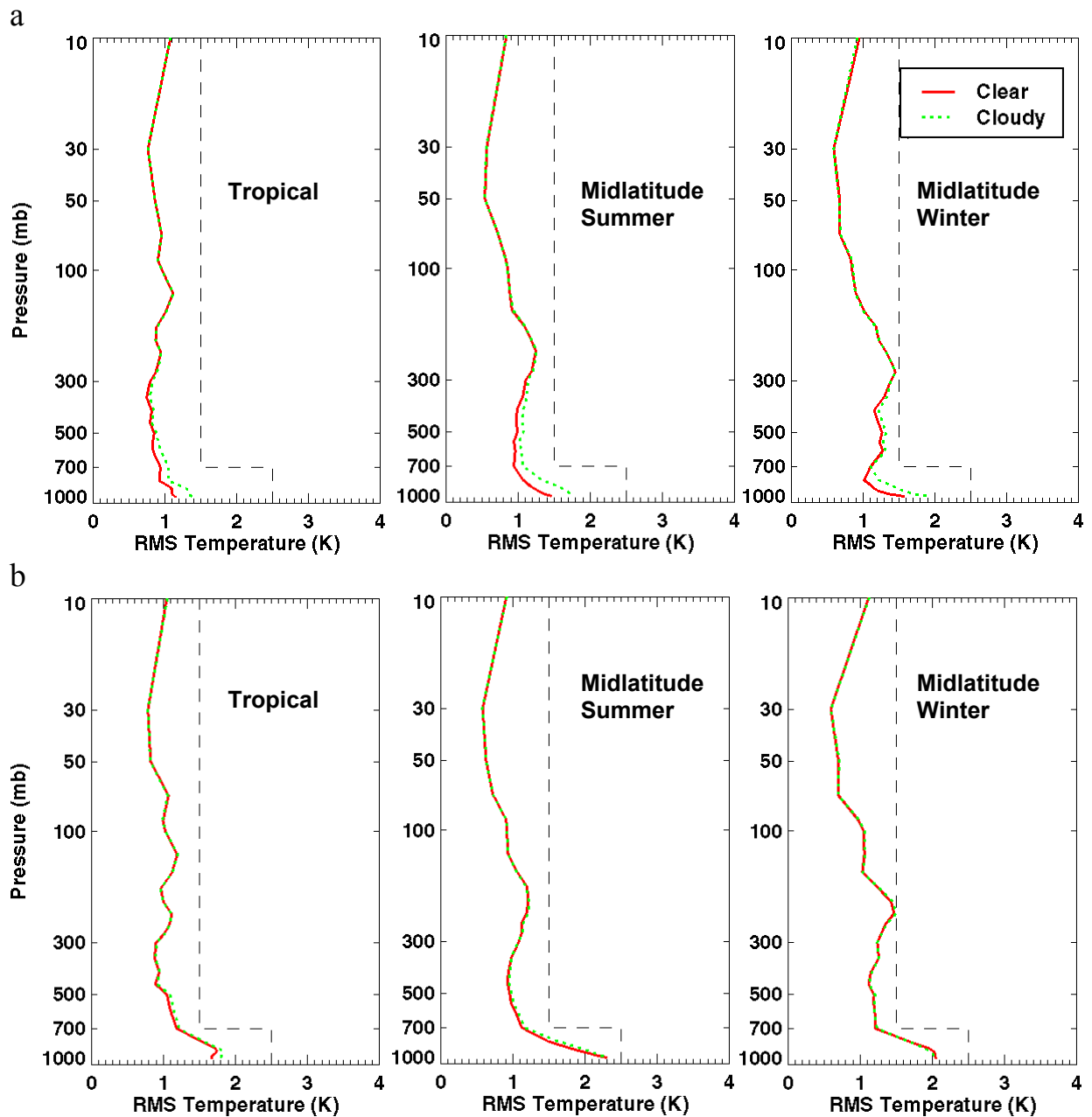


Figure 5-2. Temperature profile retrieval rms error for a) ocean surface and b) land surface, stratified by latitude and season as labeled. Performance is given for data vertically averaged according to the SRD requirements. The drop-off in error just above 300 mb coincides with an increase in the vertical cell size.

The results in Figure 5-2 do not include the affect of air mass preclassification, which is described in CMIS EDR ATBD Volume 2: Core Physical Inversion Module. The impact for the temperature profile is shown in Figure 5-3, where the errors are reduced substantially in the 100-300-mb zone.

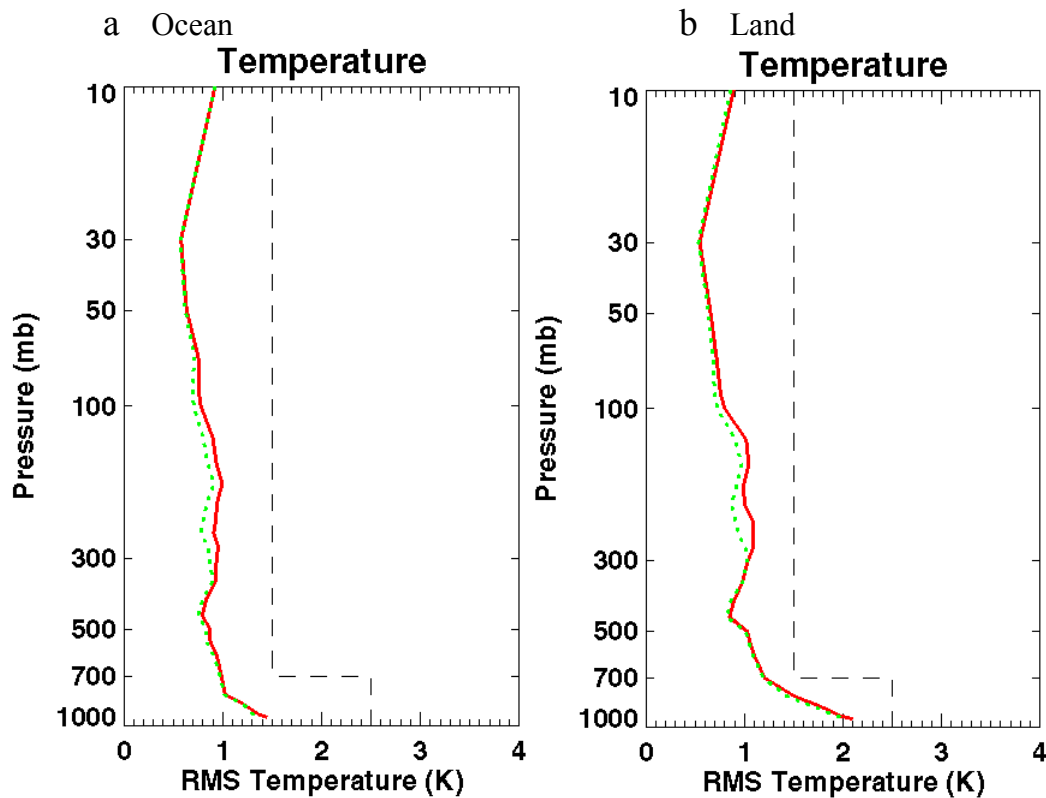


Figure 5-3. Temperature profile retrieval error with a global atmospheric background constraint (red) and an air mass classified background (dashed green) for a) ocean and b) land surface. These results are for a CFOV size of 50 km and, thus, are not directly comparable to the thresholds. The test cases are cloudy.

5.2.3. Sensitivity studies

The temperature profiling performance near the ground is strongly sensitive to the surface type, as manifested in the spectral surface emissivity. This affect is illustrated directly in Figure 5-4, where results are shown for two sets of test cases that were identical except for the surface emissivities. The retrievals over ocean used a background constraint developed from ocean emissivity spectra, and the retrievals over forest used a background developed from a variety of land surfaces. These results, therefore, apply to the case where “global” backgrounds for land and ocean are used.

One of the challenges faced by a temperature profile algorithm is to resolve the ambiguities between temperature signals and signals from other environmental variables, including clouds. Figure 5-4 demonstrates that the problem of ambiguity resolution is more challenging for land surfaces than ocean surfaces. When the retrieval algorithm is given prior information that the atmosphere is cloud-free (cloud parameters are not retrieved), there is a beneficial effect on temperature profiling performance near the surface. That beneficial effect is greater for the land surface, where there are substantial ambiguities between surface emissivity, cloud parameters, and water vapor.

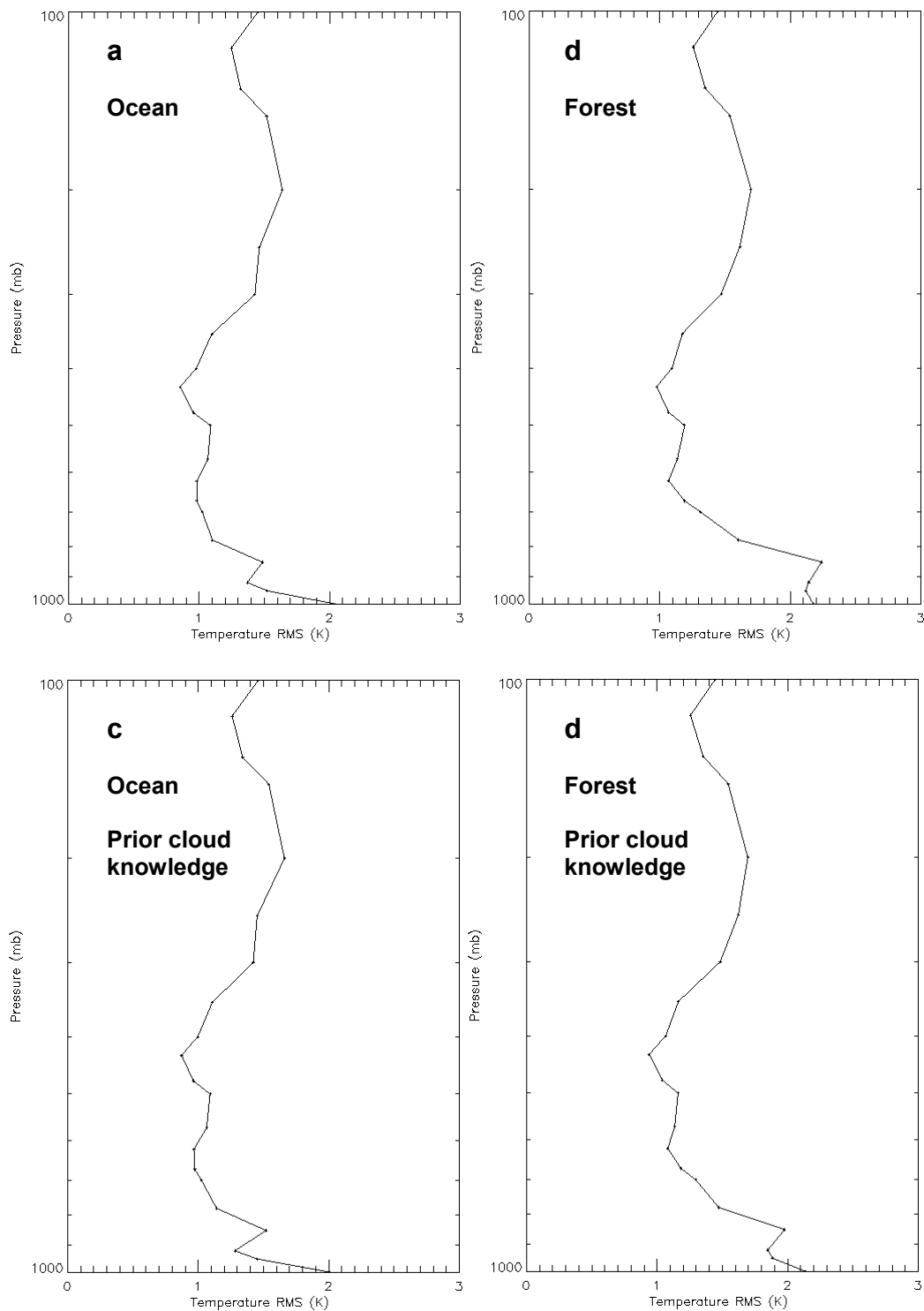


Figure 5-4. Temperature profile retrieval rms error for a set of 230 profiles with NEDT corresponding to a 50-km CFOV. Frames a and c are for ocean background and frames b and d are for a forest background. In frames c and d, cloud was specified to be held constant at the true value (0 cloud liquid water). These results are for a CFOV size of 50 km and were computed without any vertical averaging

5.3. Upper atmosphere

5.3.1. Performance test conditions

The NOAA-88b temperature profiles extended to high altitudes, but the extrapolation/interpolation process used to obtain the high-altitude data resulted in unrealistically smooth profiles (Figure 5-5) that are not useful for testing sounding performance beyond about 1 mb. The primary test cases for the upper atmosphere temperature profile were the set of 84 rocketsonde profiles discussed in Section 4.2.1 (Figure 5-6), which were provided by P. Rosenkranz. These will be referred to as the Rosenkranz profiles in the following discussion.

Two additional test sets were used. One consisted of 12 profiles retrieved from Cryogenic Infrared Spectrometers and Telescopes for the Atmosphere (CRISTA) limb sounder data (Riese, et al., 1999; Kostsov et al., 2001), provided by V. Kostsov. The CRISTA retrievals extended from 37.5 km altitude (about 4 mb) upward. The retrieved profiles were extrapolated downward by regression, trained on the Rosenkranz dataset, to provide data at all levels needed for brightness temperature simulation (Figure 5-7). Because of the extrapolation, the CRISTA dataset is useful for evaluating performance only at pressure levels from about 3 mb upward. Salient features of the CRISTA dataset are the extent of the database beyond the top of the radiative transfer domain (0.001 mb) and the presence of profiles from high latitudes (to 60°). Another test set consisted of 32 rocketsonde profiles (Figure 5-8) gleaned from 20 years of National Climatic Data Center archives, obtained through the National Center for Atmospheric Research (NCAR). We generated this dataset specifically for the purpose of finding high-latitude profiles (which were not present in the Rosenkranz dataset) that extended to high altitudes. There were essentially no profiles available that extended to altitudes fully sufficient for CMIS testing, so we used the ones that extended to at least about 68 km (0.08 mb) and extrapolated above that level.

Note the large degree of variability and sharp vertical structure at high altitudes in the Rosenkranz and CRISTA profiles.

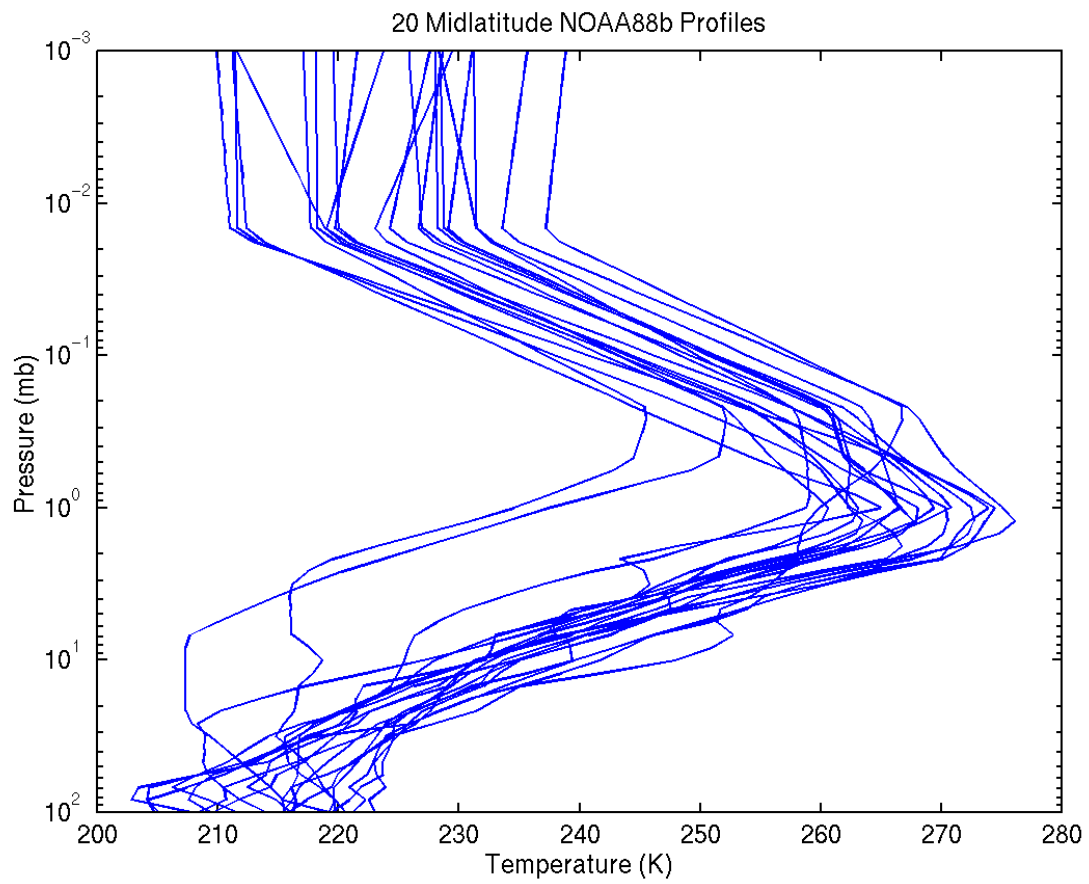


Figure 5-5. A sample of 20 profiles from the NOAA88b dataset.

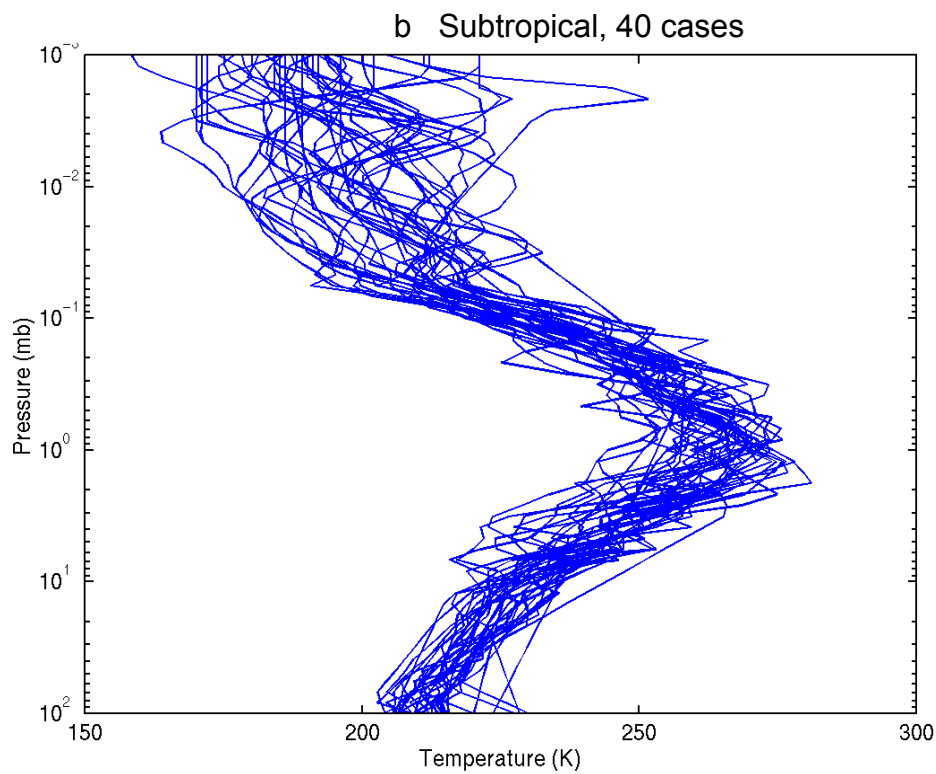
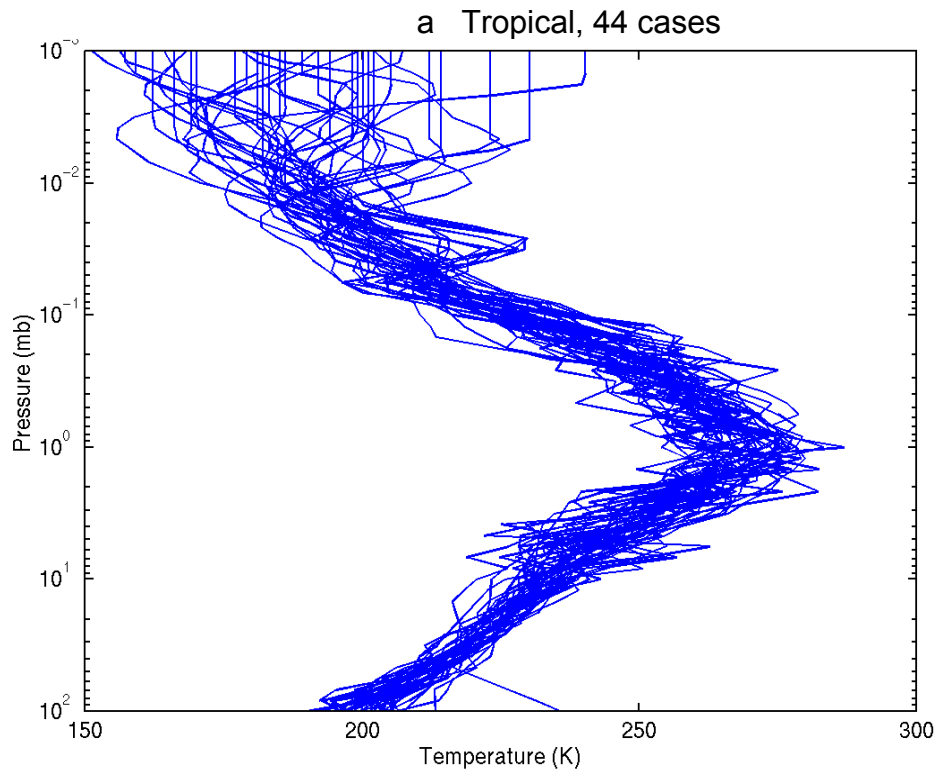
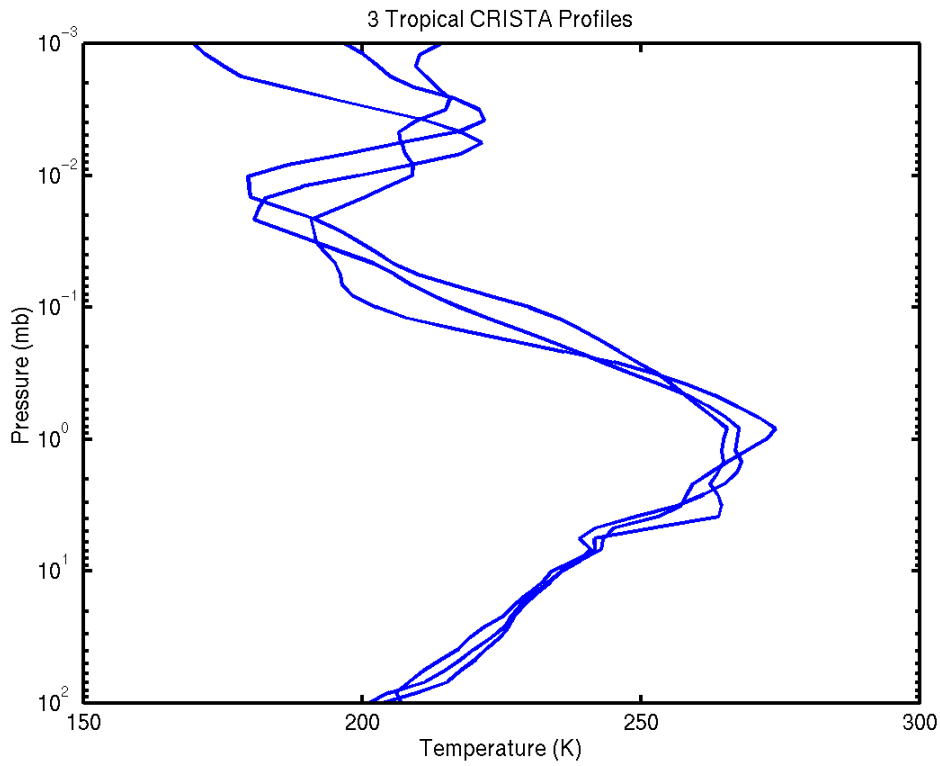


Figure 5-6. The Rosenkranz profiles from latitudes a) lower than and b) greater than 30°. Some of the profiles were extrapolated with constant temperature at the top.

a



b

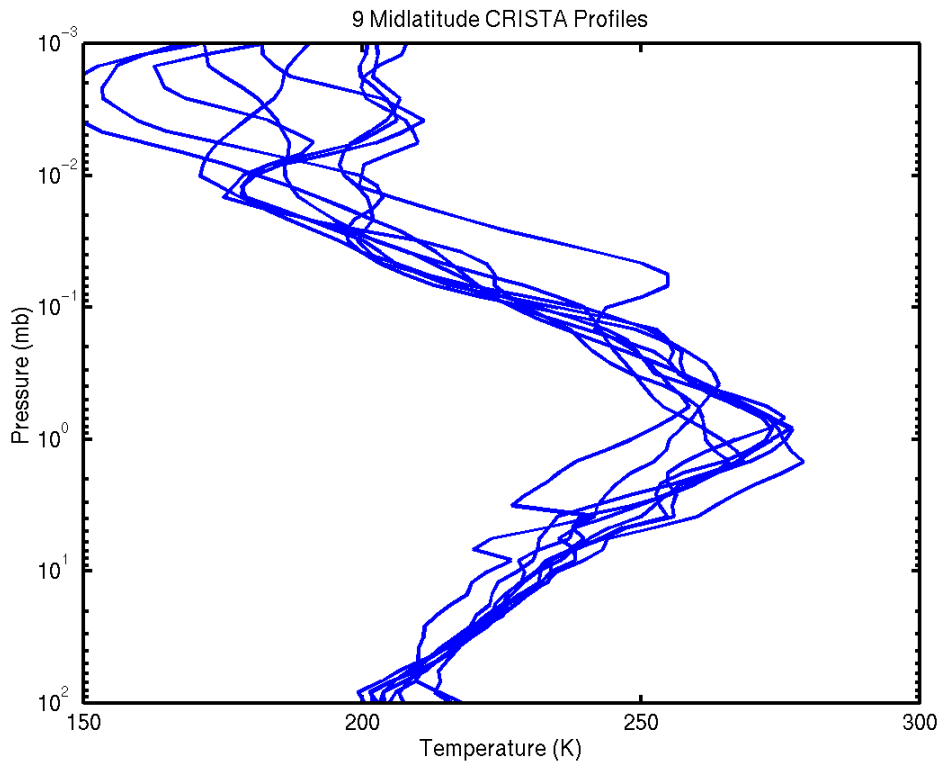
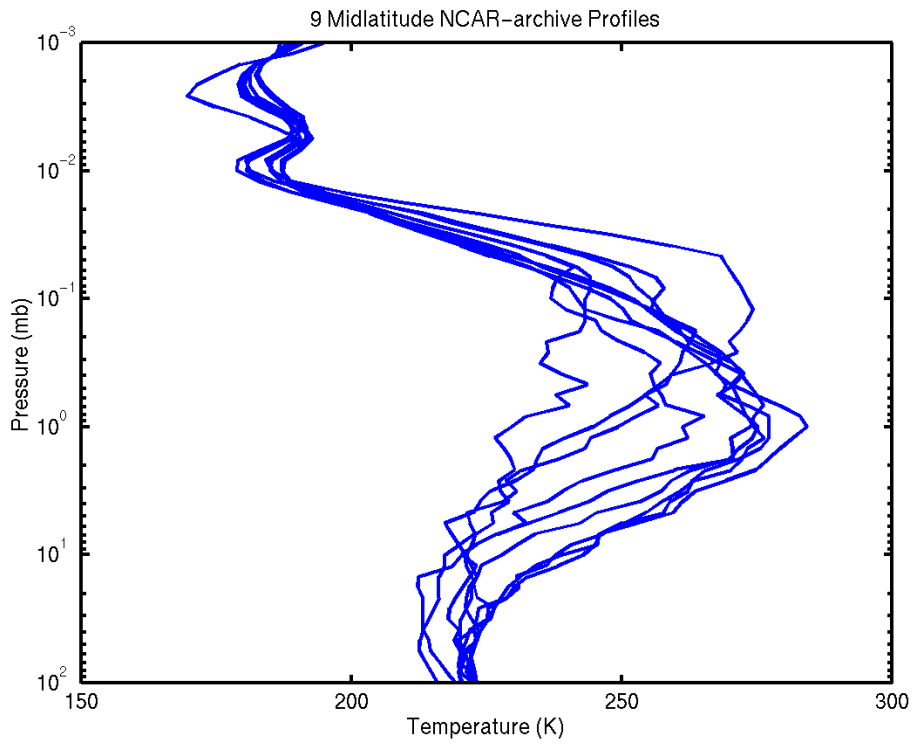


Figure 5-7. The CRISTA profiles from latitudes a) lower than and b) greater than 30° . The profiles were extrapolated downward from about 4 mb.

a



b

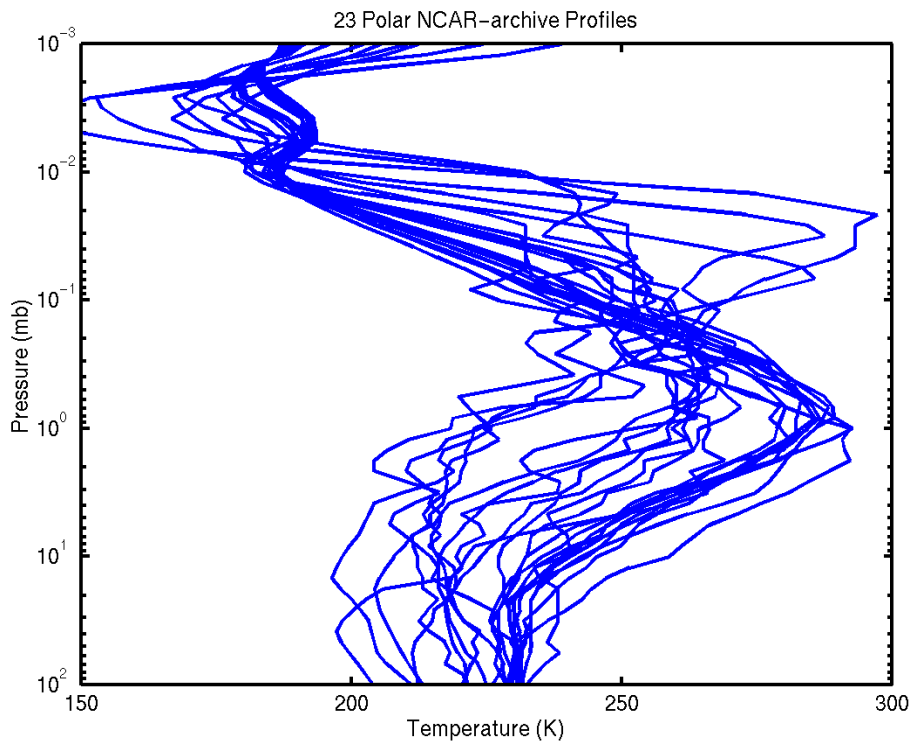


Figure 5-8. The high-latitude rocketsonde profiles from latitudes a) lower than and b) greater than 60° . The profiles were extrapolated upward from about 0.08 mb.

For upper atmosphere retrieval tests, the *a priori* profile and its covariance were computed from three-quarters of the Rosenkranz dataset, while one quarter was reserved as independent data for performing the retrievals. The division between *a priori* and retrieval sets was rotated so that retrieval tests could be performed on all of the profiles, pooling the performance statistics from all the quarters. For some sensitivity experiments, only one of the quarters was processed, as a means to save computation time.

For upper atmosphere simulations, a magnetic field condition must be specified for each profile. The conditions were derived from the International Geomagnetic Reference Field 1995 version. One option would be, for each profile in the dataset, to obtain the geomagnetic field data for the place and time where the sounding was taken. Because the test datasets are small, this would allow for testing under only a few geomagnetic field conditions. As an alternative, we retrieved each profile under a range of geomagnetic conditions, without regard to matching the times or locations. Two methods were used to select the range of conditions.

Method 1

Magnetic field conditions were determined by considering the views that would be obtained in two half orbits starting at the earth equator and crossing over the North Pole. One half orbit was aligned (at the equator) with the longitude to the magnetic pole and the other was displaced 90 degrees in longitude. For each half orbit, views were taken at six evenly spaced points along the half orbit and at three scan azimuth angles (-70° , 0 , and 70°). There were thus a total of 36 ($2 \times 6 \times 3$) geomagnetic field conditions. This method provides a useful sample of conditions, but not a thoroughly representative sample.

Method 2

A frequency distribution of magnetic field conditions was generated from a fine-resolution sampling of global conditions, as discussed in Section 3.4.5. It would not be feasible to compute retrievals for all these conditions, and it is not necessary either, since many of the views generate similar magnetic field conditions. The frequency distribution was gridded with dimensions (6,8,4) in the space of (B, θ, ϕ) . Each grid cell that contained at least 0.27% of all the conditions was taken as a test case. The 112 grid cells that made this qualification comprised 95% (normalized) of all global conditions. Each test case was assigned the values of (B, θ, ϕ) at the center of the cell. When performance statistics were computed, the statistics were weighed by the normalized frequency of occurrence of the cell.

Method 1 was used for some initial sensitivity tests and method 2 was introduced for additional sensitivity tests and performance evaluation. In the results shown below, method 2 was used except as noted otherwise.

Brightness temperature noise was added to each channel using a Gaussian random number generator. The noise amplitude was governed by the channel specifications and modulated by the noise averaging factors introduced in the footprint averaging module. The tests were all performed with noise levels appropriate to the center of scan, where the sampling density is least and the effective CFOV noise is thus at its highest. The nominal tests also included an assumed 20 kHz center frequency knowledge error (difference between center frequency in brightness temperature simulation and in retrieval-process radiative transfer).

5.3.2. Performance overview

During the course of conducting trades-off studies and sensitivity tests, some changes were made to the baseline algorithm configuration and sensor parameters. Performance data shown in this ATBD includes results from varying baselines. The current baseline has left circular polarization in the channels used for upper atmospheric temperature sounding and uses a CFOV size that closely matches the SRD threshold horizontal cell size (200 km). Many of the results shown are from the previous baseline, which had horizontal polarization and a 300-km CFOV. As part of the design change to the current baseline, the NEDT for the relevant channels was decreased modestly and the Earth incidence angle was increased modestly. Within each trade-off or sensitivity test (a plot or set of plots in this document) the baseline was held constant; however, the changing baseline does hinder comparisons from one set of tests to another. The primary differences in the baseline are noted in the discussions below.

Performance for the primary (Rosenkranz) test dataset is plotted in Figure 5-9. The errors are a strong function of altitude.

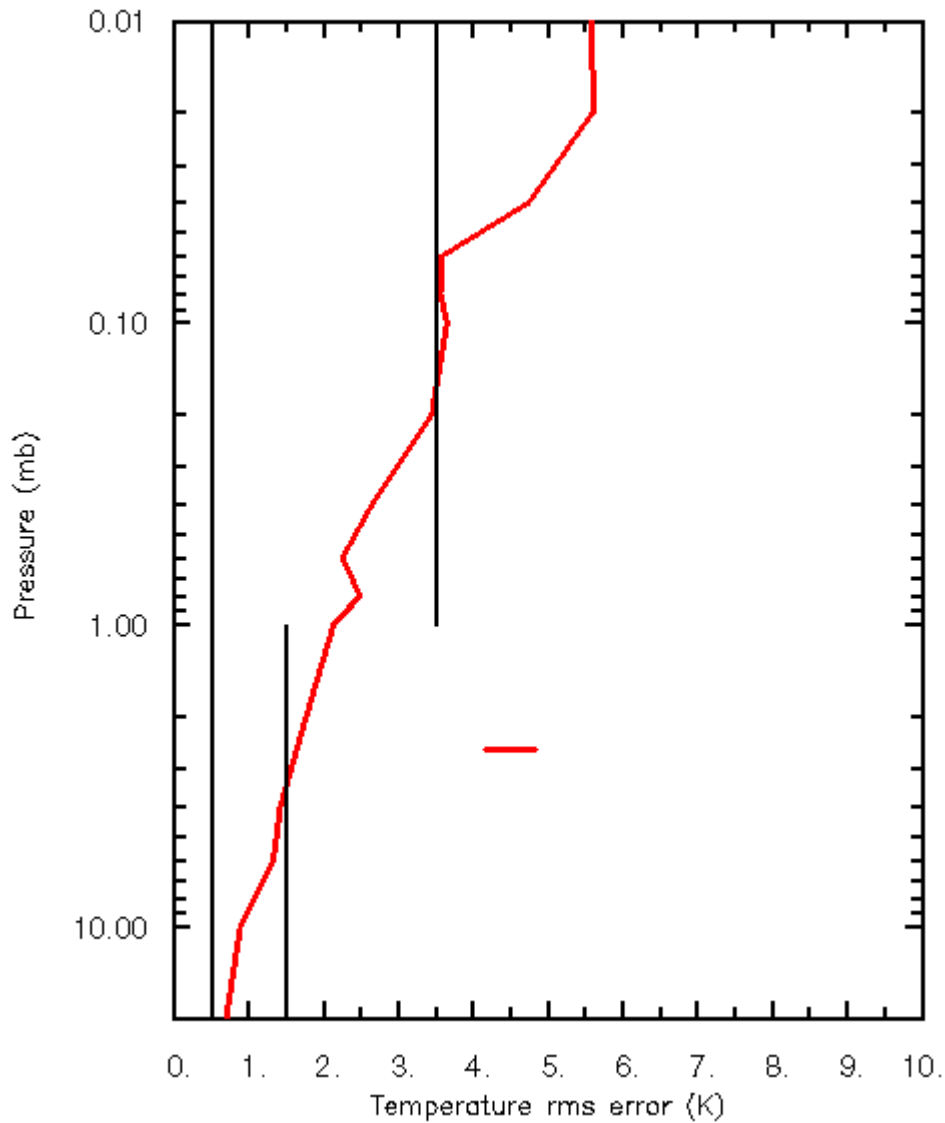


Figure 5-9. Upper atmosphere temperature profile rms error for the current baseline system applied to the Rosenkranz dataset. The errors are for temperatures that have been vertically averaged per the SRD requirements. The broken vertical line at right is the measurement uncertainty threshold and the vertical line at left is the objective.

Performance for H-polarization and varying data noise is shown in Figure 5-10 for the Rosenkranz dataset. Even for essentially noise-free data (solid curve) the measurement uncertainty threshold is not met for pressures lower than about 0.03 mb. The CFOV size, which modulates the CFOV noise, can be tuned in response to CMIS customer priorities.

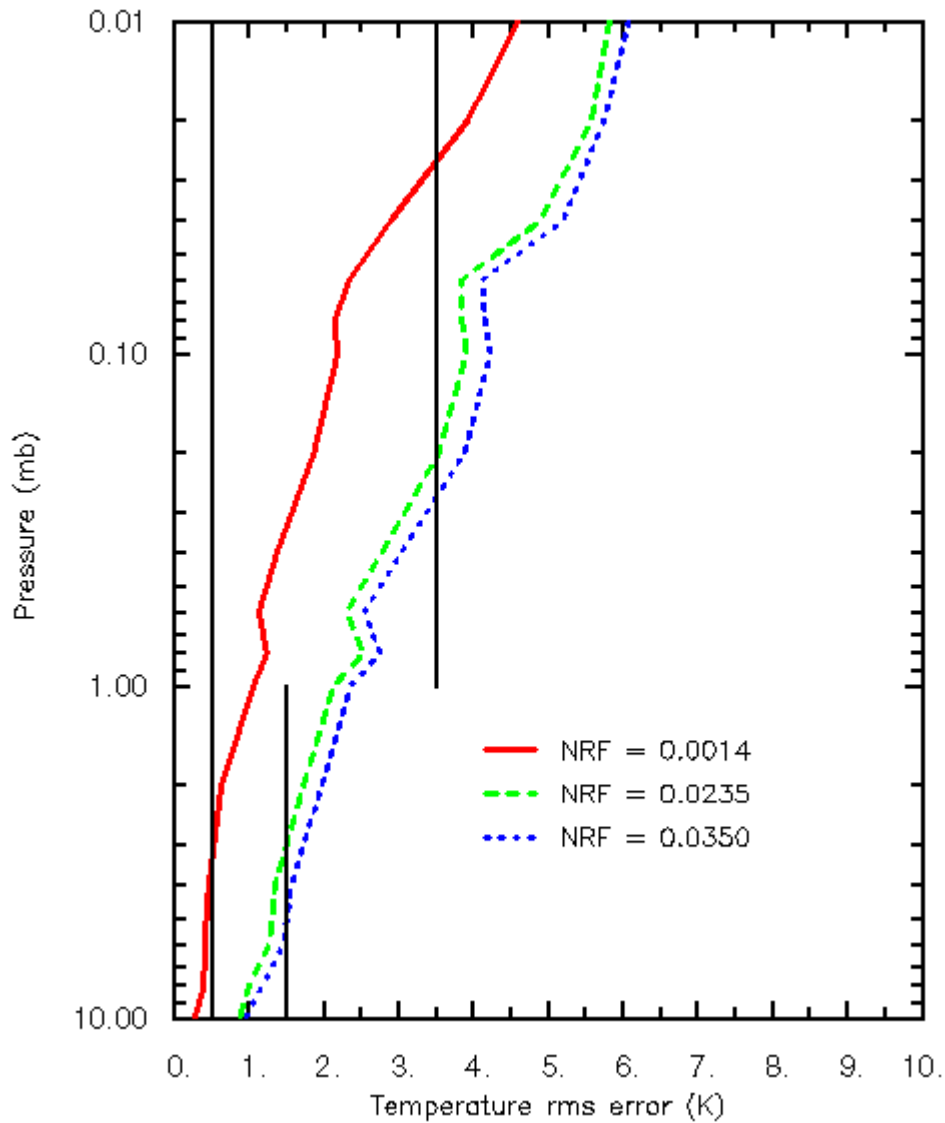


Figure 5-10. Upper atmosphere temperature profile rms error for three values of sensor noise. The NRF in the legend indicates the noise averaging factor, relative to single-footprint noise level. The solid curve corresponds to very low noise, and the dashed and dotted curves correspond to averaging over 300×300 and 200×200 km² CFOVs. The Rosenkranz dataset was used.

The test dataset is not large enough to compute performance statistics for data binned across the measurement range, but scatter plots of error versus true value (Figure 5-11) show no significant trend in error as a function of true value.

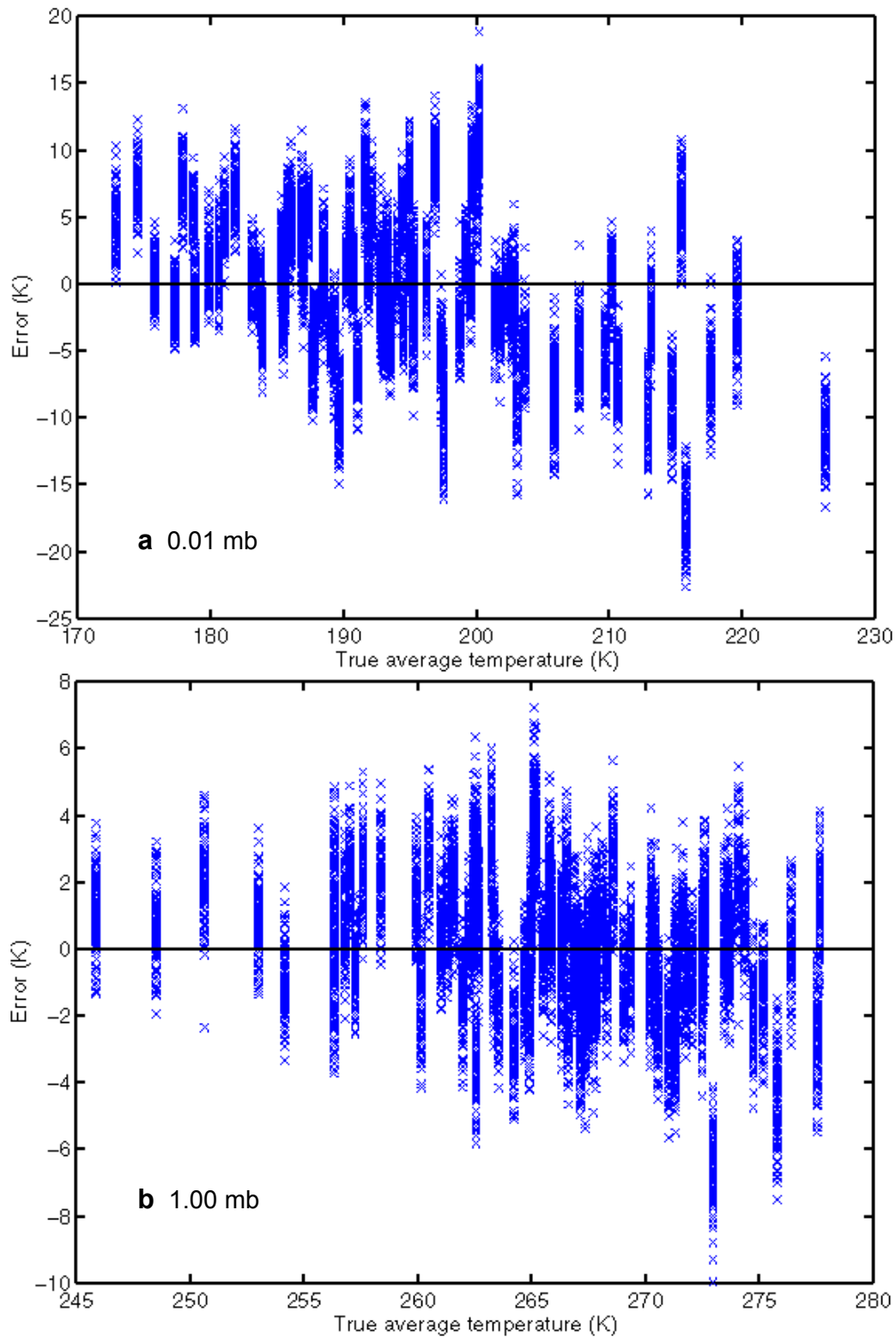


Figure 5-11. Temperature profile error for H polarization and a 300-km CFOV at a) 0.01 mb and b) 1 mb. The Rosenkranz dataset was used. For each test case (true temperature), errors are plotted for each of the 112 tabulated geomagnetic field conditions. Errors are for temperatures that have been vertically averaged per the SRD requirements.

Performance for the 12 CRISTA profiles is shown in Figure 5-12. For these retrievals, the *a priori* data were taken, as usual, from the Rosenkranz data. Considering the differences in the

datasets and their small sizes, the Rosenkranz profile statistics are not very good estimates of the ideal *a priori* statistics for application to the CRISTA data. As mentioned in Sec. 4.2.1, improving the *a priori* database is planned prior to launch and will be continued after launch. Despite the shortcomings of the *a priori* data, the algorithm produced comparable results for the two datasets, except above the 0.08-mb level. In the CRISTA performance, a major portion of the errors near 0.06 mb and near 0.2 mb was attributable to a single outlier profile.

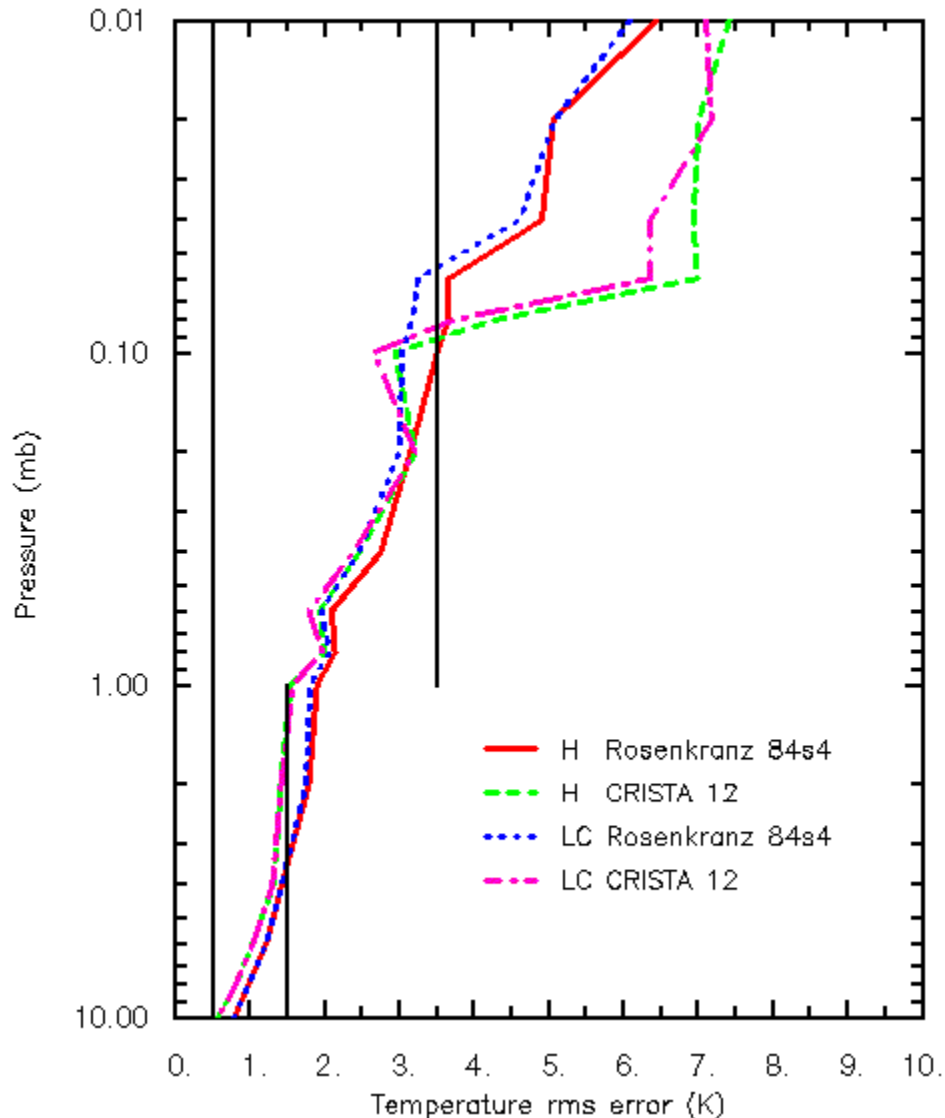


Figure 5-12. Upper atmosphere temperature profile rms error for the CRISTA dataset. Results from one quarter of the Rosenkranz data are shown for reference. Results are for a 300×300 km² CFOV. Performance is shown for horizontal polarization and for left circular.

Performance for the high-latitude rocketsonde dataset is in Figure 5-13. The background for these retrievals was derived from the high-latitude rocketsondes. The performance is similar to that obtained with the Rosenkranz dataset (see Figure 5-9). The results for altitudes above about the 0.1-mb level are not reliable because of the influence of the profile extrapolation.

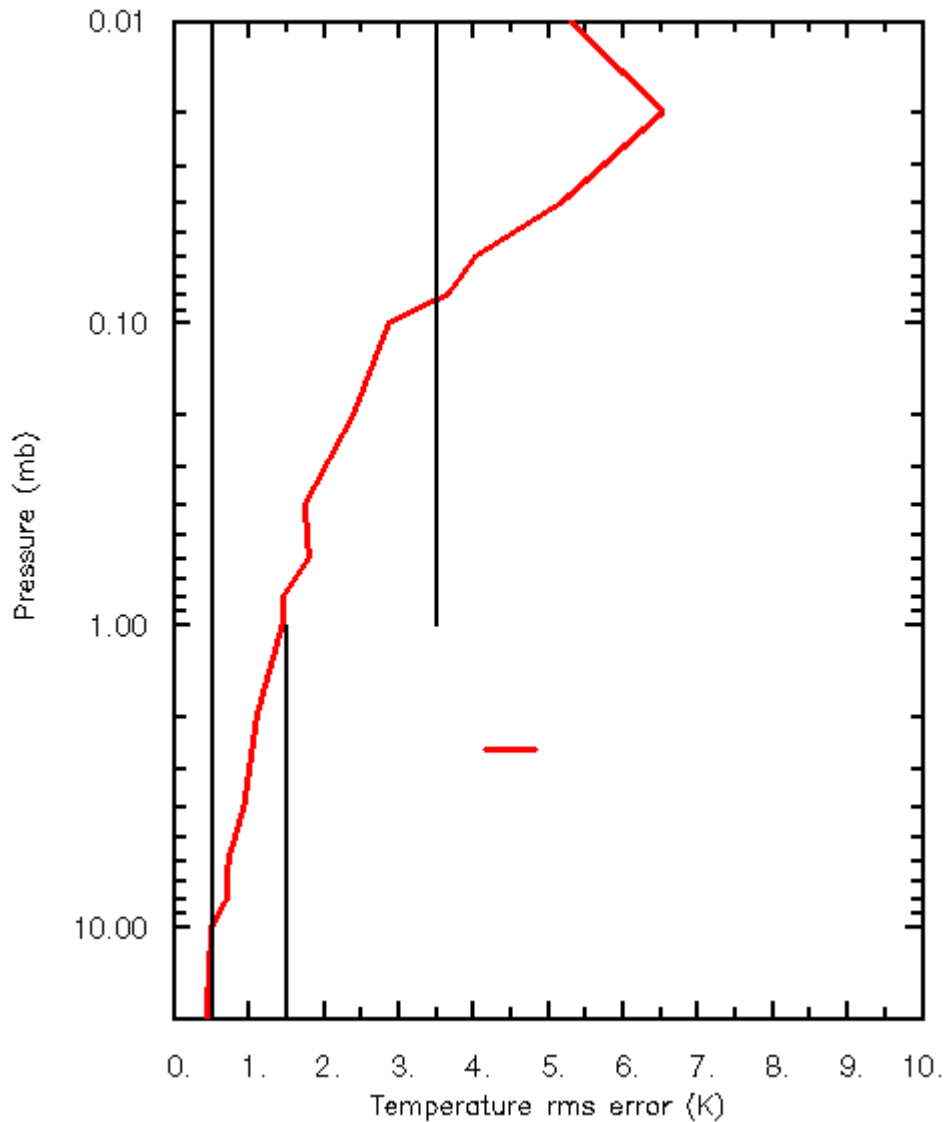


Figure 5-13. Upper atmosphere temperature profile rms error for the high-latitude rocketsonde dataset, using the current baseline system.

A potential area for future technology insertion is addition of a second set of digitally processed channels. The data thus provided would be largely redundant to the data provided by the original channel set, but the data would reduce the effective noise of the channel set as a whole. When the baseline set on the 7⁺ line is complemented by a set on the 9⁺ line (Figure 5-14), the performance is improved by about the equivalent of what can be achieved by expanding the CFOV by a factor 1.5.

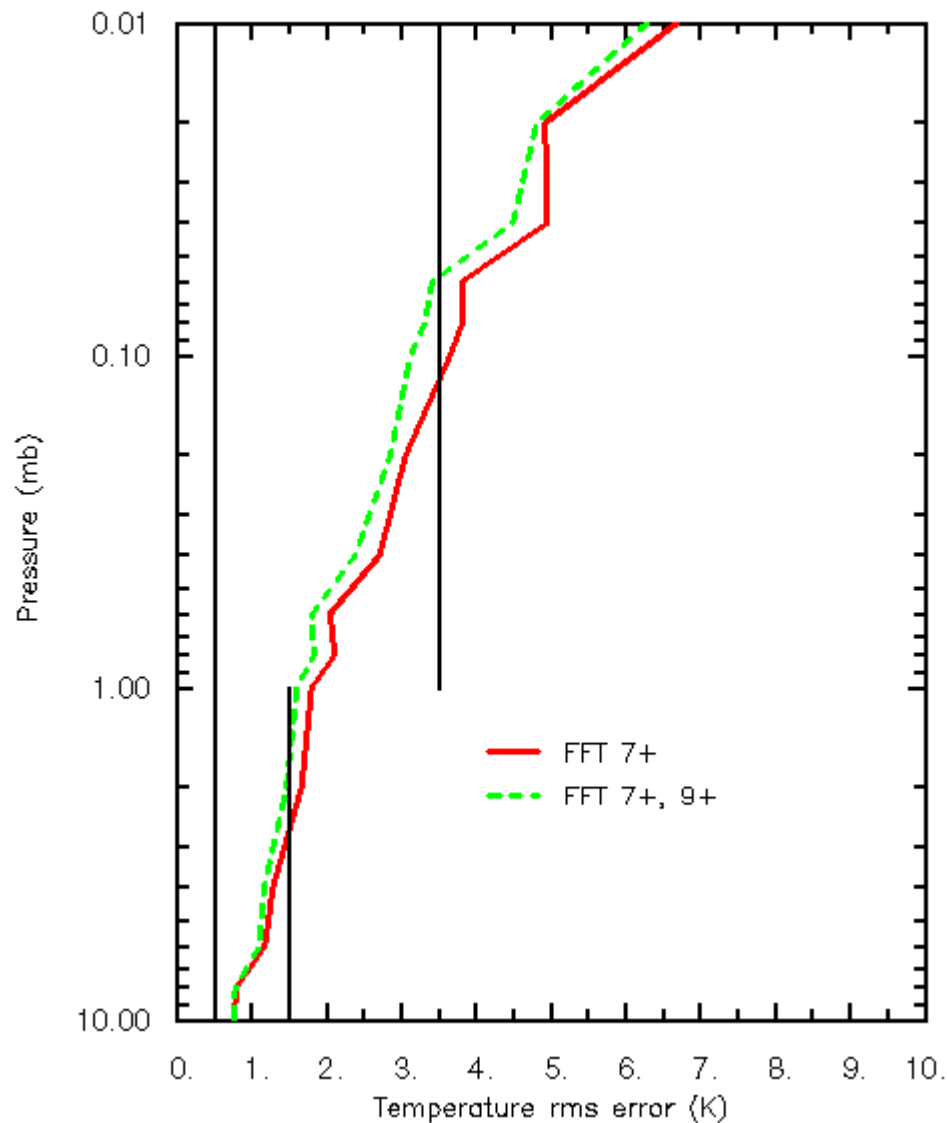


Figure 5-14. Upper atmosphere temperature profile rms error for channel sets with digital (FFT) channels on the 7⁺ line (solid curve) and on both the 7⁺ and 9⁺ lines (dashed curve). Horizontal polarization was used and the CFOV size is about 380×380 km². Statistics are for one quarter of the Rosenkranz dataset.

The change of baseline polarization from horizontal to left circular was based on performance tradeoffs (Figure 5-15) that showed circular polarization to be advantageous for CMIS at altitudes above the 1-mb pressure level.

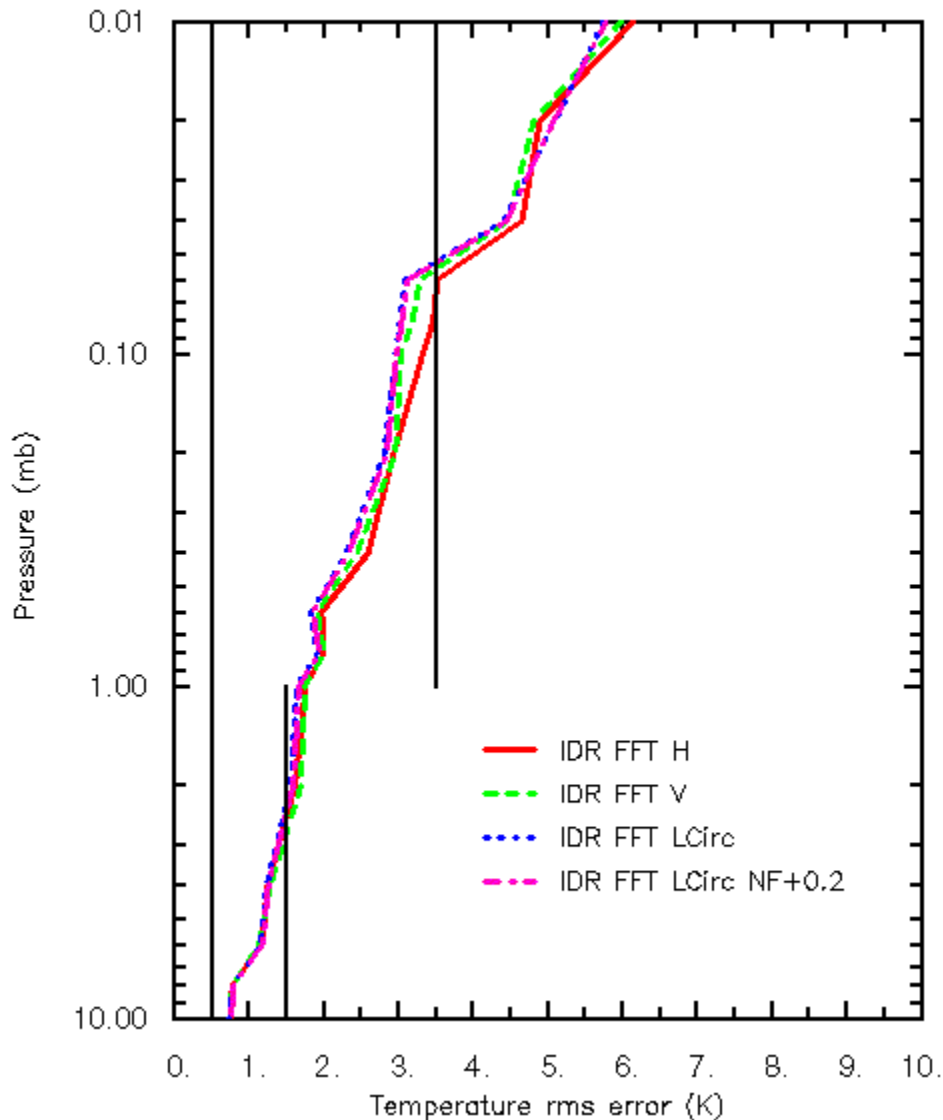


Figure 5-15. Upper atmosphere temperature profile rms error for H, V, and left circular channel polarizations. For left circular, the second curve was derived with the assumption that measuring in circular polarization adds 0.2 dB of loss to the sensor system, thus increasing the data noise. The noise is for a CFOV of about $380 \times 380 \text{ km}^2$, which is larger than the baseline size. One quarter of the Rosenkranz dataset was used.

The performance curves in Figure 5-15 are based on weighted averages over a range of geomagnetic conditions, as defined for method 2 in Sec. 5.3.1. While a particular polarization may be advantageous at a given pressure level for the ensemble of geomagnetic conditions, it is not advantageous in every condition. Some insight may be gained into the relationship between polarization and performance by considering individual conditions. Conditions to be scrutinized were identified by considering performance for a set of retrievals performed on one quarter of the Rosenkranz dataset. These retrievals were performed in each of the polarizations H, V, and left circular (LC) and, to simplify the analysis, center frequency errors were excluded. For each of the 112 geomagnetic conditions, error statistics were tabulated by taking the rms across the 21 test cases and averaging over the layers from 0.01 to 2 mb, where polarization differences were expected to have their greatest impact. The average rms performance for H polarization was compared with performance for V polarization and the geomagnetic conditions were ranked according to the performance difference between H and V. Similar comparisons were made

between H and LC and between V and LC. The rankings were then used to identify the most favorable condition for each polarization—the condition where the given polarization had its largest combined advantage over both of the other polarizations. The rankings did not include every possible condition, but just the 112 binned conditions that occurred with significant frequency for the CMIS scan geometry. The performance plots for each of the most favorable conditions (Figure 5-16) illustrates the results of the rankings. Even H polarization, which was least effective overall, was the best polarization in conditions such as in Figure 5-16a.

The advantage of a certain polarization in a certain geomagnetic condition can be related to the distribution of weighting functions under that condition. Weighting functions were computed for the mean of the Rosenkranz profiles for the 80 channels produced by digital processing (without the averaging that reduces the number to 40) and four analog channels. The weighting functions are shown in Figure 5-17, Figure 5-18, and Figure 5-19 for the geomagnetic conditions that were most favorable to H, V, and LC polarizations, respectively. Each curve in the plots for linear H and V polarizations represents two channels, because of the symmetry of the spectrum about the line center. When comparing the linear cases with the LC case, it must be kept in mind that two overlapping linear channels may provide nearly the same skill as two non-overlapping channels in LC, because each channel provides reduction in the effective noise of the channel set, while noise is a major factor in performance for these narrow channels.

Where H polarization was most favorable (Figure 5-17), the H polarization weighting functions were well distributed and provided channels peaking at higher altitudes than either V or LC polarization provided. These weighting function characteristics are expected in this condition, where the magnetic field is nearly perpendicular to the line of sight and nearly aligned with the horizontal orientation (as discussed in Sec. 3.4.5). In contrast, the highest-peaking V and LC weighting functions overlap each other heavily and are relatively broad. Where V polarization was most favorable (Figure 5-18), the weighting functions are higher peaking, more broadly distributed, and sharper for V polarization than for H polarization. The advantage of V polarization over LC polarization is more difficult to discern from the weighting function plots. These polarizations have about the same distribution of weighting functions at higher altitudes (recalling that each V curve represents two channels) and their performance there was about the same (Figure 5-16b). At pressures around 0.1 to 1 mb, the V-polarization weighting functions tend to be more sharply peaked and more tightly distributed (again, considering that the V curves are doubles) than the LC weighting functions. The magnetic field in this case is nearly perpendicular to the line of sight, which is favorable to linear polarization. Where LC polarization was most favorable (Figure 5-19), the LC weighting functions have a clear advantage with respect to sharpness, uniform distribution, and extent to the lowest pressures. The magnetic field in this case was more nearly perpendicular than parallel to the line of sight.

Based on the discussion in Sec. 3.4.5, one might expect that LC polarization would be most advantageous for a case where the magnetic field is parallel to the line of sight. The LC polarization was, in fact, advantageous for such a condition (Figure 5-16d), but less advantageous than the case in Figure 5-16c, by the metric used for vertical average performance. The weighting functions for LC polarization in this case (Figure 5-20) are well-behaved in this condition, while the H and V weighting functions have double peaks. The double peaks are detrimental, but not disastrous for retrieval performance. Some double-peaked weighting functions provide sensitivity (a peak) at high altitudes. The lower of the two peaks occurs at pressure levels where other channels have single peaks, enabling the algorithm to partially resolve the ambiguity of the signal.

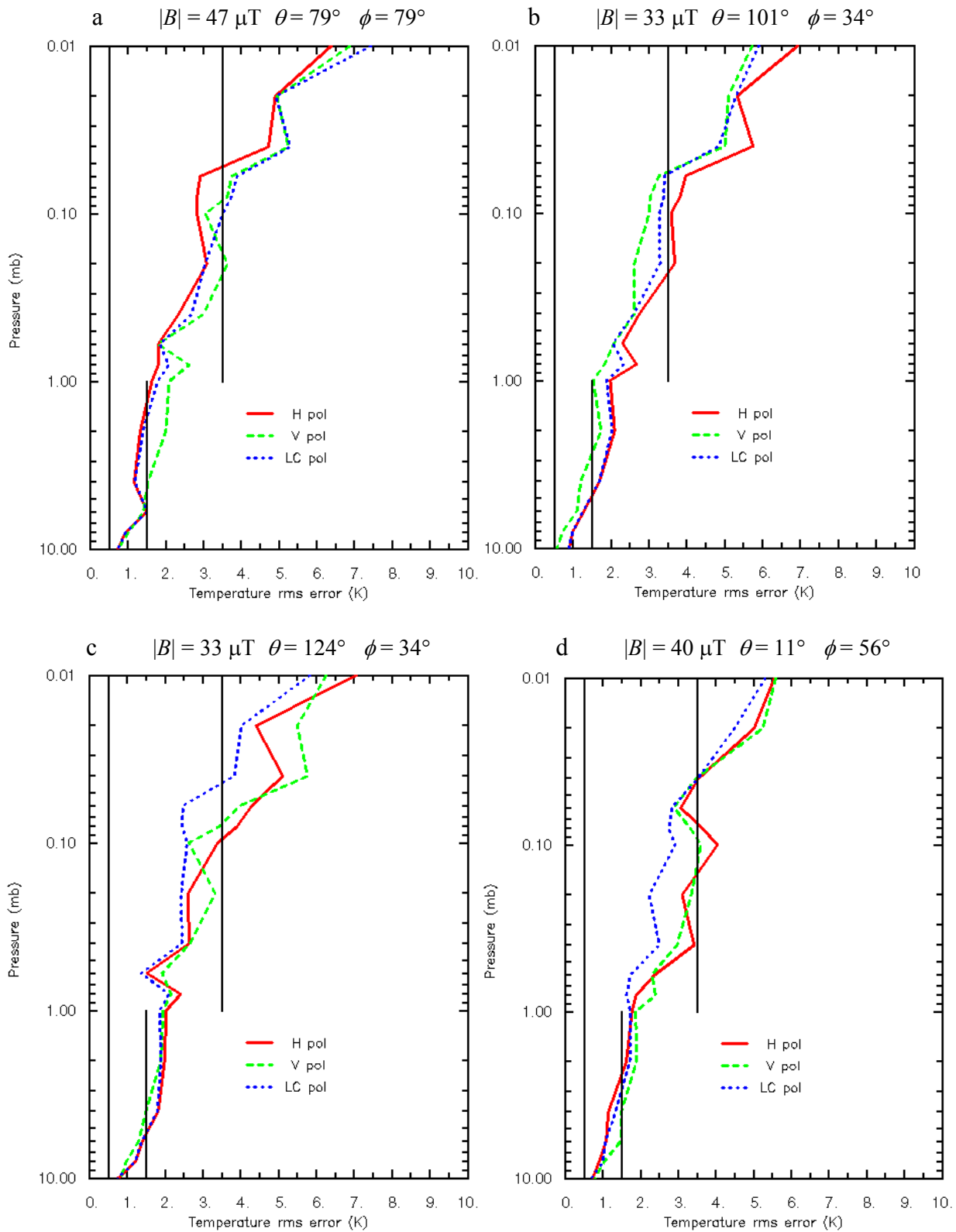


Figure 5-16. Retrieval performance for the most favorable geomagnetic conditions for a) H, b) V, and c) LC polarization; and d) for an additional condition discussed in the text. The noise is for a CFOV of $300 \times 300 \text{ km}^2$. One quarter of the Rosenkranz dataset was used.

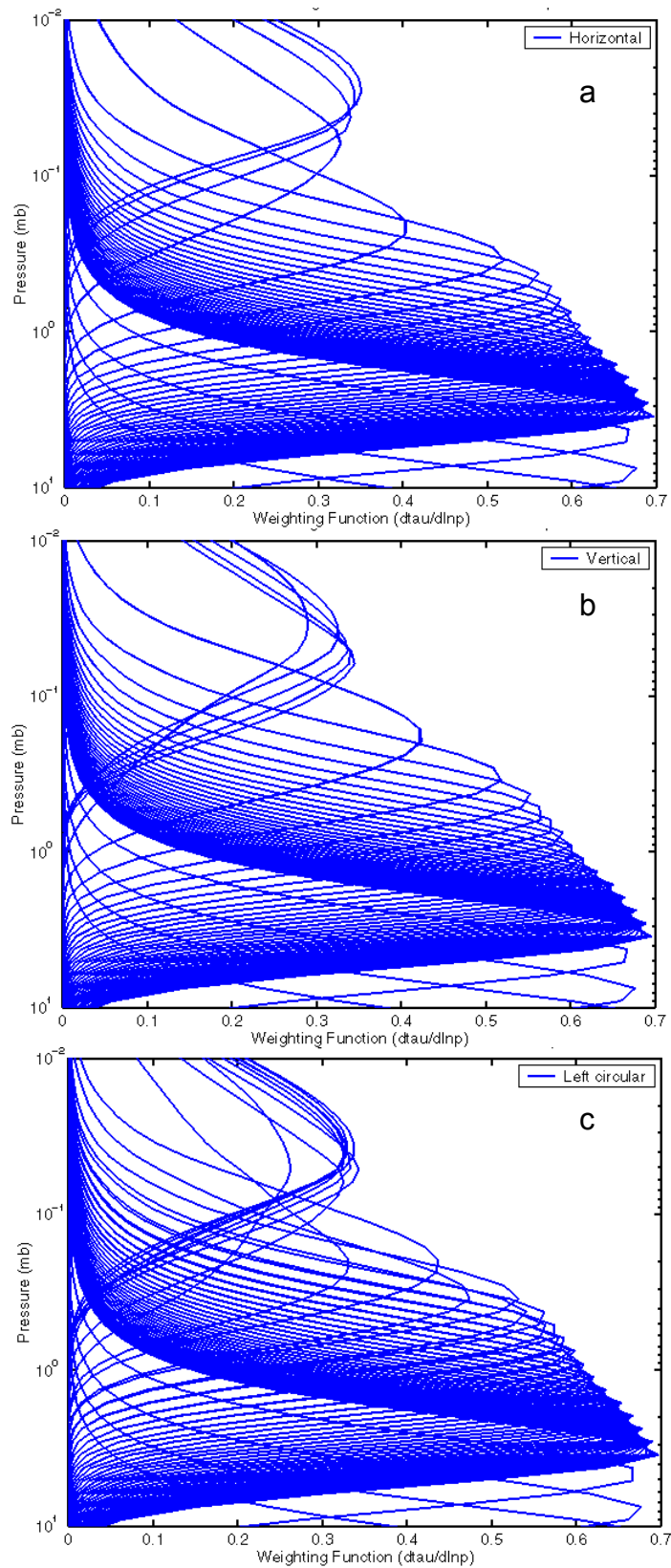


Figure 5-17. Weighting functions for the geomagnetic condition ($|B| = 47 \mu\text{T}$, $\theta = 79^\circ$, $\phi = 79^\circ$) most favorable for H polarization. Polarizations shown are a) H, b) V, and c) LC.

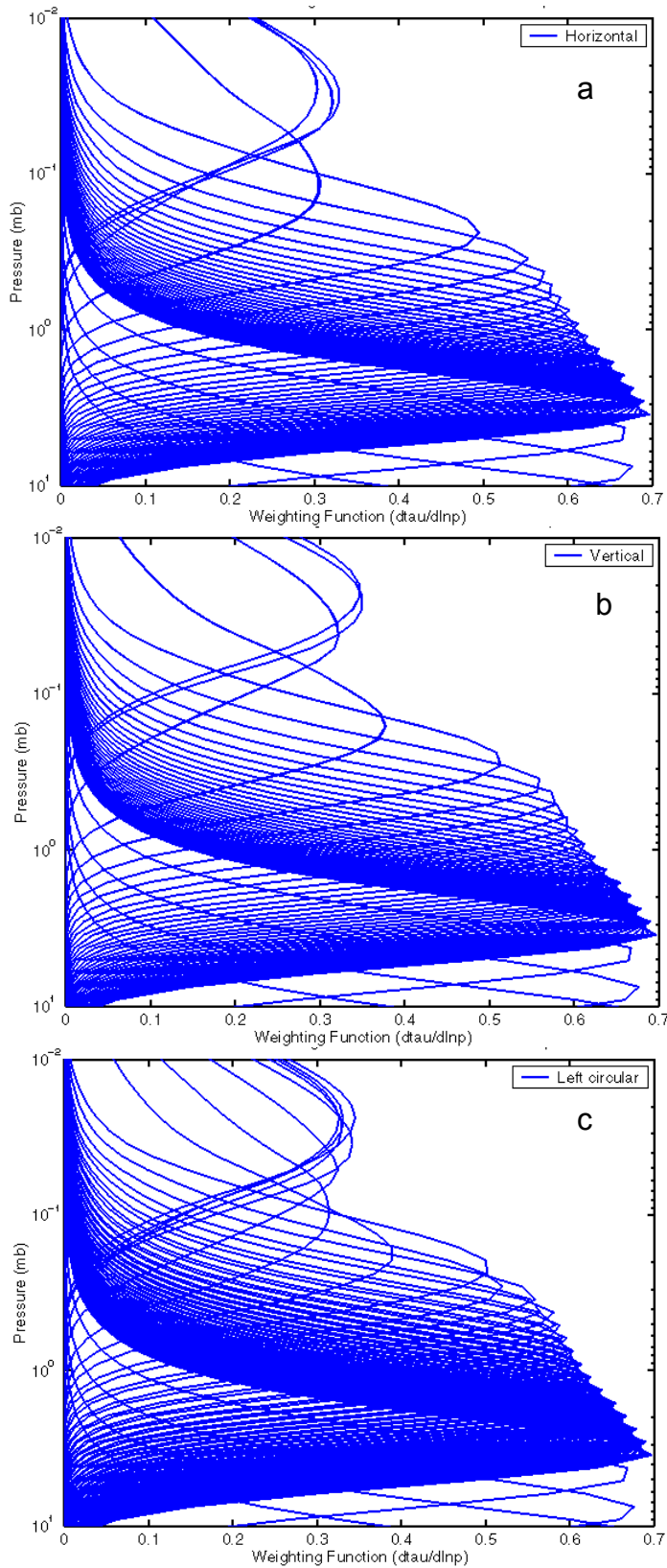


Figure 5-18. Weighting functions for the geomagnetic condition ($|B| = 33 \mu\text{T}$, $\theta = 101^\circ$, $\phi = 34^\circ$) most favorable for V polarization. Polarizations shown are a) H, b) V, and c) LC.

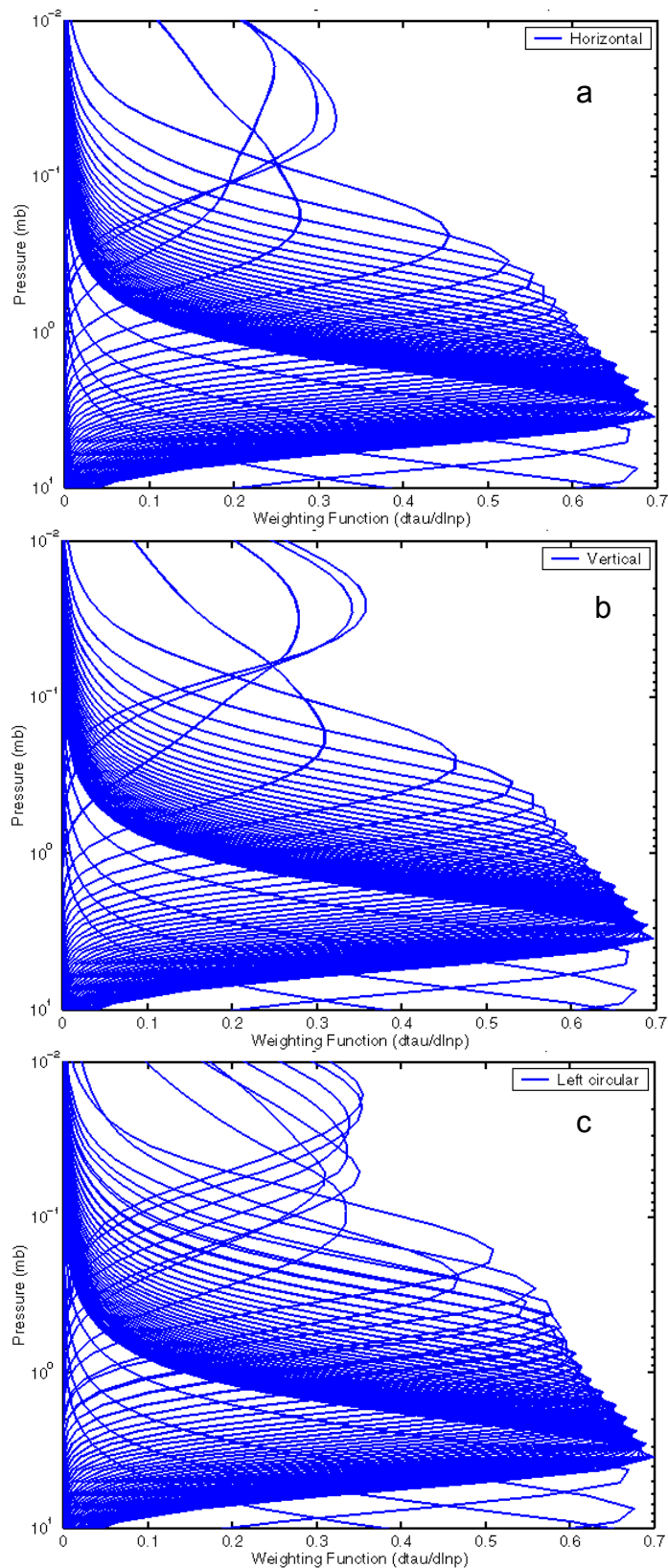


Figure 5-19. Weighting functions for the geomagnetic condition ($|B| = 33 \mu\text{T}$, $\theta = 124^\circ$, $\phi = 34^\circ$) most favorable for LC polarization. Polarizations shown are a) H, b) V, and c) LC.

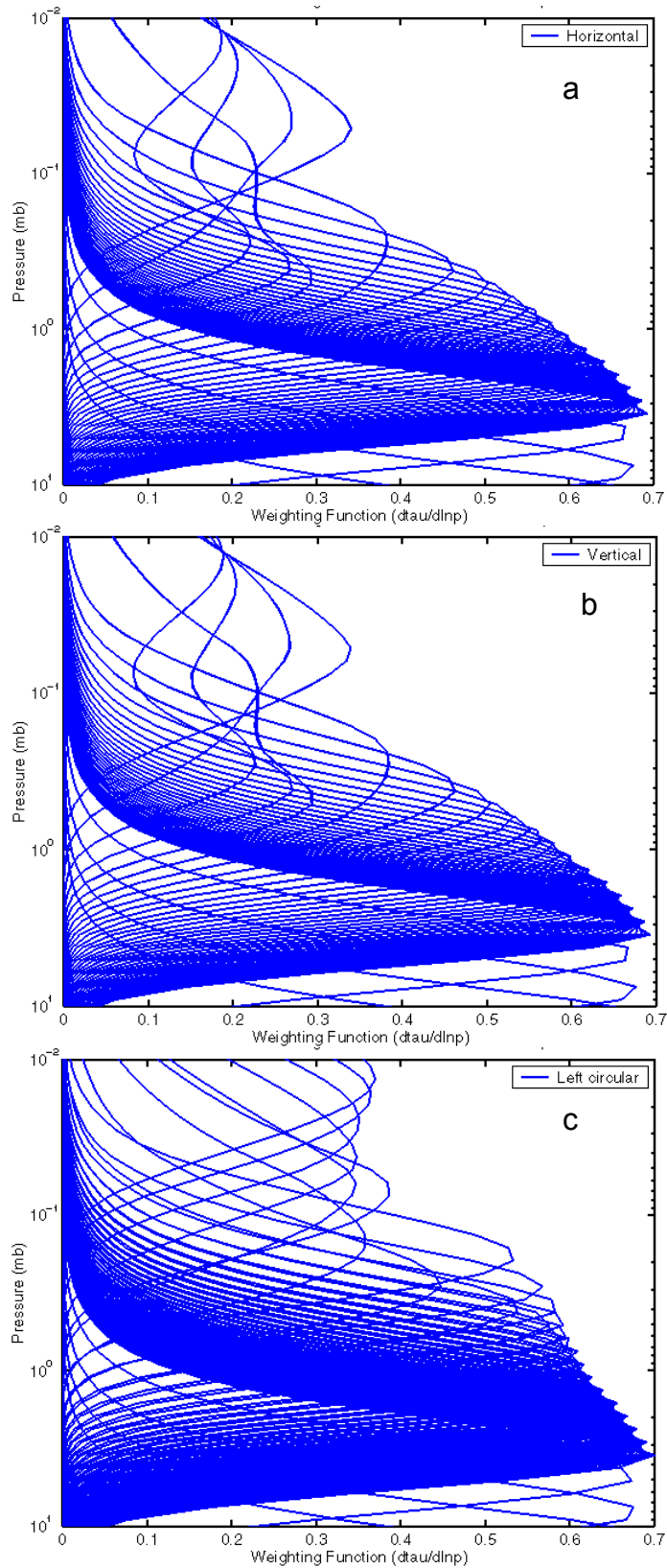


Figure 5-20. Weighting functions for an additional geomagnetic condition ($|B| = 40 \mu\text{T}$, $\theta = 11^\circ$, $\phi = 56^\circ$) favorable for LC polarization. Polarizations shown are a) H, b) V, and c) LC.

5.3.3. Polarization errors

Because of the polarization dependence of upper atmosphere radiative transfer, polarization alignment errors and polarization purity errors must be considered. Polarization alignment knowledge errors were applied to simulated sensor data by rotating the brightness temperature coherency matrix. Polarization purity knowledge errors were simulated by mixing brightness temperatures from the nominal polarization T_{BP} with those from the orthogonal polarization T_{BO} to obtain perturbed brightness temperatures $T'_{BP} = \alpha T_{BP} + (1 - \alpha) T_{BO}$. Polarization alignment errors are not relevant for the current (circular) polarization baseline. The impact of polarization purity errors is shown in Figure 5-21. With a requirement of 99% on polarization purity, this is an insignificant error source.

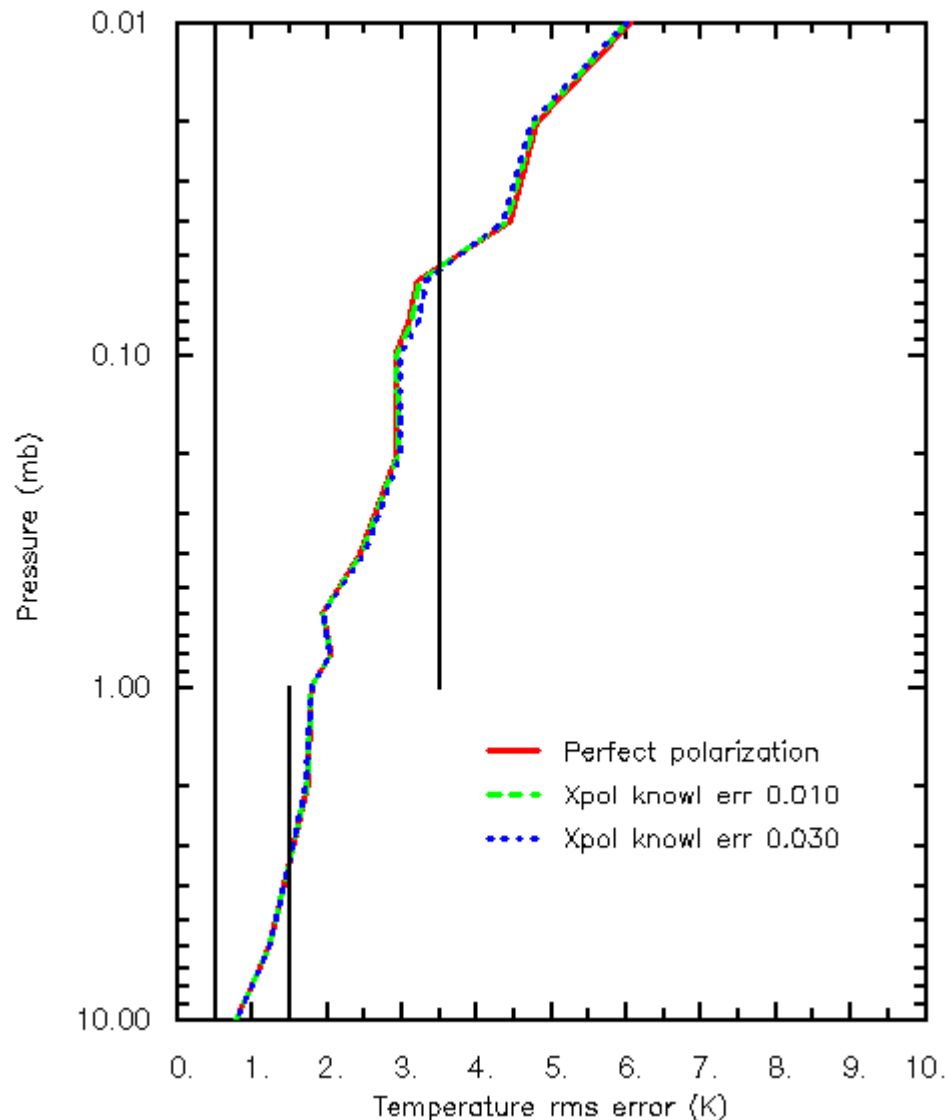


Figure 5-21. Upper atmosphere temperature profile rms error for varying polarization purity knowledge error. The labeled value of 0.01 represents $(1 - \alpha)$. The noise is for a CFOV of $300 \times 300 \text{ km}^2$. One quarter of the Rosenkranz dataset was used.

5.3.4. Sensitivity studies

5.3.4.1 Retrieval method in relation to regression

Stogryn (1989) has proposed a regression method for upper atmosphere temperature retrieval, where the major innovative aspect of the algorithm relates to the treatment of variable geomagnetic field conditions with respect to Zeeman line splitting. The nonlinearity of the Zeeman effect prevents it from being treated simply by training the regression with a range of geomagnetic conditions. Stogryn's solution was to compute regression coefficients (relating temperature profiles to brightness temperatures) for each of a selected set of geomagnetic field conditions. A formulation was devised to (nonlinearly) interpolate the coefficients from the training sets to the geomagnetic condition at any given observation site. This method produces performance virtually as good as if regressions were trained specifically for each possible geomagnetic condition.

The physical algorithm was compared with regression. For the comparisons, the regression was trained on a specific geomagnetic condition ($|B|=50\mu\text{T}$, $\theta=135^\circ$, $\phi=45^\circ$) and it was tested only on that condition, simulating the ideal treatment of the Zeeman effect within the context of regression. The physical algorithm was tested under the same condition. The same profiles were used to train the regression and to derive the *a priori* statistics for the physical method. As was the general case, one quarter of the Rosenkranz dataset were reserved for performance testing and the other three-quarters were the training data. For the regression training, 20 replications of each profile were used with different measurement noise realizations.

The two algorithms generated nearly the same performance when tested on the Rosenkranz dataset (Figure 5-22). To further investigate the algorithm behavior, each algorithm was applied to a new set of test profiles, without performing new training. These profiles were the U. S. Standard Atmosphere and five climate-zone average profiles (McClatchey, 1971). The intention was to test the algorithms on profiles from a different population than the one from which the training data had been derived. Twenty replications of each of the six profiles (with different noise realizations) constituted this test set. For this test set, the physical algorithm performed significantly better than the regression (Figure 5-23), illustrating that the physical algorithm is less reliant than regression on having well-matched training data. This is an important attribute of the physical algorithm because of the scarcity of appropriate training data.

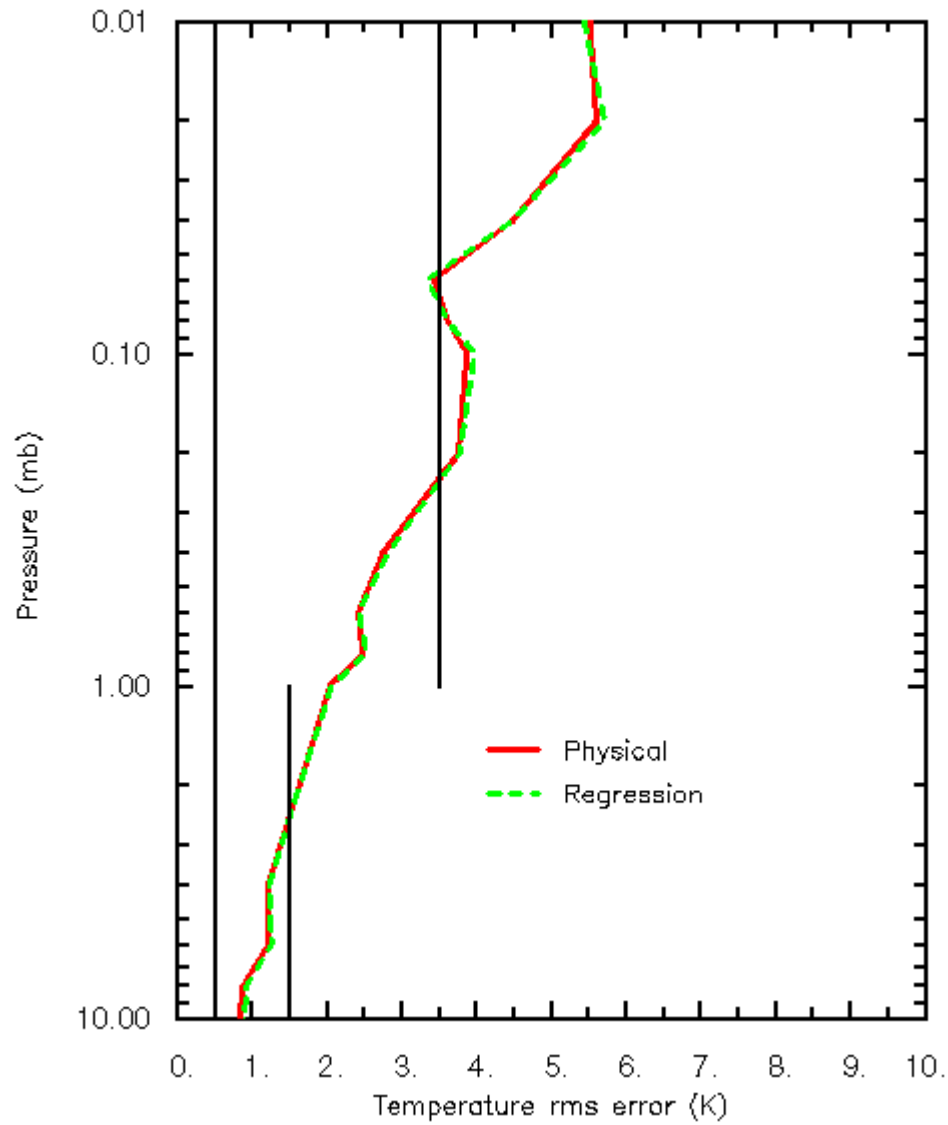


Figure 5-22. Comparison of temperature profile rms errors for the physical algorithm and regression, as applied to the Rosenkranz dataset. The polarization is horizontal and noise is for a CFOV of $300 \times 300 \text{ km}^2$.

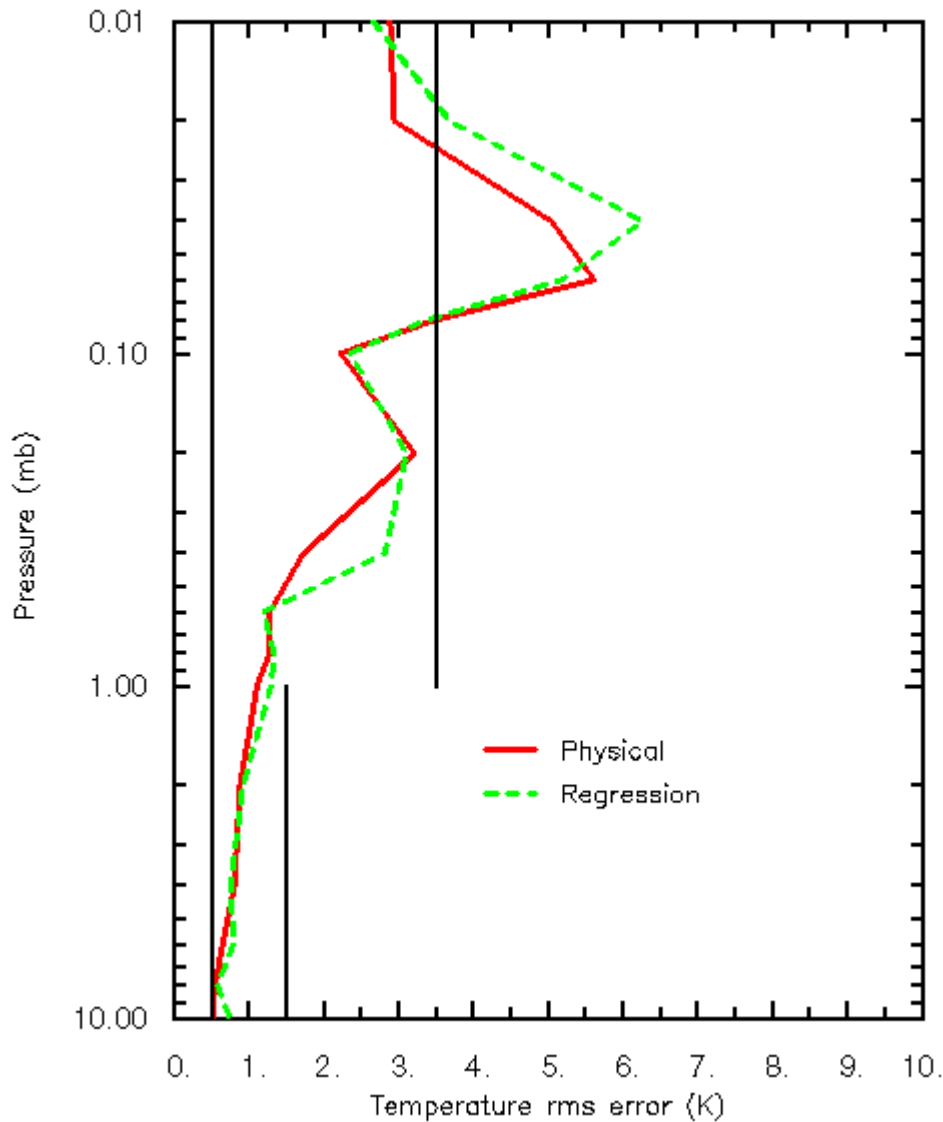


Figure 5-23. Comparison of temperature profile rms errors for the physical algorithm and regression, as applied to standard atmosphere profiles. The noise is for a CFOV of 300×300 km².

5.3.4.2 Iteration requirements

The physical algorithm performance was evaluated with respect to the number of iterations used. The bulk of the improvement from the *a priori* (0 iterations) profile occurred on the first iteration, and convergence was essentially complete after two iterations (Figure 5-24).

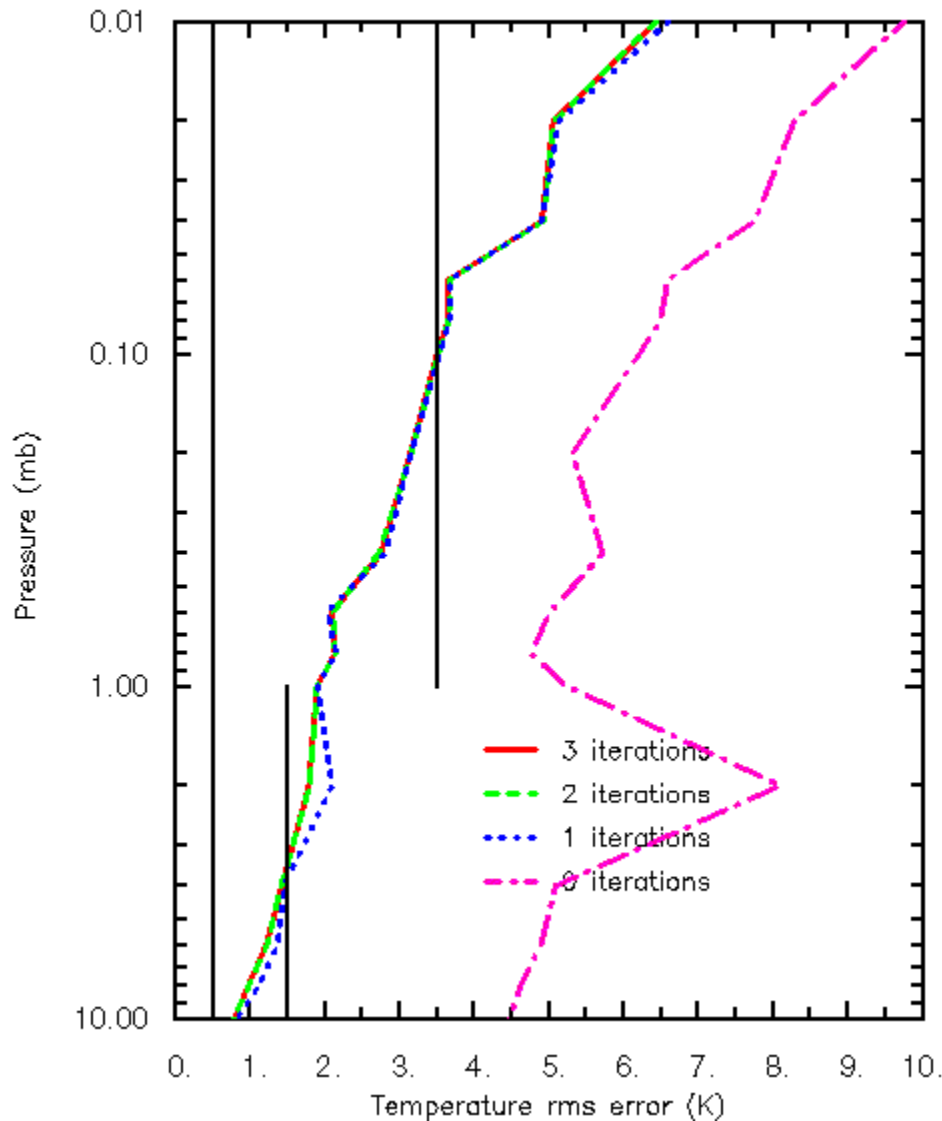


Figure 5-24. Upper atmosphere temperature profile rms error, as a function of the number of iterations of the physical algorithm. The polarization is horizontal and noise is for a CFOV of $300 \times 300 \text{ km}^2$. One quarter of the Rosenkranz dataset was used.

Considering the relatively high computational requirements of the physical algorithm, we performed test retrievals where the regression algorithm provided the initial guess profile (but not the *a priori* constraint) for the physical algorithm. These tests were performed under the same conditions as the other tests discussed in Sec. 5.3.4.1, considering performance on the Rosenkranz profiles and the standard atmosphere profiles. The performance for regression followed by one iteration of the physical algorithm was nearly identical to the performance for three iterations of the physical algorithm without the regression input. This result supports the viability of the option of using a regression first guess as a means to reduce the number of physical iterations and thus conserve computer resources.

5.3.4.3 Stratification

The variability of weighting functions in response to changes in geomagnetic field conditions suggests that retrieval performance should likewise vary. This topic was investigated by computing performance separately for each of the 112 geomagnetic field conditions that

occurred most frequently in the global distribution (Sec. 5.3.1). At each level, there are substantial performance variations (Figure 5-25), but no geomagnetic condition has performance that is systematically better or worse than all the others over the full profile.

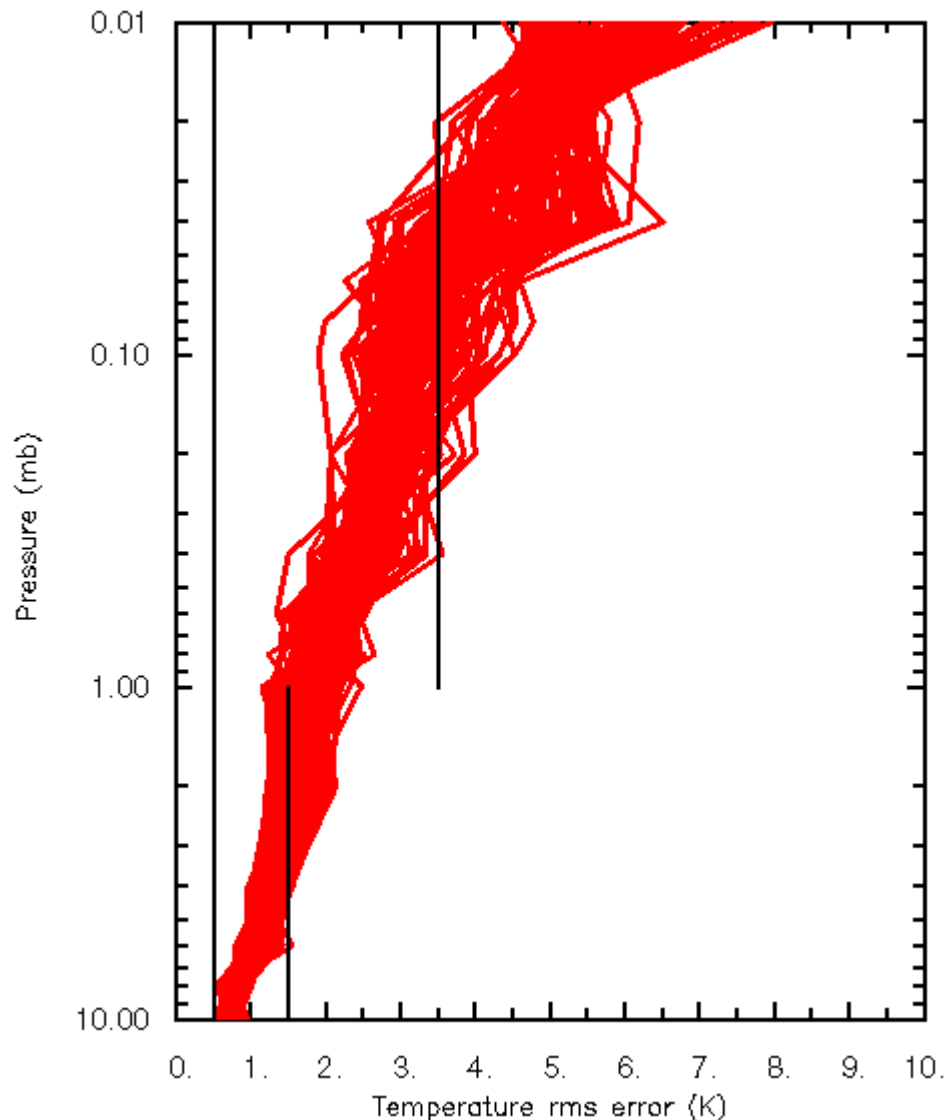


Figure 5-25. Stratified upper atmosphere temperature profile rms error. Each curve represents error under one geomagnetic field condition. The polarization is horizontal and noise is for a CFOV of about $380 \times 380 \text{ km}^2$. One quarter of the Rosenkranz dataset was used.

5.3.4.4 Response to channel failure

In the event that a CMIS channel fails to operate, the physical algorithm can accommodate the channel loss simply by switching the channel off in the retrieval. No retraining is needed, unlike for statistical algorithms. The performance has been demonstrated to degrade gracefully in relation to the particular channel or channels that are lost. In two instances where data from a single FFT channel is lost, there is a very small localized increase in retrieval error (Figure 5-26). For the case where the entire suite of FFT-derived channels are lost, performance degrades to a minor degree from about 8 to 4 mb and then more steeply for lower pressures (Figure 5-26).

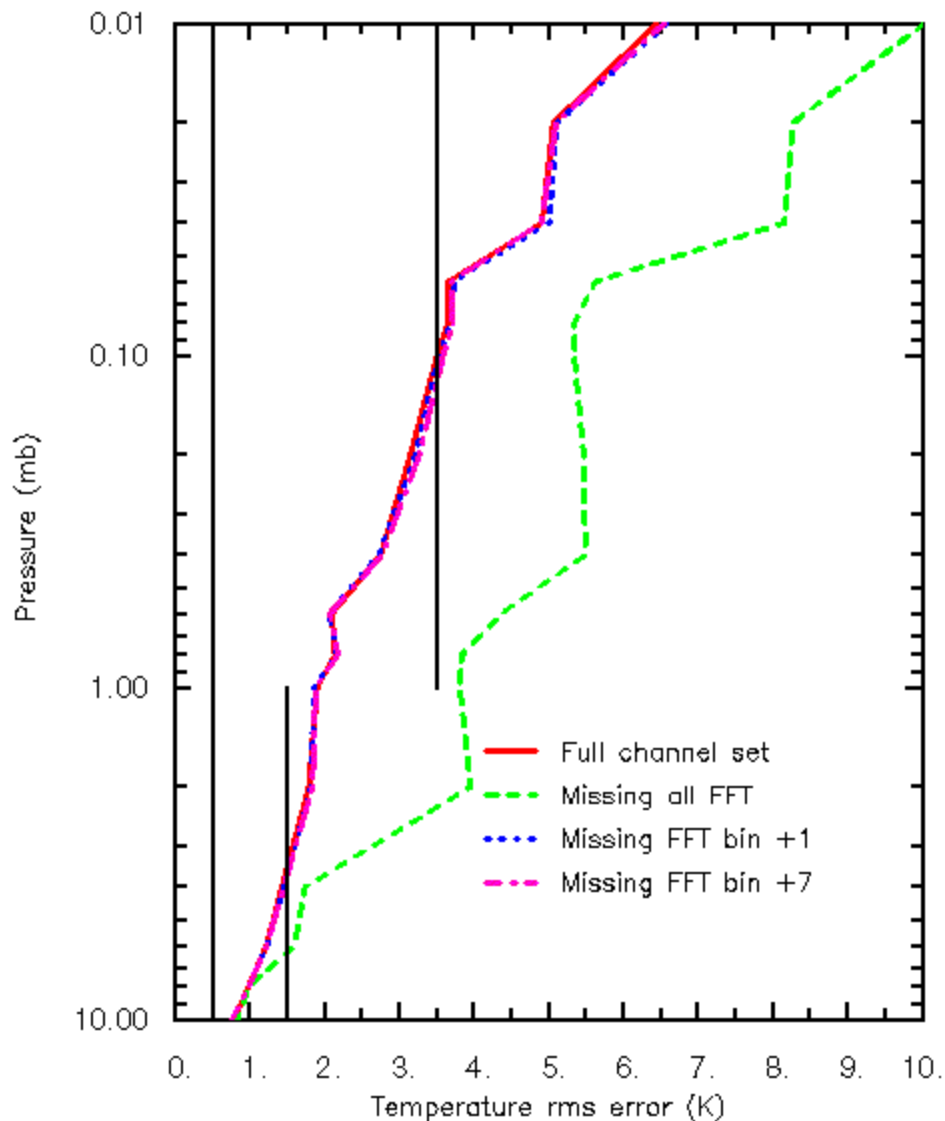


Figure 5-26. Sensitivity of upper atmosphere temperature profile rms error to loss of all the FFT-processed channels and loss of two individual channels (FFT bins). The polarization is horizontal and noise is for a CFOV of $300 \times 300 \text{ km}^2$. One quarter of the Rosenkranz dataset was used.

5.3.4.5 Doppler shifting and data averaging

Performance tests were conducted to evaluate the influence of Doppler shifting. The initial tests used data from each of the 80 individual bins independently, with no bin averaging. Doppler shifting had a negligible impact on performance. We then tested the impact of changing from using the 80 individual bins to using data that had been averaged to 40 bins, as is done in the baseline design. Again, the impact on performance was negligible, confirming that the method used to optimize the averaging was effective.

5.4. Performance summary

The nominal performance for the AVTP EDR is listed in Table 5-1. The key performance metric is the measurement uncertainty. The other performance metrics essentially define the

measurement domain and the validation conditions under which the key metrics must be met. The error budget discussed below therefore focuses on the key metrics. Each measurement uncertainty value applies to a range of vertical reporting (pressure) levels. The quoted performance refers to the worst-case pressure level within the range (the performance would appear better if all data within the range were pooled before computing statistics).

Table 5-1: Nominal performance for the AVTP EDR

Para. No.		Thresholds	Performance
C40.2.2-1	a. Horizontal Cell Size		
	1. Surface to 20 mb	40 km	40 km
	2. 20 mb to 0.01 mb	200 km	200 km
C40.2.2-2	Deleted		
C40.2.2-3	Deleted		
C40.2.2-4	Deleted		
C40.2.2-5	b. Horizontal Reporting Interval		
	1. Surface to 20 mb	40 km	40 km
	2. 20 mb to 0.01 mb	200 km	200 km
	c. Vertical Cell Size		
	Clear		
C40.2.2-6	1. Surface to 300 mb	1 km	1 km
C40.2.2-7	2. 300 mb to 30 mb	3 km	3 km
C40.2.2-8	3. 30 mb to 1 mb	5 km	5 km
C40.2.2-9	4. 1 mb to 0.01 mb	5 km	5 km
	Cloudy		
C40.2.2-10	5. Surface to 700 mb	1 km	1 km
C40.2.2-11	6. 700 mb to 300mb	1 km	1 km
C40.2.2-12	7. 300 mb to 30 mb	3 km	3 km
C40.2.2-13	8. 30 mb to 1 mb	5 km	5 km
C40.2.2-14	9. 1 mb to 0.01 mb	5 km	5 km
	d. Vertical Reporting Interval		
C40.2.2-15	1. Surface to 850 mb	20 mb	20 mb
C40.2.2-16	2. 850 mb to 300 mb	50 mb	50 mb
C40.2.2-17	3. 300 mb to 100 mb	25 mb	25 mb
C40.2.2-18	4. 100 mb to 10 mb	20 mb	20 mb
C40.2.2-19	5. 10 mb to 1 mb	2 mb	2 mb
C40.2.2-20	6. 1 mb to 0.1 mb	0.2 mb	0.2 mb
C40.2.2-21	7. 0.1 mb to 0.01 mb	0.02 mb	0.02 mb
C40.2.2-22	e. Horizontal Coverage	Global	Global
C40.2.2-23	f. Vertical Coverage	Surface to 0.01 mb	Surface to 0.01 mb
C40.2.2-24	g. Measurement Range	180-335K	162-335K
C40.2.2-25	Not used		
	h. Measurement Uncertainty		
	Clear		
C40.2.2-26	1. Surface to 700 mb	1.6 K / 1 km layers	1.6 K / 1 km layers
C40.2.2-37	2. 700 mb to 300 mb	1.5 K / 1 km layers	1.4 K / 1 km layers
C40.2.2-27	3. 300 mb to 30 mb	1.5 K / 3 km layers	1.3 K / 3 km layers
C40.2.2-28	4a. 30 mb to 6 mb	1.5 K / 5 km layers	1.5 K / 5 km layers
C40.2.2-28	4b. 6 mb to 1 mb	1.5 K / 5 km layers	2.4 K / 5 km layers
C40.2.2-29	5a. 1 mb to 0.3 mb	3.5 K / 5 km layers	3.5 K / 5 km layers
C40.2.2-29	5b. 0.3 mb to 0.01 mb	3.5 K / 5 km layers	6.5 K / 5 km layers
	Cloudy		
C40.2.2-30	5. Surface to 700 mb	2.5 K / 1 km layers (TBR)	2.0 K / 1 km layers

Para. No.		Thresholds	Performance
C40.2.2-31	6. 700 mb to 300 mb	1.5 K / 1 km layers (TBR)	1.4 K / 1 km layers
C40.2.2-32	7. 300 mb to 30 mb	1.5 K / 3 km layers (TBR)	1.3 K / 3 km layers
C40.2.2-33	8a. 30 mb to 6 mb	1.5 K / 5 km layer (TBR)	1.5 K / 5 km layers
C40.2.2-33	8b. 6 mb to 1 mb	1.5 K / 5 km layer (TBR)	2.4 K / 5 km layers
C40.2.2-34	9a. 1 mb to 0.3 mb	3.5 K / 5 km layers (TBR)	3.5 K / 5 km layers
C40.2.2-34	9b. 0.3 mb to 0.01 mb	3.5 K / 5 km layers (TBR)	6.5 K / 5 km layers
C40.2.2-35	i. Mapping Uncertainty	5 km	3 km
C40.2.2-36	j. Swath Width	1700 km (TBR)	1700 km

A large component of the retrieval error is the smoothing error associated with the vertical resolution of the sounder and the ambiguity introduced by variations in water vapor, cloud, and surface properties. This error source is sometimes called the null-space error (Rodgers, 1990) because it represents the portions of the temperature profile space that cannot be measured by the sounder. The impact of smoothing error is illustrated for the upper atmosphere by the retrieval error with minimal sensor noise in Figure 5-10. The next most significant error source is radiometric noise, whose influence can be seen by the difference between the curves in Figure 5-10. The error due to data noise predominates at the lower altitudes and the smoothing error predominates at higher altitudes.

There may be sensor errors with regard to the knowledge of the spectral gain function. Such errors are commonly parameterized as a shift in the center frequency of the passband. The impact of a 20-kHz shift of center frequency is shown in (Figure 5-27). A 20-kHz center frequency knowledge error is allocated at the EDR algorithm level. This represents the residual knowledge error after correction in post-launch processing, which is discussed further in Section 5.6. Note that this error source is negligible for linear polarization but is significant for circular polarization, so it was included by default in retrieval simulations.

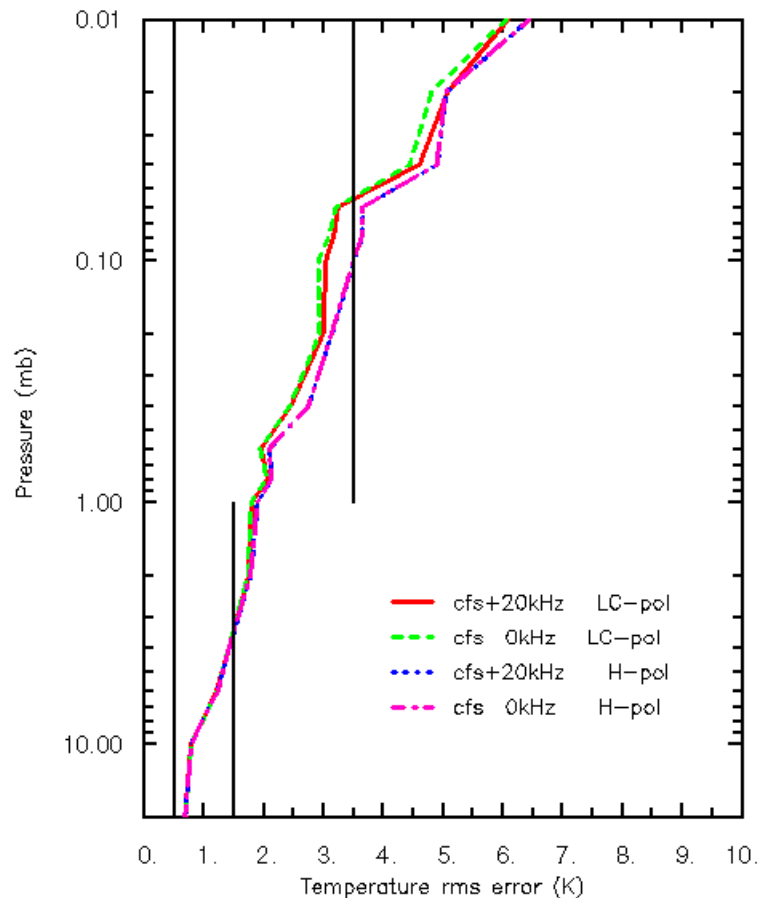


Figure 5-27: Impact of center frequency instability error on upper atmosphere temperature profile retrieval error. Results are shown for left circular (LC) and horizontal polarization (H). The red solid and blue dotted curves are for simulated retrievals with center frequencies shifted 20 kHz from the “true” values. Noise is for a CFOV of 300×300 km².

The error budget for the AVTP measurement uncertainty is in Table 5-2. Where an error budget entry is zero, that indicates that the error term is negligible in relation to the other terms, not that the error term is identically zero.

The row in the table denoted “Default retrieval error” refers to the error sources incorporated into the default retrieval simulations, including smoothing (null-space) and radiometric noise. For the upper atmosphere, we took the conservative approach of relying on the worst-case results among the test datasets. For the lower atmosphere, the values in that row were derived by combining results for ocean, “warm” land, and “cold” land (Table 5-3), while excluding land surfaces for the lowest layer, where threshold requirements cannot be met (see following section). The distinction between warm and cold land was a surface temperature cutoff of 0°C and a surface emissivity spectrum characteristic of unfrozen land or snow, respectively. Following that row are several rows (up to “Subtotal”) for which the errors are additive. The numbers cited are the added retrieval errors that were found as each error source was individually simulated.

For the lower atmosphere retrievals, performance is affected by the cascade execution method for the core module (ATBD Vol. 1 and 2). The cascade improves performance in regions where the scene is horizontal homogeneous, such that the temperature profile retrieval report at 40-km cell size is of similar quality to a report generated from 50-km data. The net effect of the cascade depends on the global distribution of fine-scale spatial structure of cloud, water vapor and other

environmental variables, which is not known with certainty and is difficult to estimate with currently existing datasets. The analyses on which the error budget is based were performed with direct 40-km core module retrievals because, at the time of their execution, the simulation environment was not mature enough to make it economical to perform retrievals with the cascade. For error budgeting, we make the highly conservative assumption that the cascade AVTP performance at 40-km is equal to the performance for direct 40-km retrievals.

Air mass classification was not implemented in the default retrieval simulations, so it is handled as a separate correction for the purposes of error budgeting, primarily affecting the 100-to-300-mb layer.

The error budget includes two terms for spectroscopic errors. One refers to the biases between the brightness temperatures CMIS reports and brightness temperatures simulated by applying the core module radiative transfer to data representing the true environmental conditions. It is a residual in the sense that these biases are largely corrected before the water vapor retrievals are performed, using correction factors derived from calibration/validation with ground truth data (Wentz, 1997). Some differences between the CMIS measurements and the model are not sufficiently systematic to be corrected with ground truth data, and the budget includes a separate term for these errors.

Sub-field-of-view effects include partial cloud cover within the field of view. The effect of partial cloud cover was evaluated by considering the most inhomogeneous case, 50% cloud cover, over the surface where the radiometric data are most sensitive to cloud effects, oceans. In this case, the retrieval error was increased about 0.1 K. The effect was negligible over land. We estimate the net effect for global cloudy conditions to be 0.02 K. The effect is not present for clear conditions.

Additional sub-field-of-view effects include differences in cloud between the direct and indirect paths by which radiation reaches the satellite. The direct path follows the satellite view vector from the surface to the satellite. The indirect path refers to downwelling radiation that is reflected by the surface before being transmitted to the satellite. To address differences between cloud in direct and indirect paths, we made simulations where cloud was placed in only the direct path and looked at the impact on retrieval performance. The effect of the differences between the paths was negligible with respect to temperature profile error. The evaluations focused on cloud inhomogeneities, as opposed to other effects, because cloud varies on particularly short scales.

Spatial coregistration errors involve two factors. One is the divergence of two beams that are coregistered at the surface but have different Earth incidence (zenith) angles and, hence, slightly different paths through the atmosphere. An analysis of this factor found no significant effect on temperature profile retrieval. The other factor is the uncertainty in the position of each channel's beam in relation to the positions of other channels. This factor was evaluated by considering several types of scene spatial structure that could cause brightness temperatures in a misregistered channel to be different from a correctly registered channel. Effects of cloud, surface emissivity, and surface temperature were considered and the impact on retrieval performance was computed. Details of the analyses are in Appendix A of ATBD Vol. 1, Part 1: Integration. For the AVTP EDR, coregistration errors within the requirements flowed to the sensor could cause retrieval error to increase by 0.02 K from the surface to 300 mb.

The channels on CMIS are not all boresighted, so there are time offsets on the order of a few seconds between the views of the various channels. An analysis indicated that the time offsets have no significant impact on retrievals.

Surface pressure is required as input to the core module within 2.5 mb uncertainty. At that level, and even for uncertainties up to 10 mb, there is negligible effect of surface pressure error on the temperature profile retrievals.

The process of vertical registration can introduce error in the vertical temperature profiles through the horizontal interpolations that are involved. We designed the algorithm to minimize those errors. Temperature retrievals for the 40-km CFOVs are performed at a CFOV spacing of 20 km and 12.5 km in the along-scan and cross-scan directions, respectively. Nyquist sampling is effectively provided and the interpolation error is statistically negligible.

Errors are introduced by the difference in spatial weighting between the horizontal cells used for validation (uniform averaging over a square) and the composite antenna pattern represented by the CFOV. Analysis of this effect is discussed in Appendix D of ATBD Vol. 1, Part2: Spatial Data Processing. The errors are negligible for the upper atmosphere because the 200-km composites are virtually identical to the reporting cell.

Table 5-2: Error budget for the AVTP EDR (K).

Term	Clear		Clear or Cloudy					Cloudy	
	Surface to 700 mb	700 mb to 300 mb	300 mb to 30 mb	30 to 6 mb	6 mb to 1 mb	1 to 0.3 mb	0.3 mb to 0.01 mb	Surface to 700 mb	700 mb to 300 mb
Default core module retrieval error	1.30	1.11	1.19	1.3	2.2	3.3	6.5	1.76	1.14
Adjustment for cascade from 50 to 40-km HCS	0	0	0	0	0	0	0	0	0
Adjustment for air mass classification	-0.01	-0.02	-0.1	-0	-0	-0	-0	-0.01	-0.02
Residual calibration/model bias	0.1	0.1	0.1	0.1	0.1	0.1	0.1	0.1	0.1
Residual unsystematic spectroscopic error	0.1	0.1	0.1	0.1	0.1	0.1	0.1	0.1	0.1
Sub-FOV effects	0	0	0	0	0	0	0	0.02	0.02
Channel spatial	0.02	0.02	0	0	0	0	0	0.02	0.02

coregistration error									
Channel temporal offset	0	0	0	0	0	0	0	0	0
Surface pressure error	0	0	0	0	0	0	0	0	0
Subtotal	1.51	1.31	1.29	1.5				1.99	1.36
Vertical interpolation	0	0	0	0	0	0	0	0	0
Vertical registration (horizontal interpolation)	0	0	0	0	0	0	0	0	0
Cell mismatch	0.1	0.1	0.1	0	0	0	0	0.1	0.1
Polarization impurity	0	0	0	0	0	0	0	0	0
Net	1.51	1.31	1.29	1.5	2.4	3.5	6.5	1.99	1.36

Table 5-3: AVTP error for various environments. Shaded values are excluded from the net, as discussed in the text.

Region	% Coverage	Clear		Clear or Cloudy	Cloudy	
		Surface to 700 mb	700 mb to 300 mb	300 mb to 30 mb	Surface to 700 mb	700 mb to 300 mb
Ocean	71	1.30	1.05	1.16	1.65	1.08
Warm land	20	2.00	1.15	1.22	2.06	1.18
Cold land	9	2.00	1.50	1.40	2.00	1.52
Net		1.30	1.11	1.19	1.76	1.14

5.5. Performance under degraded measurement conditions

Performance under degraded measurement conditions is summarized in Table 5-4. Conditions where the EDRs cannot be retrieved to within any reliable level of performance are listed in Table 5-5. Performance near the ground is degraded by sensing over a surface with a high, variable emissivity, such as land and ice, while the SRD requirements under clear conditions do not accommodate this degradation. Performance is maintained within or near threshold for light precipitation, but degrades for heavier precipitation (Figure 5-28).

Table 5-4: AVTP EDR performance under degraded measurement conditions

Condition	Layer	Measurement uncertainty
Clear sky over land or ice surface	Surface to 700 mb	2.3 K / 1 km layers
Precipitation rate greater than 0.05 mm/h and less than 0.4 mm/h	Surface to 700 mb	2.5 K / 1 km layers
Precipitation rate greater than 0.05 mm/h and less	700 mb to 300 mb	2.0 K / 1 km layers

than 0.4 mm/h		
---------------	--	--

Table 5-5: Excluded measuring conditions for the AVTP EDR

Condition	Layer
Surface pressure uncertainty greater than 20 mb	Surface to 700 mb
Precipitation rate greater than 0.4 mm/h	Surface to 20 mb
Magnetic field storm, with any component of magnetic field disturbed by more than 300 nT	20 mb to 0.01 mb
Beyond swath width of 1540 km	20 mb to 0.01 mb

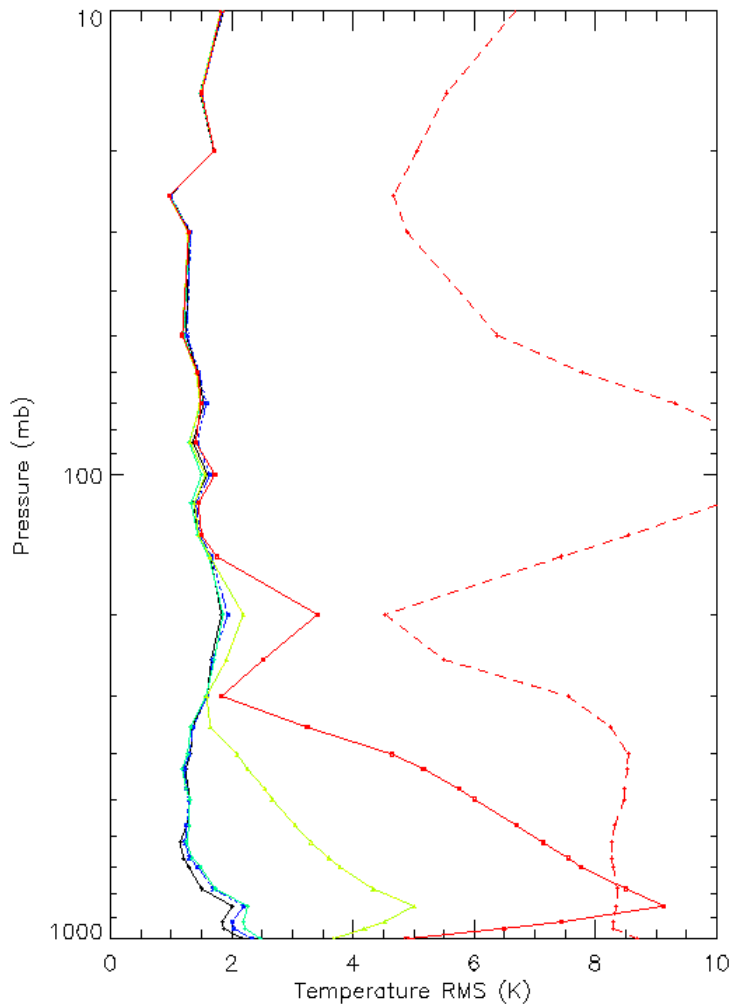


Figure 5-28: Temperature profile retrieval rms error for various precipitation rates. The curves are for the first-guess (dashed red), clear sky (black), and rain rates of 0.1 (blue), 0.4 (green-blue), 1.0 (yellow-green), and 1.7 (red) mm/h. The test cases for this plot had a rain layer top at 700 mb and excludes channels with frequencies above 61 GHz. The plotted performance is for 30-km CFOV size and was computed without vertical averaging, so it is not directly comparable to the SRD requirements.

5.6. Constraints, Limitations, and Assumptions

Performance estimates assume post-launch estimation and correction for systematic sensor errors, including calibration bias errors.

Center frequency errors tend to vary primarily with sensor aging and secondarily with sensor temperature. For temperature sounding, the errors are manifested primarily in a simultaneous drift in all the passbands in the 50-60-GHz channel set. The broad-passband channels in the set are robust with respect to center frequency errors because the channel optimization included a term that represented center frequency error as a noise source in the brightness temperatures. This term caused the passbands to avoid spectral locations where passband shifts up to 2 MHz caused large changes in brightness temperature.

Channels for upper atmosphere sounding are more susceptible to center frequency shifts because they must be positioned where spectral structure is very fine (near line centers). The use of a set of contiguous, fine-resolution channels (through digital processing) for CMIS facilitates post-launch correction of center frequency errors. Each set of measurements provides a brightness temperature spectrum that reflects the line shape. If the channel frequencies have shifted from the nominal values used in the algorithm radiative transfer computations, the retrieval performance will degrade and, in addition, the fit between the observations and the algorithm-computed brightness temperatures will degrade. This phenomenon is illustrated in Figure 5-29 and Figure 5-30. Note that significant performance degradation does not occur without significant impact on the retrieval residual brightness temperature difference. These residuals are a diagnostic parameter generated by the algorithm. Center frequency shifts can be detected and corrected post-launch by performing retrievals off-line with a variety of assumed shifts. Residual statistics can be compiled over a large number of retrievals to minimize the influence of data noise. The shift that produces the lowest residuals is inferred to be the actual on-orbit shift. That shift can then be applied to the on-line retrievals. If necessary, the correction can be made to vary with sensor temperature. We estimate that center frequency errors can be reduced by this procedure to 20 kHz or less.

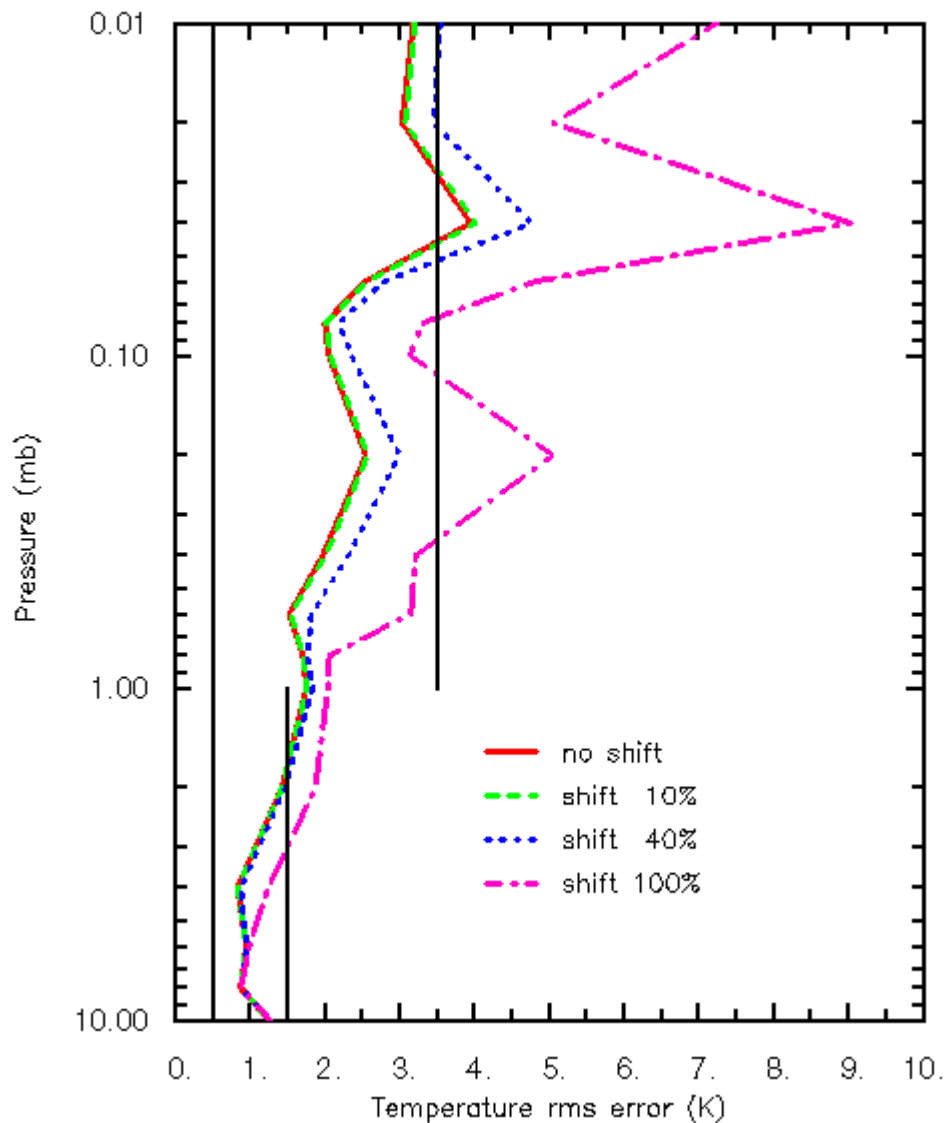


Figure 5-29. Upper atmosphere temperature profile rms error for varying center frequency knowledge error. The errors are given as a fraction of the bandwidth. The plot is for a channel set with digital (FFT) channels having 156-kHz resolution, so a shift of 10% is 15.6 kHz for the digital channels. The noise averaging factor was 0.17. Statistics are for a 20-profile subset of the Rosenkranz dataset. The sampling of geomagnetic field conditions was from method 1.

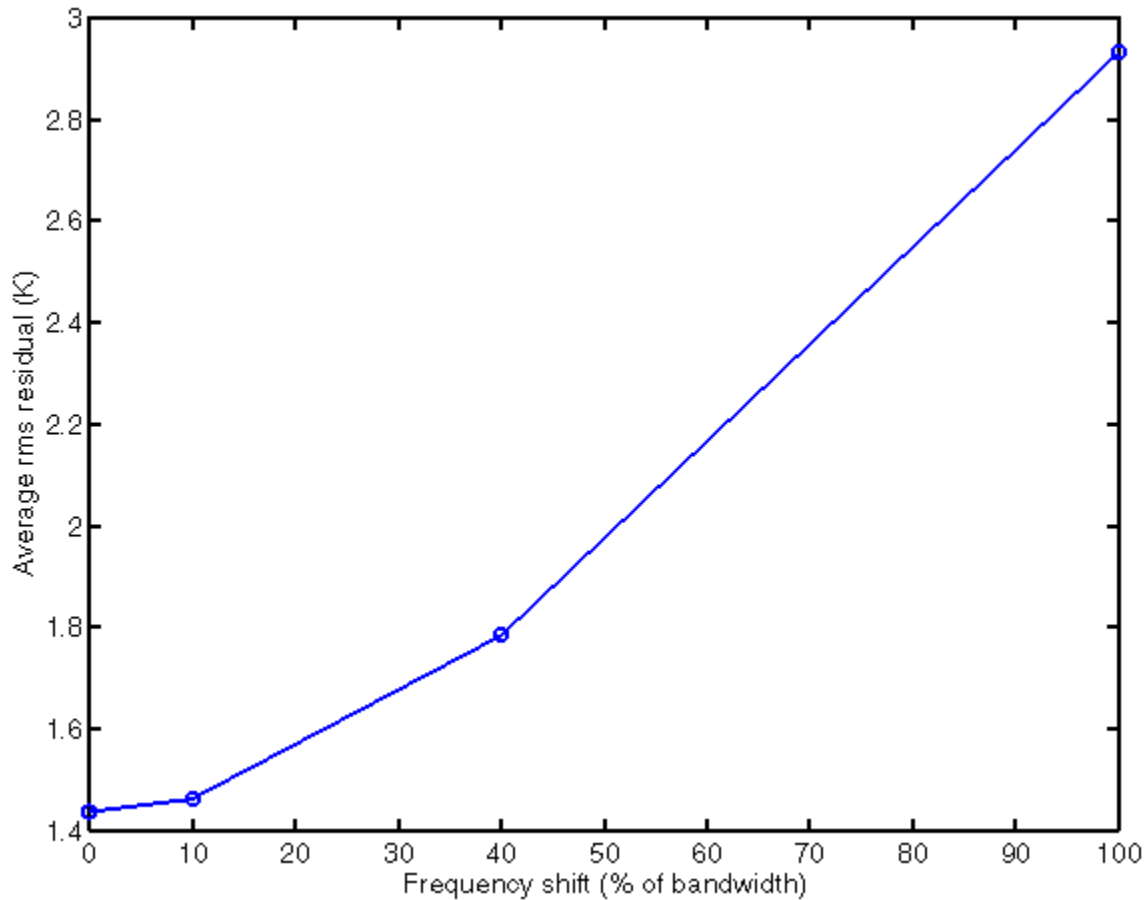


Figure 5-30. Brightness temperature residual difference from the upper atmosphere algorithm as a function of the center frequency shift from the nominal passband positions, corresponding to Figure 5-29.

6. Algorithm Calibration and Validation Requirements

6.1. Pre-launch

6.2. Post-launch

6.3. Special considerations for Cal/Val

6.3.1. Measurement hardware

6.3.2. Field measurements or sensors

6.3.3. Sources of truth data

7. Practical Considerations

7.1. Numerical Computation Considerations

7.2. Programming/Procedure Considerations

7.3. Computer hardware or software requirements

7.4. Quality Control and Diagnostics

7.5. Exception and Error Handling

7.6. Special database considerations

7.7. Special operator training requirements

7.8. Archival requirements

8. Glossary of Acronyms

ATBD	Algorithm Theoretical Basis Document
AVTP	Atmospheric Vertical Temperature Profile
CFOV	Composite Field Of View
CMIS	Conical Microwave Imaging Sounder
CRISTA	Cryogenic Infrared Spectrometers and Telescopes for the Atmosphere
EDR	Environmental Data Record
EFOV	Effective Field Of View
EIA	Earth Incidence Angle
FOV	Field Of View
IFOV	Instantaneous Field Of View
NCAR	National Center for Atmospheric Research
NCDC	National Climatic Data Center
NPOESS	National Polar-orbiting Operational Environmental satellite System
RMS	Root Mean Square
SDR	Sensor Data Record
SSMIS	Special Sensor Microwave Imager Sounder

9. References

9.1. Technical Literature

- Chahine, M. T., 1968: Determination of the temperature profile in an atmosphere from its outgoing radiance. *J. Opt. Soc. Amer.*, 58, 1634-1637.
- Chedin, A., N. A. Scott, C. Wahiche, and P. Moulinier, 1985: The Improved Initialization Inversion method: a high resolution physical method for temperature retrieval from the TIROS-N series. *J. Clim. Appl. Meteor.*, 24, 124-143.
- English, S. J., 1999: Estimation of temperature and humidity profile information from microwave radiances over different surface types. *J. Appl. Meteor.*, 38, 1526-1541.
- Fishbein, E. F., R. E. Cofield, L. Froidevaux, R. F. Jarnot, T. Lungu, W. G. Read, Z. Shippony, J. W. Waters, I. S. McDermid, T. J. McGee, U. Singh, M. Gross, A. Hauchecorne, P. Keckhut, M. E. Gelman, and R. M. Nagatani, 1996: Validation of UARS Microwave Limb Sounder temperature and pressure measurements. *J. Geophys. Res.*, 101, 9983-1001.
- Hayden, C. M., 1988: GOES-VAS simultaneous temperature-moisture retrieval algorithm. *J. Appl. Meteor.*, 27, 705-733.
- Hendin, A. E., 1991: Extension of the MSIS thermospheric model into the middle and lower atmosphere. *J. Geophys. Res.*, 96, 1159-1172.

- Kostsov, V., Y. Timofeyev, and K. Grossmann, 2001: Interpretation of the limb radiance measurements in the CO₂ 15 μ m band by the CRISTA instrument accounting for the non-LTE conditions. In *IRS2000, Current Problems in Atmospheric Radiation*, W. L. Smith and Y. M. Timofeyev, Eds. Proceedings of the International Radiation Symposium, 24-29 Aug. 2000, St. Petersburg. A. Deepak, Hampton VA.
- Lenoir, W. B., 1967: Propagation of partially polarized waves in a slightly anisotropic medium. *J. Appl. Phys.*, 38, 5283-5290.
- Lenoir, W. B., 1968: Microwave spectrum of molecular oxygen in the mesosphere. *J. Geophys. Res.*, 73, 361-376.
- McClatchey, R. A., R. W. Fenn, J. E. A. Selby, F. E. Volz, and J. S. Garing, 1971: Optical properties of the atmosphere. Environ. Res. Pap. No. 354, AFCRL-71-0279.
- McNally, A. P., J. C. Derber, W.-S. Wu, and B. B. Katz, 2000: The use of TOVS level-1B radiances in the NCEP SSI analysis system. *Quart. J. Roy. Meteor. Soc.*, 126, 689-724.
- Riese, M., R. Spang, P. Preusse, M. Ern, M. Jarisch, D. Offermann, and K. U. Grossmann, 1999: Cryogenic Infrared Spectrometers and Telescopes for the Atmosphere (CRISTA) data processing and atmospheric temperature and trace gas retrieval. *J. Geophys. Res.*, 104, 1634-1636.
- Rodgers, C. D., 1976: Retrieval of atmospheric temperature and composition from remote measurements of thermal radiation, *Rev. Geophys. and Space Phys.*, 14(4):609-624.
- Rodgers, C. D., 1990: Characterization and error analysis of profiles retrieved from remote sounding measurements. *J. Geophys. Res.*, 95, 5587-5595.
- Rosenkranz, P. W., 1995: A rapid atmospheric transmittance algorithm for microwave sounding channels. *IEEE Trans. Geosci. Remote Sensing*, 33, 1135-1140.
- Rosenkranz, P. W., and D. H. Staelin, 1988: Polarized thermal microwave emission from oxygen in the mesosphere. *Radio Sci.*, 23, 721-729.
- Rosenkranz, P. W., K. D. Hutchinson, K. R. Hardy, and M. S. Davis, 1997: An assessment of the impact of satellite microwave sounder incidence angle and scan geometry on the accuracy of atmospheric temperature profile retrievals. *J. Atmos. Ocean. Tech.*, 14, 488-494.
- Smith, W. L., 1970: Iterative solution of the radiative transfer equation for the temperature and absorbing gas profile of an atmosphere. *Appl. Opt.*, 9, 1993-1999.
- Smith, W. L., and H. M. Woolf, 1976: The use of eigenvectors of statistical covariance matrices for interpreting satellite sounding radiometer observations. *J. Atmos. Sci.*, 33, 1127-1140.
- Stogryn, A., 1989: Mesospheric temperature soundings with microwave radiometers. *IEEE Trans. Geosci. Remote Sensing*, 27, 332-338.
- Thompson, O. E., M. D. Goldberg, and D. A. Dazlich, 1985: Pattern recognition in the satellite temperature retrieval problem. *J. Climate Appl. Meteor.*, 24, 30-48.
- Uddstrom, M. J., and D. Q. Wark, 1985: A classification scheme for satellite temperature retrievals. *J. Climate Appl. Meteor.*, 24, 16-29.
- Ulaby, F. T., R. K. Moore, A. K. Fung, 1981: *Microwave Remote Sensing: Active and Passive: Volume I: Microwave Remote Sensing Fundamentals and Radiometry*, Addison-Wesley, Reading, Mass.
- Wark, D. A., and H. E. Fleming, 1966: Indirect measurements of atmospheric profiles from satellites. I Introduction. *Mon. Wea. Rev.*, 94, 351-362.
- Wentz, F. J., A well calibrated ocean algorithm for SSM/I, *JGR*, Vol 102, pp 8703-8718, 1997.

This page intentionally left blank.